AN INVESTIGATION INTO THE EFFECT OF ELECTROSTATIC ACTUATION AND MECHANICAL SHOCK ON MICROSTRUCTURES

BY

MAHMOUD IBRAHIM IBRAHIM

B.S, State University of New York at Binghamton, NY, 2007

THESIS

Submitted in partial fulfillment of the requirements for
the degree of Master of Science in Mechanical Engineering
in the Graduate School of
Binghamton University
State University of New York
2009

Accepted in partial fulfillment of the requirements for
the degree of Master of Science in Mechanical Engineering
in the Graduate School of
Binghamton University
State University of New York
2009

May 1, 2009

Professor Mohammad I. Younis ______________________________ Date _____________
Department of Mechanical Engineering
Binghamton University

Professor Ronald N. Miles __________________________________ Date _____________
Department of Mechanical Engineering
Binghamton University

Professor James Pitarresi ____________________________________ Date _____________
Chairman of the Department of Mechanical Engineering
Binghamton University

Abstract

Understanding the behavior and modes of failure of micro-electro-mechanical systems (MEMS) under different conditions is a crucial element to enhance their reliability and sensitivity, which may also lead to widen their use to more applications. One of the major causes of failure in these devices is mechanical shock. In this work we present a theoretical and experimental investigation into the effects of mechanical shock on microstructures under the influence of squeeze film damping and electrostatic forces. For the theoretical investigation, a single-degree-of-freedom system is used to model a microstructure. Simulation results are demonstrated in a series of shock spectra that help indicate the nonlinear effects due to electrostatic and squeeze film forces on the motion of the microstructure. In practical applications, the microstructure is mounted on a printed circuit board (PCB). For that purpose, the effect of the motion of a PCB on the microstructure response is also investigated, both theoretically and experimentally. For the theoretical part, a two-degree-of-freedom system is used to model the PCB and microstructure assembly.

The effect of mechanical shock on the response of resonant sensors is another reliability issue that is addressed in this work. Resonant sensors typically operate at low pressures for enhanced sensitivity, which makes their response to external disturbances such as shock a greater issue. For the theoretical investigation, a single-degree-of-freedom system is used to model the resonant sensor, which is electrostatically driven by a DC load superimposed to an AC harmonic load. Experimental work is also conducted for this case.

Finally, we present an investigation in using the nonlinearities arising from electrostatic actuation to enhance the sensitivity of a resonant accelerometer. Several results are shown for the effect of the DC and AC voltages on enhancing the sensitivity of the accelerometer. The use of the accelerometer as a switch triggered by low accelerations while operating at primary or sub-harmonic resonance is also investigated.

The experimental investigations in this work were conducted on a capacitive accelerometer. It is found that the experimental data are in good agreement with the simulation results in all the investigated cases. It is found that accounting for the nonlinearities, arising from the DC load and the AC harmonic load, and for the PCB motion is crucial. In some cases, whether the microstructure is operated as a capacitive sensor or a resonant sensor, the microstructure may experience an early dynamic instability. This in turn may lead to unexpected failure of the sensor.

Dedication

To my loving parents Ibrahim and Sondos.

Acknowledgments

I express my deep sense of gratitude to my thesis advisor Dr. Mohammed Younis for his guidance, invaluable suggestions, and encouragement during my study in the mechanical master program.

I am very grateful to my colleague Fadi Al Alsaleem for his time and technical advices throughout the coursework of this thesis.

Special thanks to Dr. James Pitarresi and Dr. Ronald Miles for their time and willingness to be on my committee, and for their excellent teaching during my study.

I would also like to thank all my graduate colleagues, especially Hassen Ouakad, and Tariq Tashtoush. Special thanks to Dr. Quang Su for his help in the experimental setup.

Table of Contents

List of Figures

List of Tables

Chapter 1. Introduction

1.1 Motivation

Microelectromechanical systems (MEMS) are miniature, low powered devices. Currently, they have become well commercialized products used in a variety of industries, such as aerospace, health care, automotives, and telecommunications (Hsu, 2002). The ability to manufacture MEMS devices using existing manufacturing techniques enables their production in large volumes under low costs. These attractive features of MEMS drew the industry into mass producing sensors and actuators, realized as MEMS devices, causing the exceptional establishment of the MEMS field. There is no limit to the wide range of applications MEMS products are used for, examples of which include, pressure sensors, airbag accelerometers, mirror arrays for television and displays, micromirrors, and disposable medical devices (Hsu, 2002).

Despite how well researchers and the industry utilized the attractive features of MEMS, there is still a lot of room for optimizing the performance of MEMS devices, and in turn enhancing their sensitivity and reliability. Understanding the behavior and modes of failure of MEMS under different conditions is crucial to allow us to enhance their sensitivity and reliability and also to widen their use to more applications. Mechanical shock is one of the major causes of failure in MEMS devices. The MEMS can be exposed to shock during fabrication, shipping, storage, or end use. They can fail in a number of ways including fracture (Tanner et al., 2000) and stiction (Hartzell and Woodilla, 1999). This thesis concentrates on the response of MEMS under mechanical shock accounting for most of the practical issues in MEMS, including the effect of the motion of printed circuit boards (PCBs).

Not only are the external factors such as mechanical shock or the motion of a PCB affect the response of MEMS devices, but also nonlinear effects within the microstructure itself affect the response, and therefore the reliability, of MEMS devices. Nonlinearities are present in MEMS in many different forms. The most common are electrostatic forces, squeeze film damping, thermo-elastic damping, and mid-plane stretching. The interest of this thesis is to consider the nonlinear effects of electrostatic forces and squeeze film damping, along with the presence of external effects from mechanical shock and PCB motion, on the response of MEMS devices.

Accelerometers are one of the well established MEMS products and one which has been under major concentration in industry. Recently, ultra sensitive accelerometers sensing accelerations in the micro range (micro-g accelerometers) have been under increasing focus in the research community. This focus is due to the many applications in which they are needed. Some of these applications include GPS navigation and guidance systems, seismometry for earthquake prediction and oil-exploration, micro-gravity measurements in space, underwater acoustic measurements, unmanned aerial vehicles (UAV’s), and virtual reality headsets (Yazdi and Najafi, 2000). Capacitive sensing, resonant sensing, and tunneling current sensing, are all sensing schemes that have been employed to develop micro-g accelerometers. This thesis explores using the nonlinear effects of electrostatic forces in enhancing the sensitivity of a resonant type accelerometer.

1.2 Literature Review

The evolvement of the MEMS field over the past years has led to many investigations over the various aspects of MEMS. In this section, we review the relevant contributions found in the literature on three primary topics discussed in this thesis (reliability of MEMS under shock, nonlinearities in MEMS, and micro-g accelerometers).

1.2.1 Reliability of MEMS under shock

Numerous works have been conducted to address the behavior of microstructures under mechanical shock. Next, we summarize the main contributions.

Wagner et al. (2001) considered shock loads on MEMS-structures that arise during drop-tests. They used a z-axis sensor and theoretically tested, using finite element (FE) analyses, the stress history during impact of two different designs. For the purpose of their experimental investigation, z-axis sensors were fabricated and tested under both controlled drops and fully guided impacts. They observed two types of failures, which raised the question of re-evaluating the FE results to monitor those failures. De Coster et al. (2004) raised the importance of taking the effect of mechanical shock into the design of RF-MEMS capacitive switches. They presented a method in analyzing the response of electrostatically driven RF-MEMS capacitive switches to external mechanical shock. They showed that the power handling of shunt switch can fall by more than 30% under shocks of 5000 ms^{-2}. Srikar and Senturia (2002) investigated the effect of shock and shock duration on MEMS devices and defined three relevant time scales: acoustic transit time, the time period of vibrations, and the duration of the applied shock. They found that many MEMS devices respond quasi-statically in a shock environment. Younis et al. (2007) developed a Glarekin-based reduced-order model to simulate the response of microstructures under mechanical shock. Both cantilever and clamped-clamped microbeams were simulated to account for low-frequency and high-frequency microstructures. Their model was capable of capturing the dynamic behavior of microstructures under both high and low shock loads, for both linear and nonlinear behaviors.

In the previous summary, the response of microstructures alone was considered. However, microstructures in real-life applications are packaged and attached to printed circuit boards (PCBs), which in turn could have a significant influence on the microstructures' response. Next, we focus merely on the effect mechanical shock on a PCB. Lim et al. (2002) presented a FE model to study the drop impact response on an electronic pager. They concentrated on the effects of the point of application of shock. Pitarresi and Primavera (1992) concentrated on the different modeling techniques in determining the dynamic characteristics of circuit cards populated with components (microstructures). They compared the simulation results with experimental modal analysis and found that accounting for the mass and stiffness of the components on the circuit cards yielded the best results. Wong et al. (2005) presented a comprehensive study on the effects of PCB materials and dimensions on the interconnection stresses. They modeled the PCB as a spring-mass system, a beam, and a plate, and studied its dynamics under a half-sine shock pulse.

Other authors such as Luan et al. (2003), Ong et al. (2003), and Suhir et al. (2000) have studied the effect of mechanical shock on a PCB and concentrated on the failure of solders. One common factor missing in these contributions is the effect of the motion of the PCB on the microstructure itself. Wong et al. (2005) mentioned, focusing only on the effects of drop impact on interconnections, that taking measures such as lowering the PCB stiffness, and therefore the natural frequency, would not be effective against drop impact. Alsaleem et al. (2009) investigated the effect of the motion of a PCB on the response of a MEMS device to shock loads. They showed the significance of accounting for the PCB effect when modeling a MEMS device under shock, as it could lead to inaccurate predictions of the microstructure motion. They found that a poor design of the PCB or the MEMS package may result in severe amplification of the shock effect. This contradicts with Srikar and Senturia (2002) who mentioned that, in a worst case scenario, the PCB transmits the shock load to the microstructure without changing its intensity, however; in most cases the PCB reduces the applied shock on the microstructure. It will be shown later that the natural frequency of the PCB can extensively affect the motion of the microstructure and sometimes lead to its failure, as presented by Alsaleem et al. (2009).

1.2.2 Nonlinearities in MEMS

Sources of nonlinearities in MEMS can exist from electrostatic forces, squeeze film damping, material nonlinearities, and geometric nonlinearities. The focus of this thesis is to discuss the effects of squeeze film damping and electrostatic forces on the response of microstructures.

1.2.2.1 Squeeze film damping

The phenomenon of squeeze film damping exists in any MEMS device that employs the principle of a parallel-plate capacitor, where a movable electrode moves towards a stationary electrode. In typical MEMS devices, the distance (gap) between the electrodes is in the micro range. In the presence of a structure with a large surface area compared to the gap width, as the structure moves towards the stationary electrode, the air between the electrodes acts as a highly viscous fluid, opposing the motion of the proof mass. This is referred to as squeeze film damping (SQFD). There has been extensive research in the past addressing the effects of squeeze film damping on microstructures. Next we summarize some of these contributions.

We begin with Starr (1990) who modeled the squeeze film damping in a parallel-plate capacitive accelerometer using a linearized Reynolds equation. He derived an exact expression for the damping forces of a circular disk and an approximate expression for the damping force of a rectangular plate. Chu et al. (1996) investigated the dynamics of polysilicon parallel-plate electrostatic actuators. To account for squeeze film damping they used the same expressions used by Starr (1990), however, they modified the expressions to account for the varying gap distance as the proof mass moves. Zhang et al. (2004) studied the effect of squeeze film damping on a microbeam resonator. They presented a first-order analysis for the squeeze film damping effect, which is based on the coupled elastic beam theory and Reynolds equation of incompressible fluid films. The perturbation method was used to linearize the Reynolds equation as in Starr (1990). The solution of the coupled solid deformation and fluid flow equations showed that the squeeze film effect can be characterized by two dimensionless parameters used for the simple spring-mass-damper system. Jordy and Younis (2008) explored the use of squeeze film damping phenomenon as a way to mitigate shock and its effects on microstructures. They investigated the effect of changing the size of the perforation holes and the gap width. As a case study, they used a G-sensor and found that the threshold shock increases significantly when the holes size or gap width are decreased. Darling et al. (1998) used a green function method to find the solution of the linearized Reynolds equation. A number of useful cases on the effects of damping on cantilevers, diaphragms, tilting plates, and drum-head modes are presented. Pan et al. (1998) concentrated on the squeeze film damping effect on a MEMS torsion mirror (rotation between two very closely spaced surfaces). Both the Fourier series solution and the double sine series solution were derived for the linearized Reynold equation. An experimental investigation was carried out and the results were close to the modeling results.

Blech (1983) solved analytically the linearized Reynolds equation in the case of oscillating rigid plates of rectangular and circular shapes with trivial pressure boundary conditions and derived analytical expressions for the spring and damping forces. Blech (1983) referred to the use of squeezed gas films in tailoring the frequency response of seismic accelerometers. Andrews et al. (1992) employed the Blech model (Blech, 1983) in investigating the squeeze film effects on microstructures. They compared theoretical and experimental measurements over a range of pressures and frequencies where the results were in good agreement except for some discrepancies at low and high frequencies. Veijola et al. (1995) derived an electrical equivalent circuit for the damping and spring forces based on the Blech model (Blech, 1983). They conducted simulations and experimental measurements on a capacitive accelerometer to verify their model and the results were found to be in good agreement. Nayfeh and Younis (2004) presented a new approach in modeling flexible microstructures under the effect of squeeze film damping. They used perturbation methods in deriving an analytical expression for the pressure distribution. Their theoretical calculations of the quality factors are in good agreement with available experimental data. Younis and Nayfeh (2007) also presented simulations of squeeze film damping in microplates actuated by large electrostatic loads. They derived analytical expressions for the pressure distribution in terms of the plate mode shape around the deflected position using perturbation techniques.

1.2.2.2 Electrostatic forces

The second nonlinearity investigated in this thesis is from the electrostatic forces in microstructures. Several means of actuation are used for MEMS such as electrostatic, thermal, electromagnetic, piezoelectric, piezomagnetic, and optical actuation (Rebeiz, 2003). Electrostatic actuation is the most common method of actuation in MEMS devices due to its simplicity and low-power consumption. A typical electrostatically actuated microstructure employs two parallel-plates, a microbeam and stationary electrode separated by a gap, where the microbeam is actuated by a DC bias. In the case of a resonator, the microbeam is driven by an AC harmonic load in addition to the DC load. The DC bias causes an initial deflection of the beam to a new equilibrium position and the AC harmonic load causes the beam to vibrate about the new equilibrium. However, there is a limit to the voltage used in actuating a microstructure depending on its geometric and mechanical properties, beyond which the microstructure experiences an instability known as “pull-in” (Younis et al., 2003), where the microstructure touches the stationary electrode. The voltage associated with pull-in is known as the “pull-in voltage”.

A great number of publications reported observations of nonlinear response of microstructures due to electrostatic forces. Legtenberg and Tilmans (1994) conducted both theoretical and experimental investigations on electrostatically driven vacuum-encapsulated polysilicon resonators and noted a hardening behavior. Ayela and Fourneir (1998) investigated the nonlinear behavior of electrostatically excited micromachined silicon resonators and observed a softening behavior which they claimed was due to the mechanical properties of the resonators rather than the electrostatic excitation. Gui et al. (1998) studied the nonlinearity and hysteresis effects of electrostatically actuated resonant microbridges both theoretically and experimentally. They observed that in order to avoid hysteresis, the choices of DC and AC driving voltages, quality factor, and geometry of the microbridge are crucial. Their investigation concluded that reducing the quality factor and driving voltages or increasing the pull-in voltage increase the chances of a hysteresis-free operation, however, under the cost of losing resolution and frequency stability, lower sensitivity, and a higher noise level. Veijola et al. (2000) investigated nonlinearities in electrostatically driven MEMS resonators using the harmonic balance method showing hardening effects due to the cubic nonlinearity of the spring coefficient and softening effects due to the electrostatic forces.

Starting 2002, the group of Abdel-Rahman, Nayfeh, and Younis presented one of the earliest robust theoretical works that discussed the nonlinearities of electrostatically-actuated microbeams. Abdel-Rahman et al. (2002) shed light on the importance of accounting for the mechanical restoring force of the microbeam (mid-plane stretching) to avoid underestimation to the stability limits. Softening behavior due to electrostatic forces was noted and the shift in the natural frequency of the microbeam due to the electrostatic forces was highlighted. They also showed how the microbeam dimensions can be used to extend the domain of the linear relationship between the electrostatic forces and the natural frequency. Younis and Nayfeh (2003) presented an investigation into the response of a resonant microbeam to an electric actuation. They accounted in their model for the nonlinear effects of mid-plane stretching, DC electrostatic force, and AC harmonic force. They validated their simulation results by comparing them with published experimental results. Abdel-Rahman and Nayfeh (2003) focused on the response of microbeam-based resonant sensors due to superharmonic and subharmonic electric actuations. They adopted the method of multiple scales to describe the response and stability of the microbeam. Typical frequency-response and forced-response curves were used to demonstrate different nonlinear aspects such as bifurcations and hysteresis which are meant to aid designers in safely operating their sensors at different frequencies. Nayfeh and Younis (2005) conducted similar work but concentrated on the effects of the large AC excitation amplitude on the frequency-response curves and reported a number of cases where dynamic instability (pull-in) occurs. Nayfeh et al. (2007) showed how the dynamic pull-in phenomenon could be utilized to design a low-voltage MEMS RF switch actuated with a combined DC and AC loading.

The works of Agrawal et al. (2006, 2007) investigated nonlinear effects on a double-ended-tuning-fork microresonator. Nonlinear hardening effects from the mechanical restoring force of the beam (mid-plane stretching) were observed at low bias voltages, and softening effects from the electrostatic forces were observed at high bias voltages. An intermediate bias voltage was presented, in which both nonlinearities cancel each other, increasing the linear range of the resonator. Also in the work of Agrawal et al.

(2007), they studied the scaling of nonlinearities in a double-ended-tuning-fork microresonator and found that increasing the resonant frequency as well as reducing the length of the microbeam strongly improves power handling of the microresonator. Similar studies were presented by Shao et al. (2007, 2008), in which the nonlinearities of micromechanical free-free beam resonators were investigated. Hardening and softening effects were again observed and the possibility of nonlinearity cancellation was discussed. In the work of Shao et al. (2008) specifically, a thorough investigation on the nonlinearity cancellation was conducted and was found to enhance the power handling capabilities of resonators, however, may not be achievable for resonators with a very large cubic mechanical spring constant. Alsaleem et al. (2009) provided a theoretical and experimental investigation on the nonlinear response of a capacitive sensor due to electrostatic forces. In analyzing the stability of the resonator response, a Floquet theory and the basin of attraction methods were used. Dover-cliff integrity curves were used to illustrate the erosion of the basin of attraction for given values of frequencies. This is a helpful tool for MEMS designers when questioning the safety of their resonator against disturbances.

In addition to the nonlinearities and hysteresis behaviors emphasized, more complex dynamical behaviors, such as chaos, were also observed and studied for electrostatically driven microstructures. Liu et al. (2004) conducted simulations on a MEMS cantilever system with electrostatic sensing and actuation, intended for a MEMS based mass storage chip. They observed bistability and a Hopf bifurcation in the closed loop controlled cantilever system without disturbances. De and Aluru et al. (2005, 2006) discussed complex nonlinear oscillations in electrostatically actuated microstructures.

They observed, through simulations, that the application of a large DC bias voltage on a microstructure under superharmonic excitation can bring it to a nonlinear state with chaotic behaviors. Park et al. (2008) investigated the potential of chaos control in microstructures and demonstrated that by adopting an appropriate feedback rule, a chaotic response can be effectively converted into a periodic response. This was shown to increase both the operating range and effective power output of the electrostatically-actuated microresonator under study.

1.2.2.3 Nonlinear shock spectra

Over a number of decades, researchers have tried to represent the nonlinear effects on the response of structures by the means of a nonlinear shock spectrum. Next we summarize some of the contributions focusing on nonlinear shock spectra.

Thomson et al. (1960) investigated the response of a single mass system with bilinear stiffness under different shock pulses and presented his results in a series of nondimensionalized nonlinear shock spectra. Young et al. (1963) pointed out the difficulty in presenting the nonlinear shock response problem since the superposition principle does not hold as in the linear case. Young et al. (1963) analyzed the response of an undamped single-degree-of-freedom system composed of a mass on a nonlinear spring. They investigated both the effect of a cubic-softening spring and a cubic-hardening spring and presented their results in a series of nondimensionalized shock spectra. It will be shown later that the softening effects that Young et al. (1963) analyzed resemble the effect of the electrostatic forces.

1.2.3 Highly sensitive accelerometers

The importance of highly sensitive accelerometers has been realized in the literature. A number of sensitive accelerometers have been fabricated and proposed employing capacitive sensing, resonant sensing, and tunneling current sensing. Capacitive sensing is attractive due to its high sensitivity, good noise performance and low-power dissipation. However, it does not easily implement digital readout. Tunneling sensors have a low noise floor. However, due to the small allowable displacement at the tip they require a very stiff feedback loop, which reduces the useful bandwidth and dynamic range. As for resonant sensing, it has high sensitivity, low electrical drift or noise, wide output range, and can easily implement digital readout. Here, we summarize some of the contributions related to highly sensitive accelerometers.

Yazdi and Najafi (2000) used a combined surface and micromachining process to fabricate a highly sensitive accelerometer that utilizes a capacitive sensing scheme. The sensitivity of the device was enhanced through the use of a large proof mass, small damping and a narrow uniform air gap over a large area. The device is tested by applying an electrostatic force to generate an input acceleration. The device shows a sensitivity of *2 pF/g*. Rudolf et al. (1990) fabricated an accelerometer utilizing capacitive sensing, working in the range of *1 μg* to *0.1 g* at frequencies from *0.01* to *100 Hz*. A number of static and dynamic measurements were taken and also temperature sensitivity was investigated. Another capacitive sensing accelerometer was introduced by Leuthold and Rudolf (1990) that uses a self-balancing capacitor bridge circuit, sensing capacitance with a resolution of *0.04 fF* for frequencies between *0* and *1 Hz*. Helsel and Gassner (1994) developed a monolithic bulk-micromachined vibrating beam accelerometer that uses capacitive sensing. An applied acceleration increases the resonant frequency of the vibrating beam, and capacitance is used to keep the beam oscillating at the resonant frequency. The accelerometer is developed for navigation purposes. Henrion et al. (1990) used silicon micromachining techniques to fabricate a high-precision high sensitivity accelerometer, which utilizes electrostatic field sensing and electrostatic force feedback. They claimed that the accelerometer can be built to sense accelerations from *nano-g* to hundreds of *g*. Roszhart et al. (1995) fabricated a micromachined vibrating beam accelerometer that uses resonant sensing. The device has a measured sensitivity of $1\ \mu g$ with a full scale of $40\ g$ and is designed for defense-related inertial navigation. Liu et al. (1998) fabricated a high sensitivity bulk-silicon-micromachined tunneling accelerometer that is intended for underwater acoustic applications. The measured sensitivity is *50 Volt/g* with a resolution of $2\mu g/\sqrt{Hz}$. Testing was conducted to verify the performance of the accelerometer.

A resonance type accelerometer detects variation of resonant frequency due to external acceleration. Numerous researches have been conducted in the area of resonant accelerometers and a number of them have been developed and fabricated, with some being commercially used. Burns and Horning (1995) fabricated a micromachined all-silicon acceleration sensor with a direct-to-digital frequency output. When the device is subjected to acceleration, bending stresses are created. The strain is measured and applied to the microbeam, shifting its resonant frequency. The accelerometer is developed for navigation purposes. Burrer and Esteve (1994) characterized and fabricated a resonant accelerometer, electrothermally driven and piezoresistively sensed. The device has a sensitivity of $200\ Hz\ g^{-1}$. Aikele and Bauer (2001) presented a resonant accelerometer, thermally excited and piezoresistively sensed. The accelerometer has a sensitivity of $70\ Hz\ g^{-1}$.

1.3 Thesis Objectives and Organization

The objectives of this thesis are:

- To study the combined effects of mechanical shock, electrostatic forces, and squeeze film damping on the response of a microstructure.
- To study the effect of PCB motion on the response of a microstructure.
- To investigate the use of nonlinearities in enhancing the sensitivity of a resonant accelerometer, and realizing its use as a switch triggered by low acceleration.
- To study the effect of mechanical shock on resonant sensors operating at reduced pressure conditions.
- To validate the theoretical investigations using experimental work on a commercially available MEMS device.

The organization of the thesis is as follows. In Chapter 2, we present a general theoretical background on mechanical shock in MEMS and the shock spectrum, electrostatic actuation, and squeeze film damping. In Chapter 3, we present both simulation and experimental investigations on the nonlinear effects of electrostatic forces and squeeze film damping on the motion of a MEMS device under mechanical shock. All the work is presented in a series of shock spectra. In Chapter 4 we investigate the effect of PCB motion on the response of microstructures under mechanical shock. The effect of the PCB and microstructure natural frequencies is highlighted.

In Chapter 5, we investigate the sensitivity enhancement of a resonant accelerometer by operating it in the nonlinear regime. The operation of the accelerometer at both primary and sub-harmonic resonance is investigated. This chapter also focuses on the use of the nonlinearities arising from the electrostatic forces to realize a switch triggered by low acceleration. In Chapter 6, we conduct a theoretical and experimental investigation on the effects of mechanical shock on the response of an electrostatically actuated resonant sensor with a focus on the effect of the AC harmonic load. The simulation results are demonstrated in a series of shock spectra that help indicate the combined effects of shock and the existing nonlinearities from the electrostatic forces. Finally, Chapter 7 concludes this thesis with summary, conclusions, and suggestions for future work.

Chapter 2. Background

2.1 Mechanical Shock in MEMS

Mechanical shock is the sudden force that can cause a sudden acceleration or deceleration for a system. It is caused by, for example, drop, impact, kick, earthquakes, or even an explosion. It is also defined as a transient physical excitation with a duration between once and twice the natural period of the excited mechanical system (Lalanne, 2002). In the case of microelectromechanical systems, shock could be experienced during fabrication, shipping, storage, or end use. Mechanical shock has the potential to cause undesirable effects on MEMS devices such as stiction and short circuit problems or even failure of the device through fracture.

2.1.1 Shock pulse shapes

Mechanical shock can be modeled theoretically to imitate the shock pulse a microstructure may experience. Different shapes of shock pulses have been adopted for that purpose, the most common of which are half-sine, triangular, and rectangular shock pulse shapes, which are represented in Figure 2.1 (Lalanne, 2002).

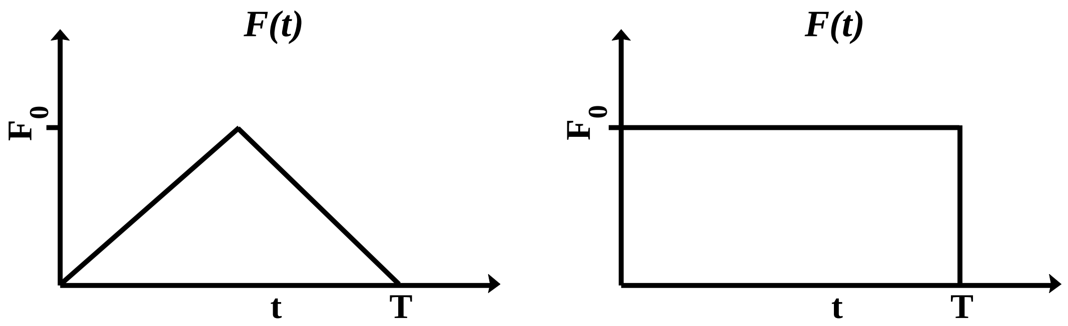

(a) Triangular pulse **(b) Rectangular pulse**

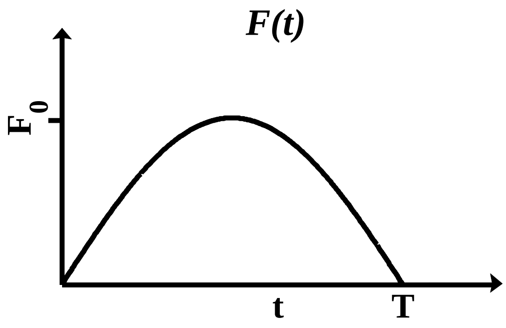

(c) Half-sine pulse

Figure 2.1: Shock pulse shapes.

2.1.2 Response of a linear single-degree-of-freedom system

In many cases, a single-degree-of-freedom model could be used as a simple representation of a microstructure. In order to obtain a solution to the response of a microstructure to shock, it is modeled as a spring-mass-damper system (Figure 2.2). The applied shock is modeled as a base excitation with the differential equation of motion of the microstructure written as:

$$m\ddot{z} + c\dot{z} + kz = -m\ddot{y} \tag{2.1}$$

where z is the relative deflection of the mass m, which is the absolute motion of the mass x minus that of the base y $(z = x - y)$, the superscript dot denotes time derivative, c is the viscous damper coefficient, k is the stiffness of the microstructure, and $\ddot{y}$ is the base acceleration pulse. The equation can be put in the form:

$$\ddot{z} + 2\xi\omega_n\dot{z} + \omega_n^2 z = -\ddot{y} \tag{2.2}$$

where,

$$\xi = \frac{c}{2\sqrt{km}} \text{ (damping ratio)} \tag{2.3}$$

and

$$\omega_n = \sqrt{\frac{k}{m}} \text{ (natural frequency)} \tag{2.4}$$

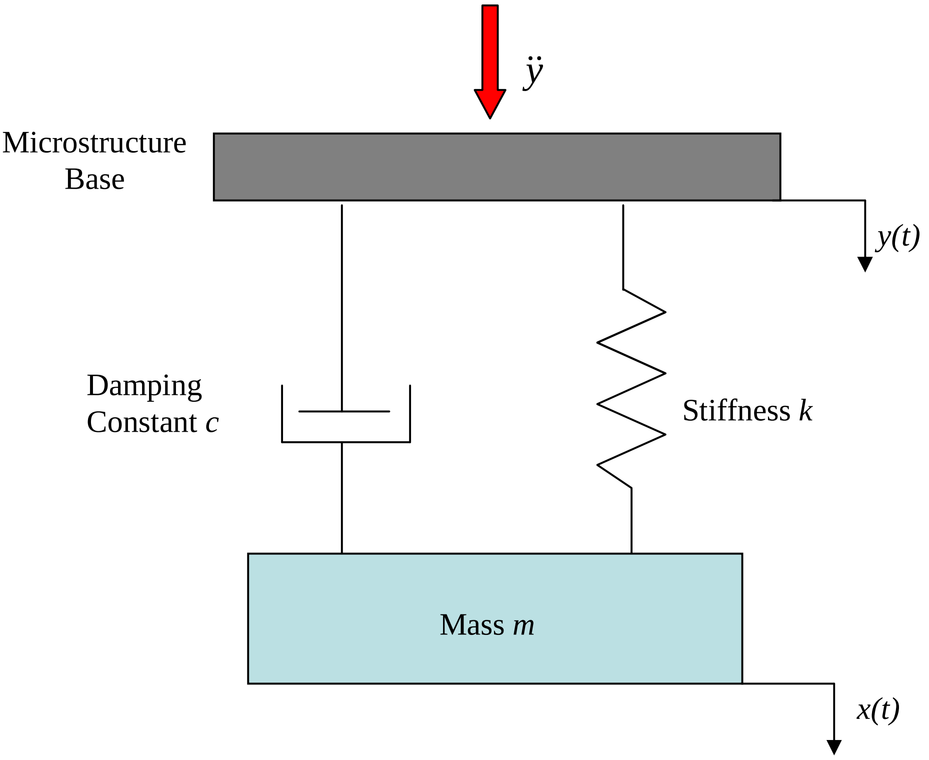

Figure 2.2: Linear single-degree-of-freedom system subjected to a base excitation.

The next step, given the microstructure parameters and shock pulse amplitude and shape, a numerical solution of the microstructure response can be obtained using direct time integration of the differential equation of motion, Equation (2.1).

The shock pulses applied to a microstructure in practical applications have different pulse shapes and can vary from one to another. Brown et al. (2001) showed that a good approximation to these shocks can be presented by a half-sine shock pulse (Figure 2.1a). For that reason, a half-sine pulse will be used throughout the simulations of this thesis to represent the applied base acceleration $\ddot{y}$, which is defined as:

$$\ddot{y} = A_0\left[\sin(\frac{\pi}{T}t)u(t) + \sin[\frac{\pi}{T}(t-T)]u(t-T)\right] \tag{2.5}$$

where A_0 is the amplitude, $u(t)$ is the unit step function, and T is the pulse duration. An example of a typical response of a microstructure to a shock load is depicted in Figure 2.3b.

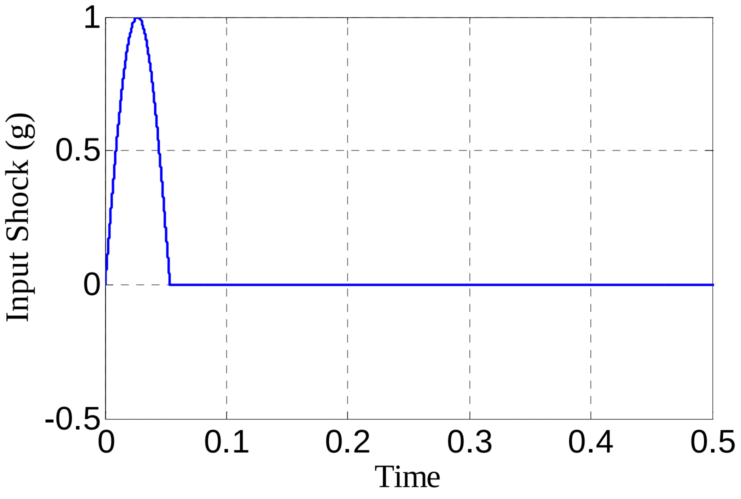

(a)

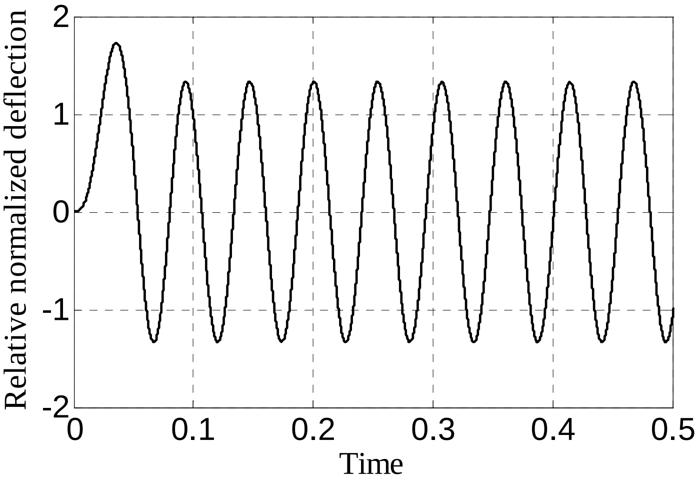

(b)

Figure 2.3: (a) Input shock of *1 g*. (b) Time history response of a microstructure to a shock load of *1 g* under zero damping.

2.1.3 Shock response spectrum

A Shock Response Spectrum (SRS) is a graphical representation showing the variation of the largest response of a linear Single-Degree-Of-Freedom (SDOF) system subjected to a mechanical shock, plotted against its natural period.

The linear shock response spectrum in Figure 2.4 represents the behavior of a structure when subjected to mechanical shock of a half-sine pulse shape. It shows the peak dynamic response of the structure A_{dyn} as a function of the shock duration T. Typically, A_{dyn} is normalized by the static response of the structure to an equivalent static load of the same shock amplitude and T is normalized by the natural period of the structure T_n.

As seen in Figure 2.4, the normalized peak dynamic response does not exceed *1.76* times the structure's static deflection and is achieved in the case of zero damping (Steinberg, 2000). The spectrum can be classified into three separate regions, the dynamic region, the quasi-static region, and the shock isolation region. In the dynamic region, the response of the structure is amplified as the shock duration is close to its natural period $\left(\frac{T}{T_n} \approx 1\right)$. In the quasi-static region, the shock duration is much larger than the natural period of the structure, where the shock is experienced almost as a static load. Hence, the response of the structure is almost equal to the static response.

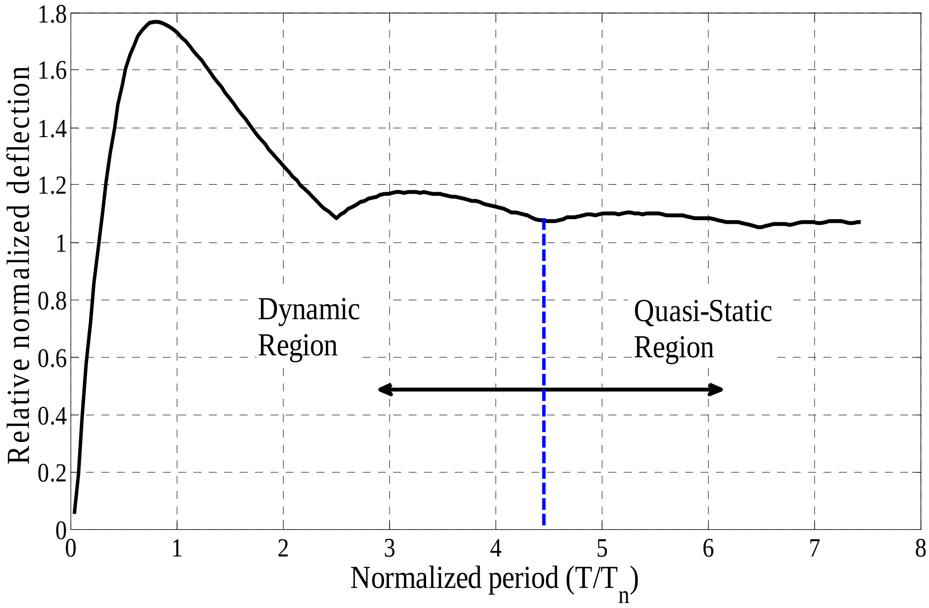

Figure 2.4: A shock response spectrum for a SDOF system of a half-sine shock pulse, assuming no damping.

2.2 Electrostatic Actuation

An actuator is defined as a mechanical device used to move or control something (Hsu, 2002). The three principle means in actuating microdevices are thermal forces, piezoelectric forces, and electrostatic forces. Electrostatic actuation is the most common method of actuation in MEMS devices due to its simplicity and low-power consumption.

As one of the focuses of this thsis is on the electrostatic forces, it is further introduced below.

2.2.1 Coulomb’s Law

Electrostatic force *F* is defined as the electrical force of repulsion or attraction induced by an electric field *E*. An electric field *E* exists in a field carrying positive and negative electric charges. Figure 2.5 shows two charged particles *A* and *B* existing in an electric field. The induced electrostatic force according to Coulomb’s law can be expressed as:

$$F = \frac{1}{4\pi\varepsilon}\frac{qq'}{r^2} \tag{2.6}$$

where ε = permittivity of the material separating the two particles and *r* is the distance between the two particles. In free space, $\varepsilon_0 = 8.85\,x10^{-12}\,C^2/N - m^2$. The force *F* is repulsive if both charges q and q’ carry the same charge sign, or attractive if both charges carry opposite signs.

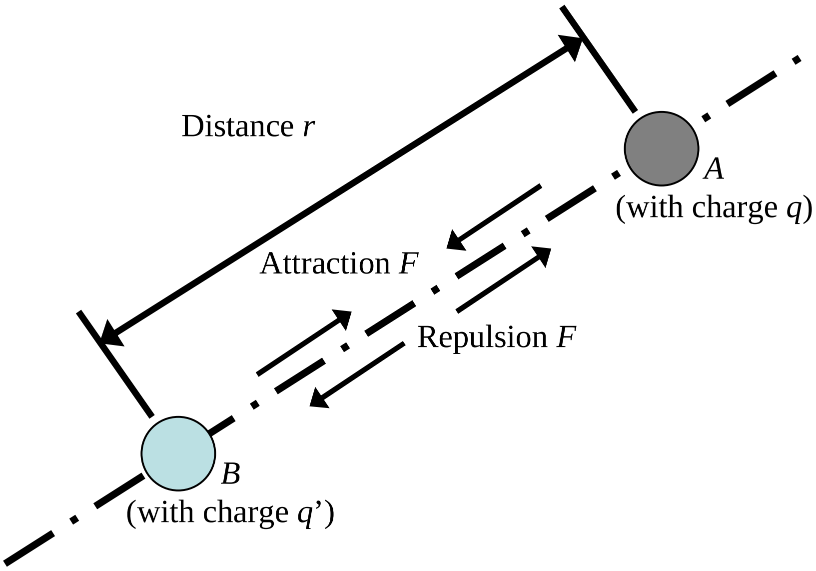

Figure 2.5: Two particles in an electric field.

2.2.2 Electrostatic forces in parallel plates

Figure 2.6 represents two charged plates separated by a dielectric material with gap *d*. The plates become electrically charged when a voltage is applied to the plates. This action induces capacitance in the charged plates, which can be expressed as:

$$C = \varepsilon_r \varepsilon_0 \frac{A}{d} = \varepsilon_r \varepsilon_0 \frac{WL}{d} \tag{2.7}$$

where, A is the area of the plates and ε_r is the relative permittivity. The energy associated with the electric potential can be expressed as:

$$U = \frac{1}{2} CV^2 = -\frac{\varepsilon_r \varepsilon_0 WLV^2}{2d} \tag{2.8}$$

The negative sign in Equation (2.8) exists because there is a loss of the potential energy with the increase of the applied voltage. The associated electrostatic force that is normal to the plates can be derived from the potential energy expression in Equation (2.8) as:

$$F_d = -\frac{\partial U}{\partial d} = -\frac{\varepsilon_r \varepsilon_0 WLV^2}{2d^2} \tag{2.9}$$

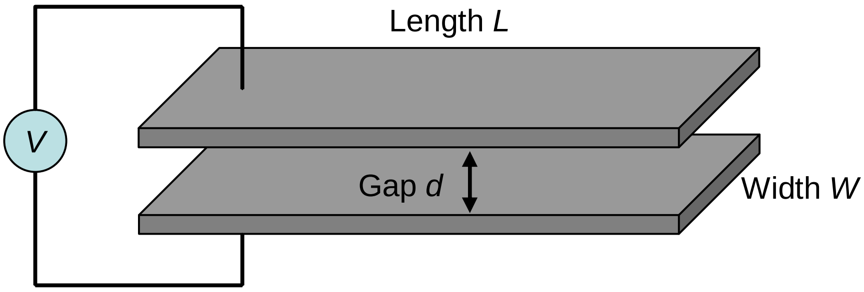

Figure 2.6: Electric potential in two parallel plates.

2.2.3 Electrostatically actuated microstructures

For an electrostatically actuated microstructure, we can once again adopt the single-degree-of-freedom model as in Figure 2.2, actuated by a DC voltage and with a separation gap *d* between the movable and stationary electrodes (Figure 2.7). The differential equation of motion now becomes:

$$m\ddot{x} + c\dot{x} + kx = \frac{\varepsilon A V_{DC}^2}{2(d - x(t))^2} \qquad (2.10)$$

In order to obtain the solutions of the above equation and check their stability, we use state space representation:

$$x_1 = x \ ; \ x_2 = \dot{x} \qquad (2.11a)$$

$$\dot{x}_1 = x_2 \ ; \ \dot{x}_2 = \frac{\varepsilon A V_{DC}^2}{2m(d - x_1)^2} - \frac{c}{m}x_2 - \frac{k}{m}x_1 \ ; \qquad (2.11b)$$

Next, we obtain the equilibrium points. Setting the right-hand side of Equation (2.11b) equal to zero yields,

$$\frac{\varepsilon A V_{DC}^2}{2m(d - x_1)^2} - \frac{k}{m}x_1 = 0 \qquad (2.12a)$$

$$2k(d^2 - 2x_1 d + x_1^2)x_1 = \varepsilon A V_{DC}^2 \qquad (2.12b)$$

$$x_1^3 - 2x_1^2 d + x_1 d^2 - \frac{\varepsilon A V_{DC}^2}{2k} = 0 \qquad (2.12c)$$

We solve Equation (2.12c) to get:

$$\frac{x_{11}}{d} < 1 \ ; \ \frac{x_{12}}{d} < 1 \ ; \ \frac{x_{13}}{d} > 1$$

Here we normalize x_1 by the gap d to distinguish between the physical solutions (less than the gap width) from the non-physical solutions (larger than the gap width). Figure 2.8 shows a plot of the variation of the normalized static deflection of the three obtained solutions, with the DC voltage. To find the stability of the physical solutions, we first obtain the Jacobian by deriving Equation (2.11b):

$$A = J = \begin{bmatrix} 0 & 1 \\ -\frac{k}{m} + \frac{\varepsilon A V_{DC}^2}{m(d - x_1)^3} & -\frac{c}{m} \end{bmatrix} \tag{2.13}$$

Next we solve for the determinant of the eigenvalue problem and set it equal to zero:

$$\left| A - \lambda I \right| = 0 \tag{2.14}$$

$$\begin{vmatrix} -\lambda & 1 \\ -\frac{k}{m} + \frac{\varepsilon A V_{DC}^2}{m(d - x_1)^3} & -\frac{c}{m} - \lambda \end{vmatrix} = 0 \tag{2.15}$$

For zero damping ($c = 0$), we obtain:

$$\lambda_{1,2} = \pm \sqrt{\frac{\varepsilon A V_{DC}^2}{m(d - x_1)^3} - \frac{k}{m}} \tag{2.16}$$

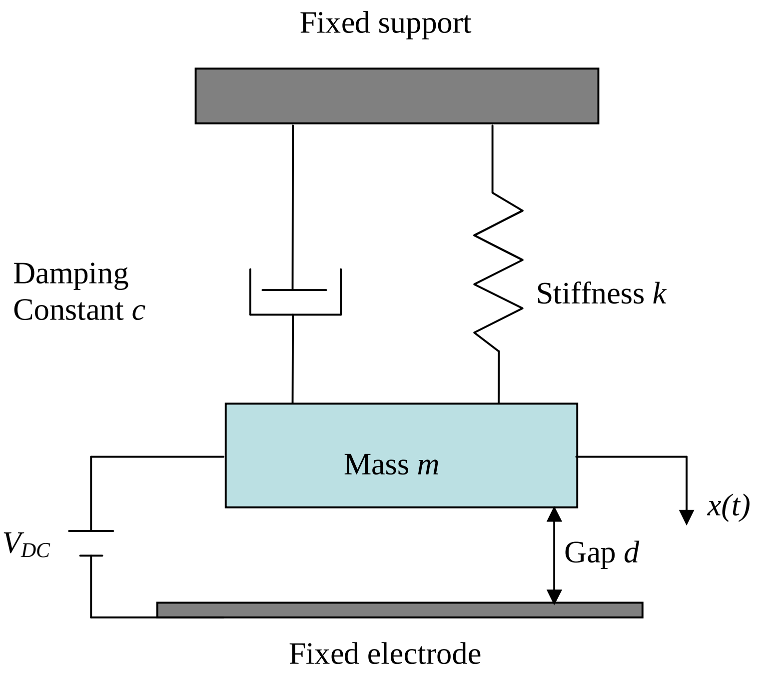

Figure 2.7: Linear one-degree-of-freedom system subjected to a force.

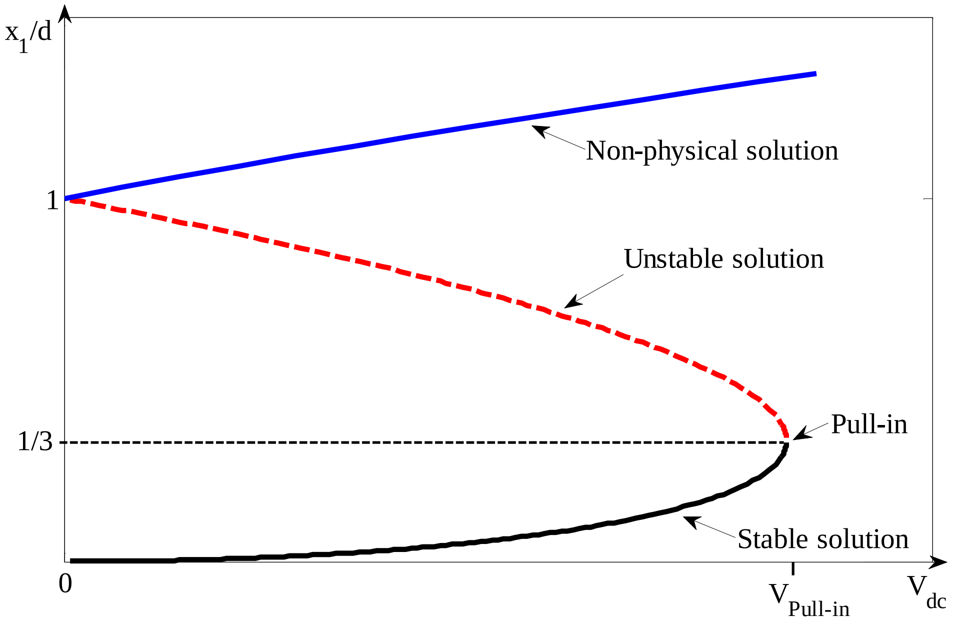

Figure 2.8: Variation of the normalized static deflection of a parallel-plate, electrostatically actuated microstructure with the DC voltage.

2.3 Squeeze Film Damping

A typical electrostatically actuated MEMS device employs two parallel-plates, a moving plate and a stationary electrode separated by a gap. The microstructure is actuated electrically by the attractive force between the electrodes. In order to increase the efficiency of actuation and improve the sensitivity of the device, the distance between the parallel plates is minimized and the surface area of the electrodes is maximized. Under such conditions, squeeze film damping effects are evident. This phenomenon is present due to the movement of the fluid underneath the plate (microbeam) which is resisted by the viscosity of the fluid. This gives rise to a pressure distribution underneath the plate which acts as a spring and/or damping force (Younis and Nayfeh, 2004). Failure in accounting for the squeeze film damping effects when modeling a MEMS device can give a very inaccurate prediction of its response. The significance of squeeze film damping effects will be highlighted later in this thesis. Figure 2.9 shows a schematic of a parallel-plate MEMS device with the presence of squeeze film damping.

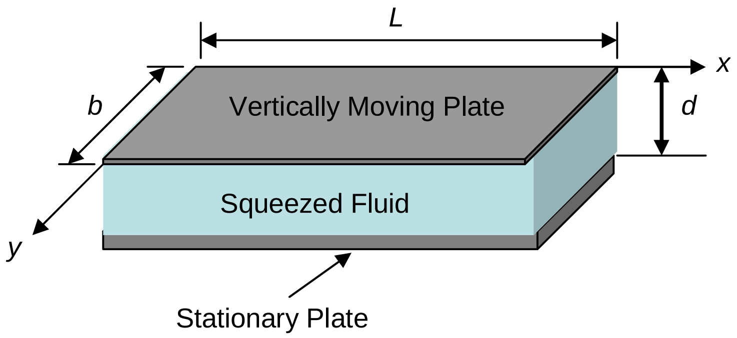

Figure 2.9: Schematic of a parallel-plate MEMS device with a squeezed fluid.

2.3.1 Blech model

Many models are available in the literature to model the effects of squeeze film damping. The one model adopted in this thesis to represent the effects of squeeze film damping is the Blech model (Blech, 1983). The Blech model defines the squeeze film term as

$$f_{squeeze} = C_{squ}(\dot{x}) \qquad (2.17)$$

where,

$$C_{squ} = \frac{64\sigma P_a A}{\pi^6 \omega_n d} \sum_{m,n,odd} \left(\frac{m^2 + n^2}{(mn)^2 \{[m^2 + n^2]^2 + \frac{\sigma^2}{\pi^4}\}} \right) \qquad (2.18)$$

and σ is the squeeze number, $\sigma = \frac{12 A \omega_n \eta}{P_a [d - x]^2}$. ere, x is the relative displacement of the microstructure and $\dot{x}$ is the relative velocity of the microstructure (Figure 2.9). The parameter P_a is the ambient pressure, ω_n is the natural frequency of the microstructure, and η is the viscosity coefficient of air.

The Blech model in Equation (2.18) above is modified to allow variation in the gap distance with the motion (Starr, 1990). Using only one term to obtain the squeeze damping coefficient has proven to accurately depict the effect of squeeze film damping. By considering only the first term of Equation (2.18), where $m = 1$ and $n=1$, the squeeze damping coefficient becomes

$$C_{squ} = \frac{64\sigma P_a A}{\pi^6 \omega_m [d - (x)]} \left(\frac{2}{\left[4 + \frac{\sigma^2}{\pi^4} \right]} \right) \qquad (2.19)$$

Table 2.1 demonstrates the difference between using one or more terms to obtain the squeeze damping coefficient and shows that using one term is sufficient. The parameters used to obtain the squeeze damping coefficient in Table 2.1 are given in the following chapter.

Table 2.1: Squeeze damping coefficient calculation.

Number of Terms	1	2	3
Squeeze Damping Coefficient	0.16998	0.17258	0.17281317

Chapter 3. Investigation of the Effects of Electrostatic Forces and Squeeze Film Damping on Microstructures

In this chapter we investigate the nonlinear effects of electrostatic forces, which behave as a negative quadratic nonlinearity, and squeeze film damping on the response of microstructures under shock. The results are illustrated in a series of shock spectra which clearly indicate how the microstructures respond. This investigation helps take MEMS designers a step forward onto realizing the reliability of their microstructures under shock and sheds light on the importance of accounting for the combined effects of shock with common MEMS nonlinearities.

3.1 Problem Formulation

We consider the modified SDOF model shown in Figure 3.1, which represents a typical electrostatically actuated parallel-plate MEMS device. The mechanical shock applied to the MEMS device can be modeled as a base excitation problem, as discussed in Chapter 2, with the equation of motion of the microstructure written as

$$m\ddot{z} + c\dot{z} + kz + f_{squeeze} = \frac{\varepsilon A V_{dc}^2}{2(d-z)^2} - m\ddot{y}(t) \qquad (3.1)$$

where ε is the dielectric constant of the gap medium, *A* is the electrode area of the microstructure, *d* is the capacitor gap width, V_{DC} is the DC polarization voltage, and *z* and $\ddot{y}(t)$ are as defined in Chapter 2. The squeeze film term $f_{squeeze}$ is expressed using the Blech model (Blech, 1983) defined in Chapter 2.

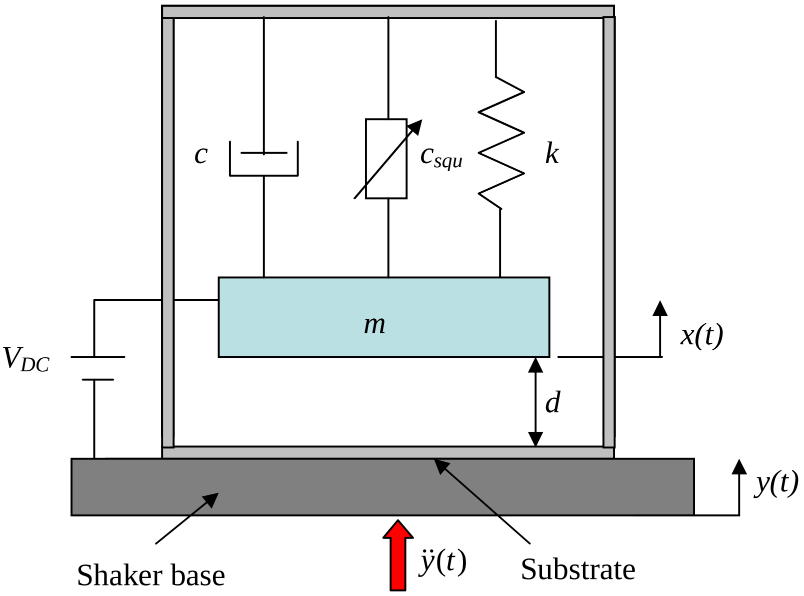

Figure 3.1: A single-degree-of-freedom model of a typical electrostatically actuated parallel-plate MEMS device.

3.2 Case Study: Capacitive Accelerometer

Three different samples of a commercial off-the-shelf capacitive accelerometer (Figure 3.2), fabricated by Sensata Technologies (Sensata Technologies), are used for the simulation and experimental investigation. We label them as sample *a*, *b*, and *c*. The samples are made up of two alloy *42* cantilever beams of thickness $150\ \mu m$ and a proof mass (approximately of length = *9.0 mm* and width *5.32 mm*) attached to their tips. The proof mass forms one side of the capacitive electrode used for detection. The samples are identical in their geometrical properties. The differences between the samples are in the stiffness of the cantilever beams and the gap separating the proof mass from the substrate.

The extraction of some of these parameters is discussed in more details in Section 3.6 of this chapter. Table 3.1 gives a summary of the different parameters for each sample.

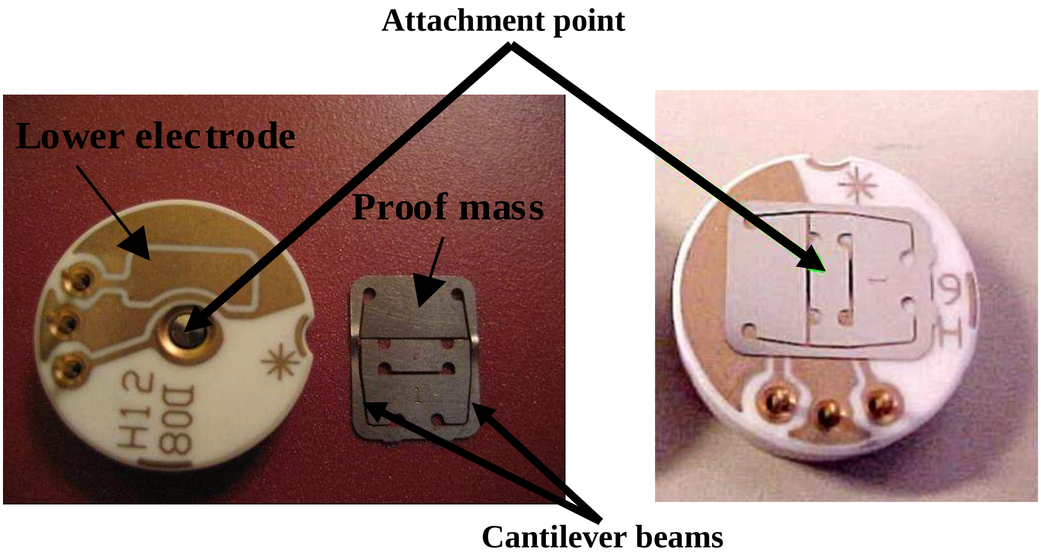

(a) (b)

Figure 3.2: (a) The capacitive accelerometer taken-apart. (b) A picture for the capacitive accelerometer, fabricated by Sensata Technologies (Sensata Technologies).

Table 3.1: Summary of extracted parameters for each sample of the capacitive accelerometer.

Parameter	Sample a	Sample b	Sample c
Stiffness k (N/m)	124	350	282
Electrode separation d (µm)	49	37.5	36.16
Natural frequency ω_{MEMS} (Hz)	187	187	187
Linear damping coefficient ζ	0.5	0.4	0.5
Pull-in voltage (Volt)	112	124.9	155

3.3 Effect of the Electrostatic Force on the Shock Spectrum under Low Damping

In this case we investigate the effect of the electrostatic force on the shock spectrum. We assume the microstructure to have a linear damping ratio of $\zeta = \frac{c}{2m\omega_n} = 0.006$. This value of low linear damping ratio is typical for a microstructure operating at reduced pressure, such as resonant sensors. Two cases of shock loads of *1 g* and *2 g* are investigated. It is worth to mention that a shock value of *3 g* is sufficient to make the proof mass of the device hit the substrate. The squeeze film damping effects are negligible in this case ($f_{squeeze} = 0$). Since Equation (3.1) is nonlinear, an analytical solution is not available. Hence, we use direct time integration of the equation of motion to obtain the shock spectrum. The direct time integration was done in Mathematica (Wolfram Research) using the second order Runge-Kutta method.

It is important to note that applying the electrostatic force causes an initial static deflection of the proof mass, and applying the shock load thereafter causes the proof mass to oscillate about its new equilibrium position due to the electrostatic force. For the purpose of comparing with experimental results, all simulated shock spectra illustrated in this paper account for this new equilibrium position by subtracting the static deflection of the proof mass due to the electrostatic force after reaching its steady state from the total response, yielding only the dynamic component of the response.

Figure 3.3 shows the simulation results of the nonlinear shock spectrum of the microstructure. The microstructure is subjected to a shock load of amplitude *1 g* and various electrostatic loads. We can note from the figure that, as we raise the applied electrostatic force, the deflection of the microstructure increases significantly and the spectrum peak shifts to the right. This behavior shows that the electrostatic force here acts as a softener to the microstructure. Young et al. (1963) observed the same behavior on a spring-mass-damper model with a cubic-softening spring term in the equation of motion. Also we can observe that as we increase V_{DC} past 80 *Volt*, the microstructure experiences pull-in for a range of shock durations. We will call this range of shock durations the pull-in zone or the escape zone. It is the zone at which the proof mass collapses onto the stationary electrode. It is important to mention that raising the electrostatic force decreases the natural frequency of the microstructure (Younis et al., 2003). To make the obtained spectra of practical use for MEMS designers, all simulated shock spectra illustrated in this paper are normalized by the fundamental natural period of the microstructure at zero voltage (T_n at V_{DC} of *0 Volt*). Hence, the knowledge of the natural frequency of the structure before actuation is enough to be able to use these curves.

Next we examine the effect of increasing the shock amplitude by subjecting the microstructure to a shock load of *2 g*. We observe from Figure 3.4 the same behavior as with the *1 g* shock load. However, the microstructure in this case pulls-in at a lower voltage of about *45 Volt*. This agrees with the results reported in (Younis et al., 2006, 2007) about the influence of both shock and electrostatic forces.

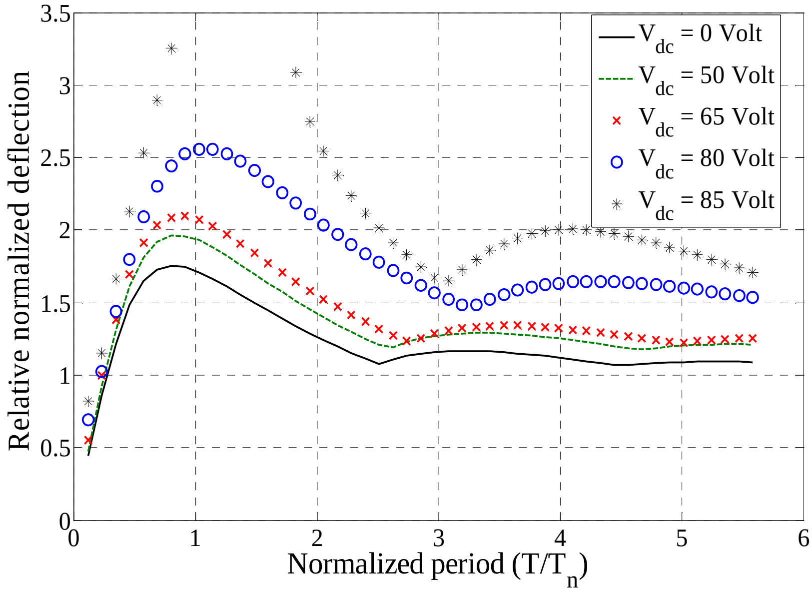

Figure 3.3: Nonlinear shock spectra of a capacitive accelerometer when subjected to a shock of *1 g* and various electrostatic loads (*ζ = 0.006*).

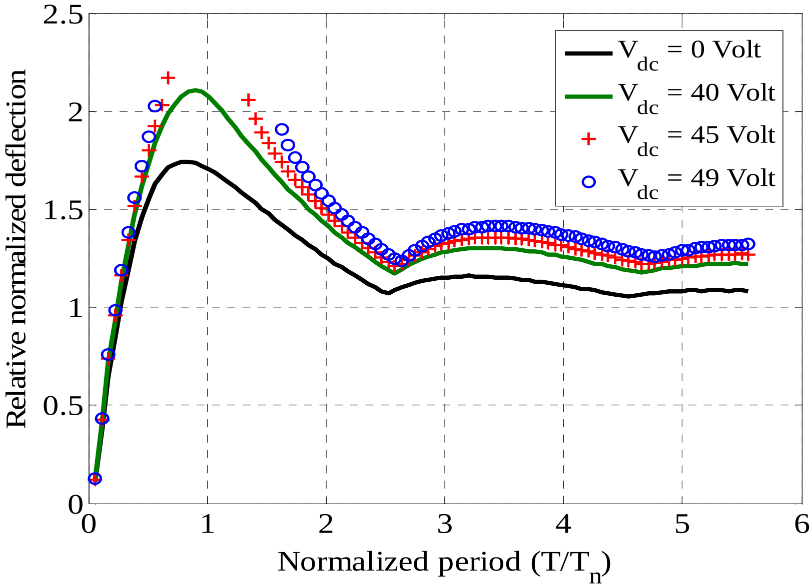

Figure 3.4: Nonlinear shock spectra of a capacitive accelerometer when subjected to a shock of $2\ g$ and various electrostatic loads ($\zeta = 0.006$).

3.4 Effect of Squeeze Film Damping on the Response of the Capacitive Accelerometer

Next we demonstrate the squeeze film damping effects on the response of the microstructure when operated in air at atmospheric pressure P_a without electrostatic force. The SQFD is modeled using the Blech model (Blech, 1983), which is defined in details in Chapter 2. It is a highly nonlinear phenomenon, related to the motion of the microstructure. In the case of the capacitive accelerometer, if the proof mass is moving away from the substrate, SQFD has small effect. However; if the proof mass moves towards the substrate, SQFD becomes significant. Figure 3.5 shows previously obtained experimental and simulation results, which give a clearer explanation to the behavior of SQFD (Younis et al., 2007).

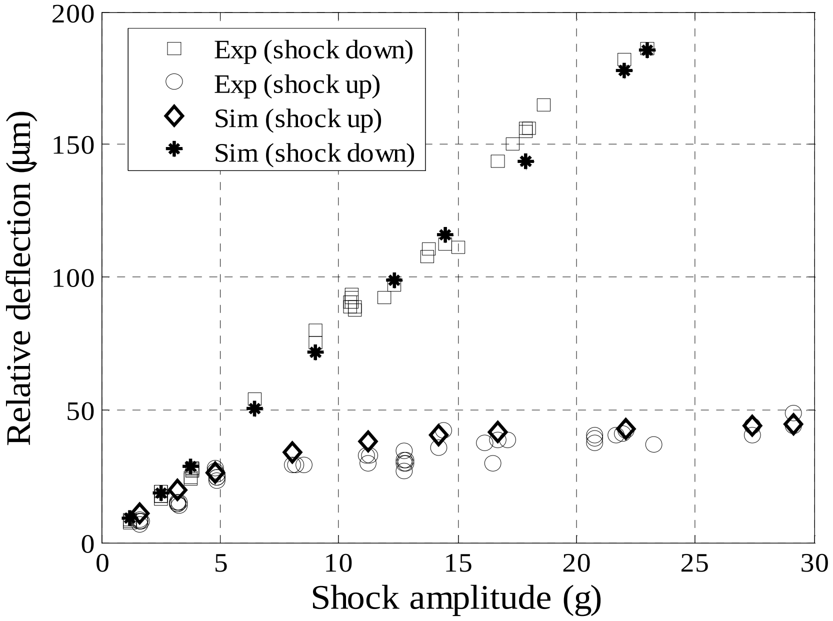

Figure 3.5: Simulation results (stars and diamonds) and experimental data (circles and squares) of the proof mass deflection with shock amplitude when *T = 5.0 ms*, when operated in air at atmospheric pressure P_a. In the figure, shock down means the proof mass moves away from the substrate (Younis et al., 2007)

3.5 Effect of the Electrostatic Force and Squeeze Film Damping on the Shock Spectrum

Next, we examine the combined effects of the electrostatic force and squeeze film damping. We use a linear damping value of *0.4*, which is obtained experimentally for the capacitive accelerometer (Younis et al., 2007), in addition to the SQFD term. Figures 3.6 and 3.7 depict the nonlinear spectrum of the MEMS device when subjected to shock loads of *1 g* and *3 g* respectively. By comparing Figures 3.3 and 3.6, we note that in Figure 3.3, with a voltage of 85 *Volt*, the microstructure reaches pull-in while in Figure 3.7, at a voltage of 90 *Volt*, the normalized defection does not exceed a ratio of *1.8* (no pull-in). This clearly indicates that SQFD suppresses the motion of the microstructure.

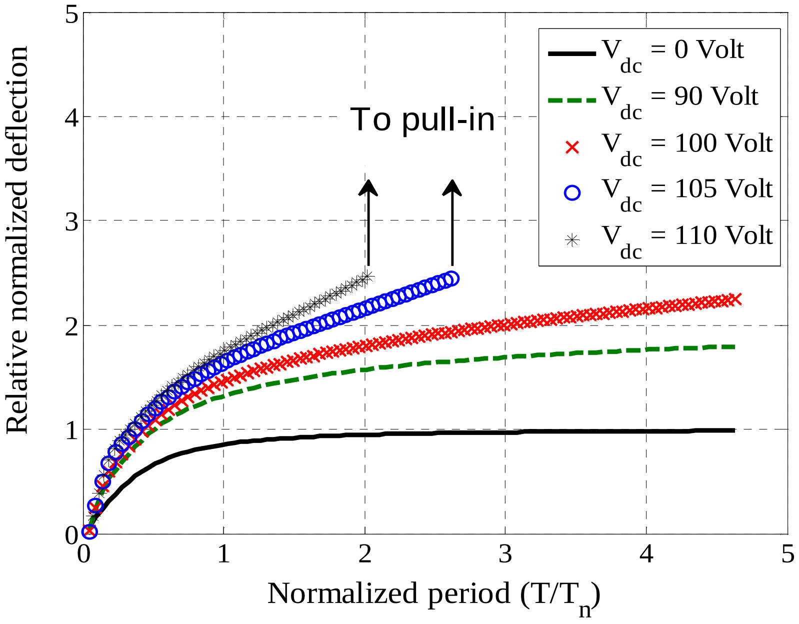

Figure 3.6: Nonlinear shock spectra of a capacitive accelerometer when subjected to a shock of *1 g* and various electrostatic loads assuming squeeze film damping effect and $\zeta = 0.4$.

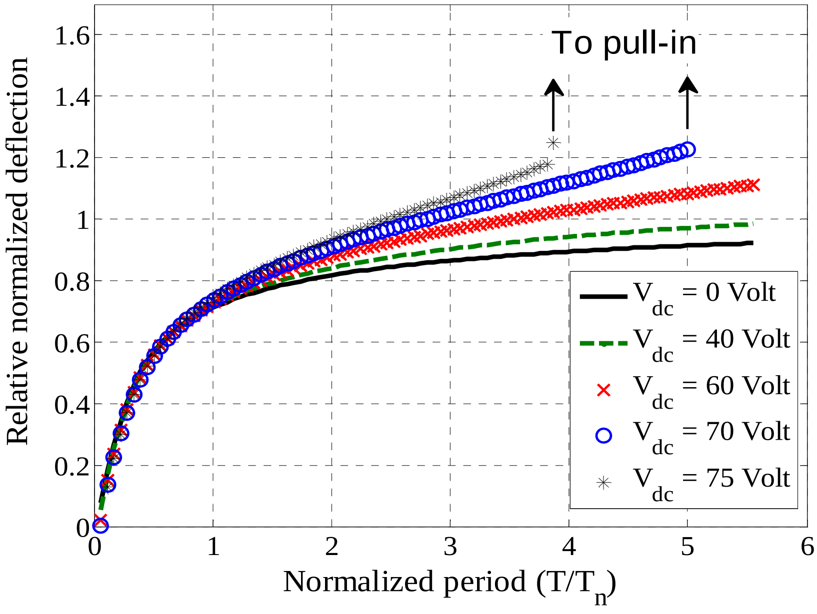

Figure 3.7: Nonlinear shock spectra of a capacitive accelerometer when subjected to a shock of *3 g* and various electrostatic loads assuming squeeze film damping effect and $\zeta = 0.4$.

Furthermore, the effects of squeeze film damping are highly influenced by the dynamic behaviors of the microstructure. However, they are almost negligible in the quasi-static behavior, which is well illustrated through Figures 3.6 and 3.7. If we take a closer look at Figure 3.6, we note that the microstructure at an applied voltage of *100 Volt* is approaching pull-in in the quasi-static region and its deflection is highly suppressed in the dynamic region. Due to this behavior, the nonlinear spectrum does not have pull-in zones similar to those observed in Figures 3.3 and 3.4, because once the microstructure pulls-in at a given shock duration, it will continue to do so for longer shock durations, where the response will always be quasi-static.

3.6 Experimental Results on the Effects of Electrostatic Forces and Squeeze Film Damping

Several experiments were conducted to extract key parameters of the capacitive accelerometer, which were used throughout this paper in the simulations. Experimental work was also conducted to compare theory to experimental data. The following sections discuss the details of the experimental setup, the parameters extraction, and results.

3.6.1 Experimental setup

Figures 3.8a and 3.8b show the experimental setup used to investigate the effects of electrostatic forces and squeeze film damping on the response of the capacitive accelerometer when operated in atmospheric pressure. The device was mounted on a shaker head and connected to a V_{DC} supply via a small electrical circuit. Current limiting resistors were used in the circuit to avoid failure of the device in the case of pull-in. A reference accelerometer was also mounted on the shaker head to monitor the value of shock applied to the device. A laser vibrometer was used to monitor the response of the device proof mass. All input and output signals were controlled using the LabView software and through a Data Acquisition (DAQ) card.

Figures 3.9a and 3.9b show the experimental setup used to investigate the effect of electrostatic forces on the capacitive accelerometer in reduced pressure environment (negligible squeeze film damping). The setup is similar to the previous one. However in this case, a small shaker was placed inside a vacuum chamber. The vacuum chamber is equipped with a window made of quartz glass to allow the penetration of the laser signal without distortion.

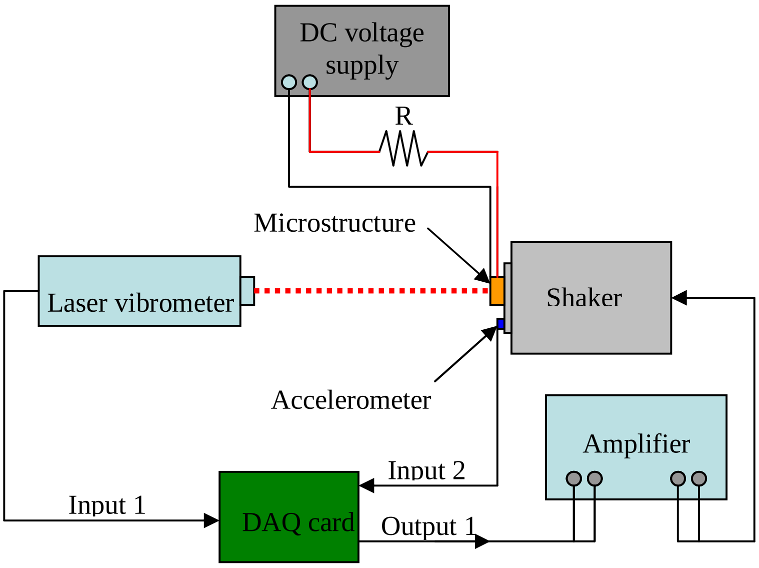

(a)

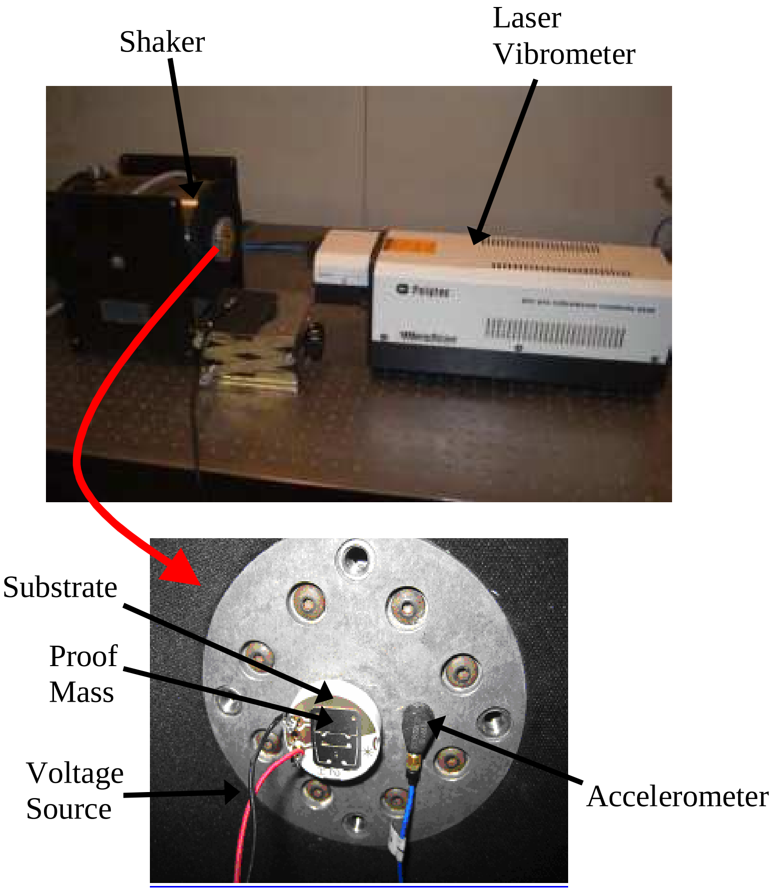

(b)

Figure 3.8: (a) Schematic of the experimental setup and the data acquisition system. (b) A picture of the experimental setup used for testing the device in air.

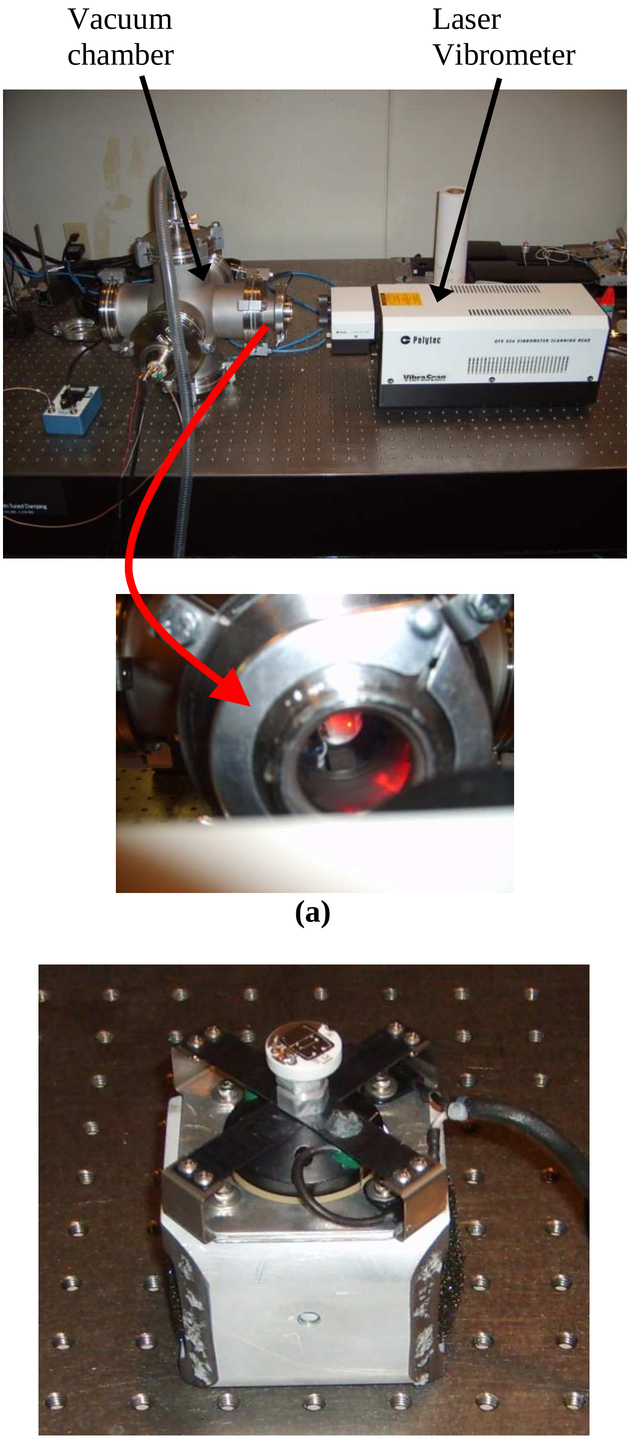

Figure 3.9: (a) A picture of the experimental setup used for testing the capacitive accelerometer at reduced pressure. (b) A picture of the shaker used to generate shock pulses inside the vacuum chamber.

3.6.2 Parameter extraction

The first parameter extracted was the cantilevers stiffness, which are attached to the proof mass. The device was actuated using various V_{DC}, and the transient response of the proof mass was monitored using the laser vibrometer. Figure 3.10 shows the data obtained experimentally for sample *b*. The stable solution of Equation (3.2), which is the static version of Equation (3.1), was used to curve fit the experimental data. Based on this, a stiffness coefficient *k* of *350 N/m* was obtained.

$$z^3 - 2dz^2 + d^2 z - \frac{\varepsilon A V_{dc}^2}{2k} = 0 \tag{3.2}$$

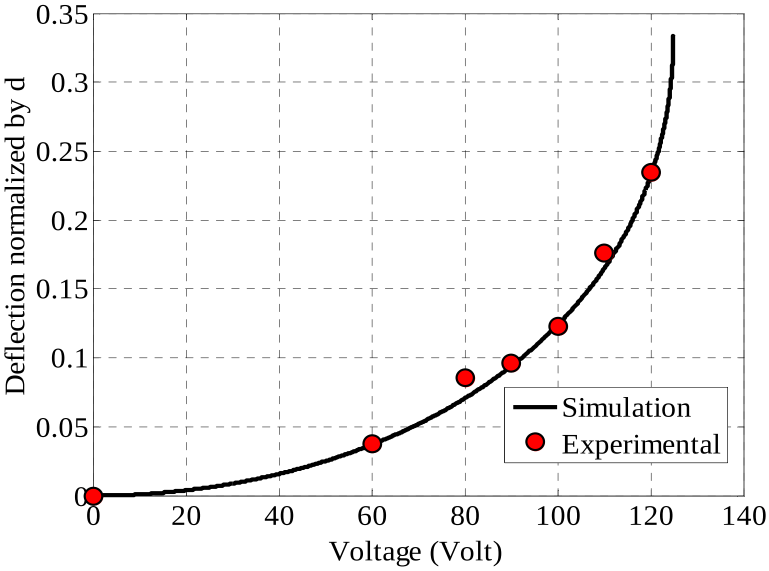

Figure 3.10: Variation of the proof mass displacement normalized by the gap spacing underneath the proof mass *d* for various values of V_{DC}. Shown in the figure both the simulation and experimental data.

To measure the gap width *d*, which separates the proof mass from the stationary electrode, a high V_{DC} beyond pull-in was applied. Figure 3.11 shows the transient response of the proof mass, which was monitored using the laser vibrometer. As indicated in the figure, the gap *d* is close to $37.5\ \mu m$ for sample *b*.

Finally, the vibration response of the device was measured to identify the natural frequency and linear damping ratio (Younis et al., 2007). A continuous random signal was used to drive the shaker. Using a curve fitting technique, the fundamental natural frequency of the device was found to be *187 Hz*, with an estimated linear damping ratio (ζ) of about *0.4* for sample *b*.

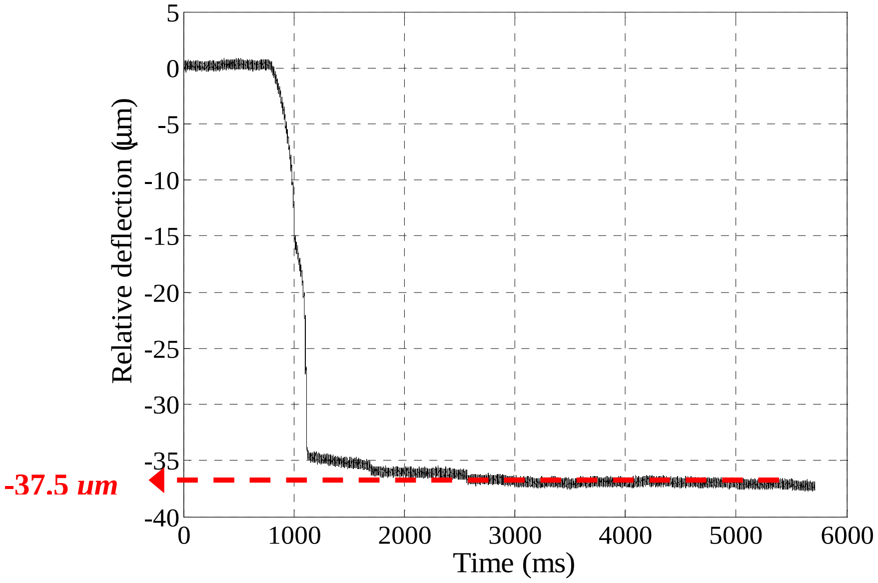

Figure 3.11: The measured transient response of the proof mass for a voltage beyond the pull-in voltage.

3.6.3 Results and comparison with simulation

As explained in Section 3.6.1, the device was first actuated by V_{DC} then after the proof mass reaches steady state, the mechanical shock was applied using the shaker. The applied shock pulses were dependent on the shock duration. For large shock durations, the shock pulse was a full sine shape, while for small shock durations the shock pulse was of a half-sine pulse shape. The transient response was monitored. Two displacement measurements were obtained using the laser vibrometer, one for the absolute motion of the accelerometer and the other for the substrate motion. By subtracting the two measurements, the displacement of the proof mass relative to the substrate was obtained. Figures 3.12a and 3.12b show an example of an applied shock and the corresponding transient response of the microstructure, respectively.

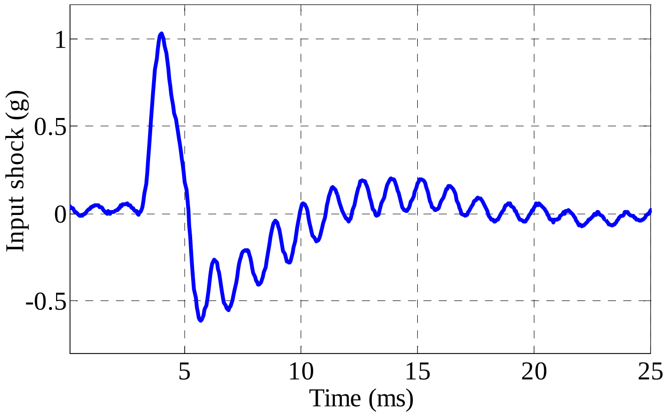

(a)

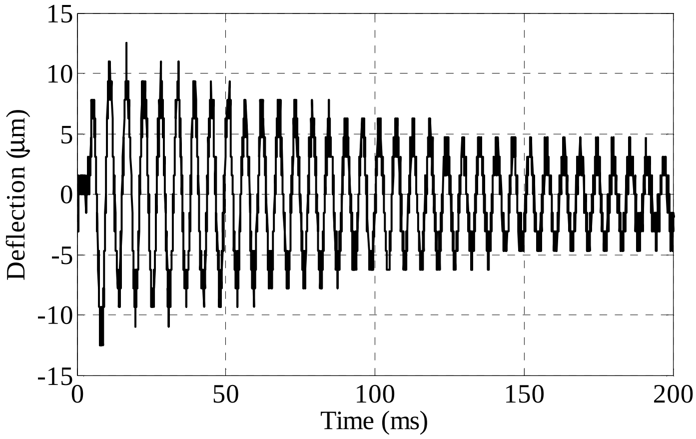

(b)

Figure 3.12: (a) Applied shock of *1 g* at a shock duration of *T = 2.2 ms*. (b) Transient response of the proof mass of sample *b* when subjected to mechanical shock at *80 Volt,* as monitored through the laser Doppler vibrometer. The measured value of pressure is equal *176 mtorr*.

3.6.3.1 Effect of electrostatic forces on the shock spectrum in reduced pressure conditions

Here, the device is operated on the setup of Figure 3.9 (inside the vacuum chamber). Figures 3.13-3.15 compare the simulation and experimental results, where the device was subjected to a mechanical shock of *1 g* and V_{DC} of *0 Volt, 80 Volt,* and *85 Volt,* respectively. In Figures 3.13-3.15, the dynamic amplitude response is normalized by an equivalent static response of a static force with the same magnitude as the shock. The figures show good agreement between simulation and experimental results. We notice from Figure 3.15 that the experiment and simulation deviate slightly in predicting the pull-in zone. This can be attributed to the fractal nature of dynamic pull-in, which makes it depend on the initial conditions of the system. Another aspect contributing to this deviation is due to the shaker used. The shaker induced a magnetic field which in turn affected the response of the microstructure, acting almost as a damper, opposing the microstructure from reaching pull-in.

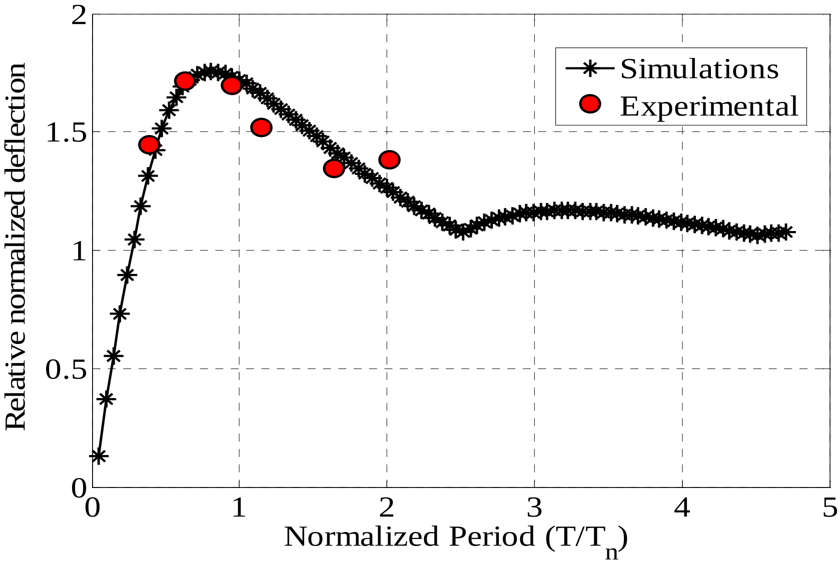

Figure 3.13: Simulation versus experimental results for the accelerometer shock spectrum when subjected to a shock of *1 g* at *0 Volt*. The measured value of pressure is equal *190 mtorr*.

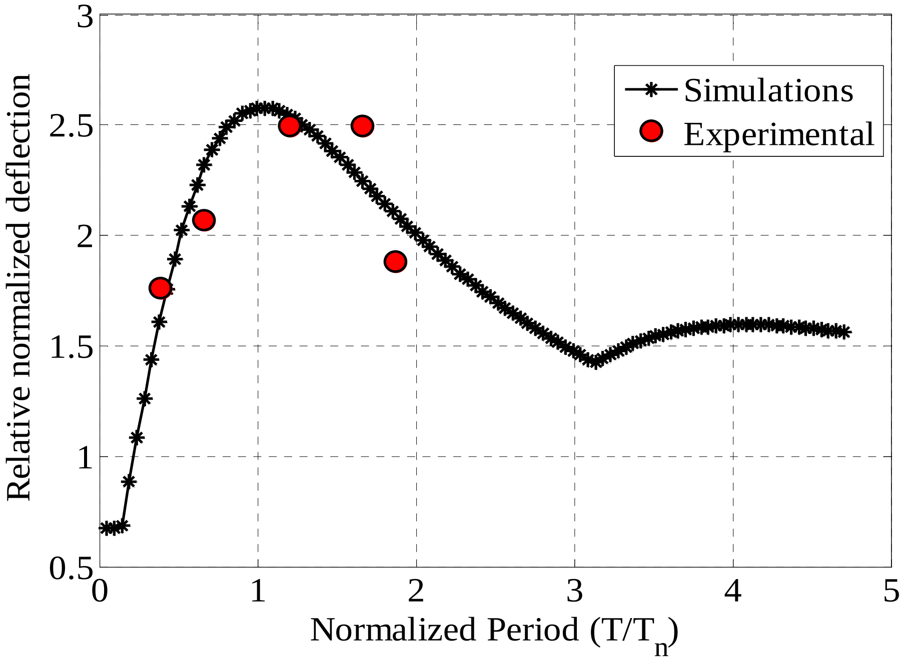

Figure 3.14: Simulation versus experimental results for the accelerometer shock spectrum when subjected to a shock of *1 g* at *80 Volt*. The measured value of pressure is equal *176 mtorr*.

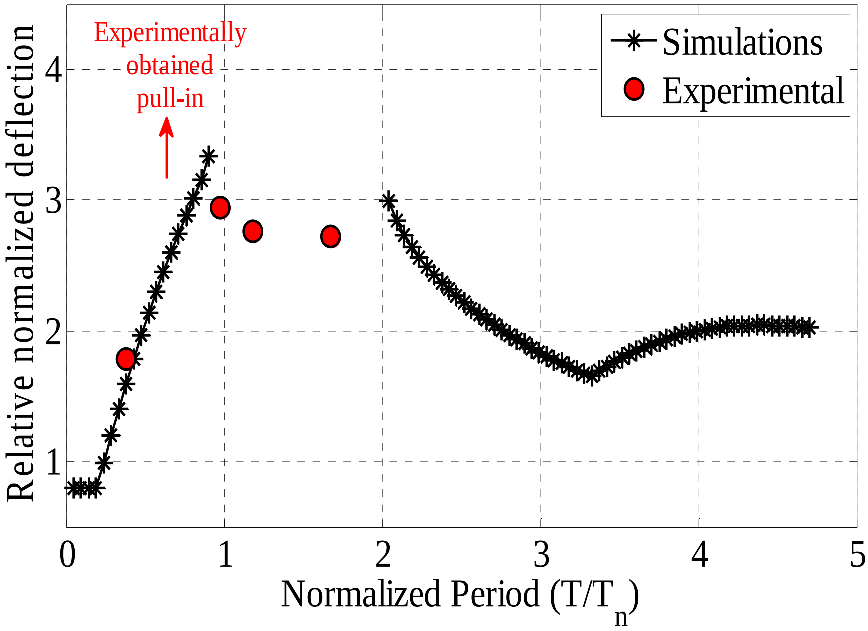

Figure 3.15: Simulation versus experimental results for the accelerometer shock spectrum when subjected to a shock of *1 g* at *85 Volt*. The measured value of pressure is equal *169 mtorr*.

3.6.3.2 Effect of electrostatic forces and squeeze film damping on the shock spectrum

Here, the device is tested in atmospheric pressure P_a using the setup shown in Figure 3.8. Figures 3.16 and 3.17 compare the simulation and experimental results, where the device was subjected to a mechanical shock of *3 g* and V_{DC} of *0 Volt* and *60 Volt*, respectively. The figures show good agreement between simulation and experimental results. Furthermore, this proves the observed behavior through simulations, where the increase of the actuation V_{DC} softens the device, causing larger deflections.

It is important to note that the experimental data was obtained only for a small range of shock durations due to restrictions of both the shaker and laser vibrometer. For large shock durations, the response was quasi-static when subtracting the two measurements, which was not well captured by the laser vibrometer. When the shock duration was too small, it was close to the natural period of the shaker, which caused disturbances in the signal. In Section 3.6.3.1, experimental results were obtained even for small shock durations because a different shaker was used that fits inside the vacuum chamber.

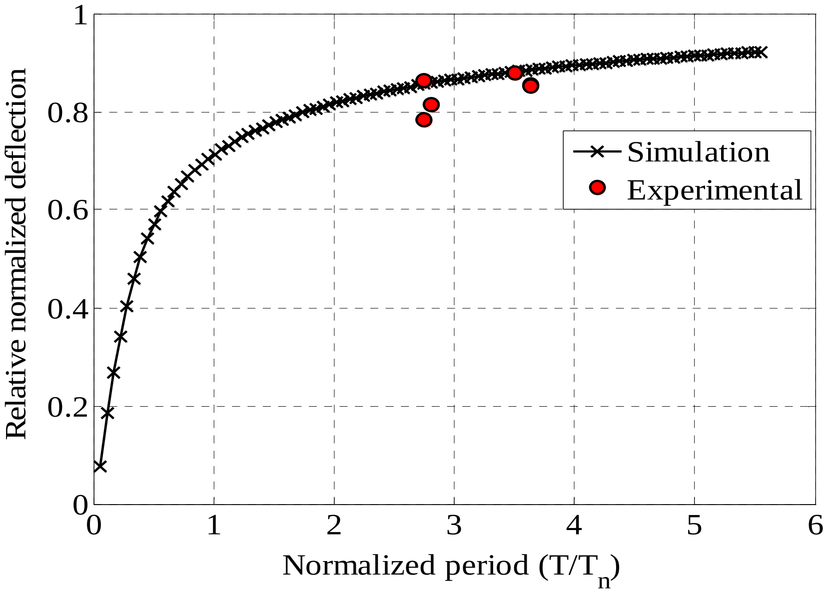

Figure 3.16: Simulation versus experimental results for the accelerometer shock spectrum when subjected to a shock of *3 g* at *0 Volt*, while operating at ambient pressure *P$_a$*.

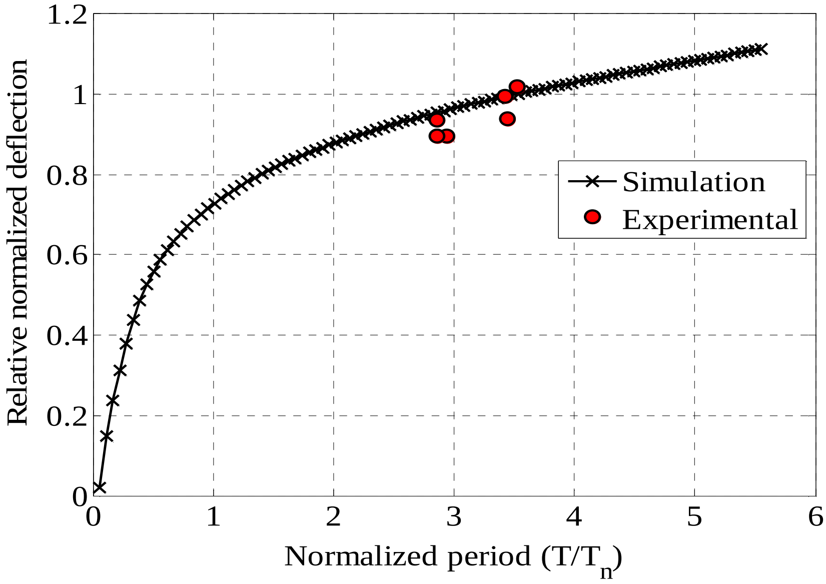

Figure 3.17: Simulation versus experimental results for the accelerometer shock spectrum when subjected to a shock of *3 g* at *60 Volt*, while operating at ambient pressure *P$_a$*.

Chapter 4. Investigation on the Effect of PCB Motion on Microstructures

A typical microstructure of a commercialized device is packaged and placed on a printed circuit board (PCB) as shown in Figure 4.1. Because the microstructure and the PCB are flexible structures, the interaction of their motion can be significant. This section aims to understand the motion consequences due to the motion of the PCB in response to shock, which may cause stiction and short circuit problems due to the impact of microstructures among themselves and with the substrate.

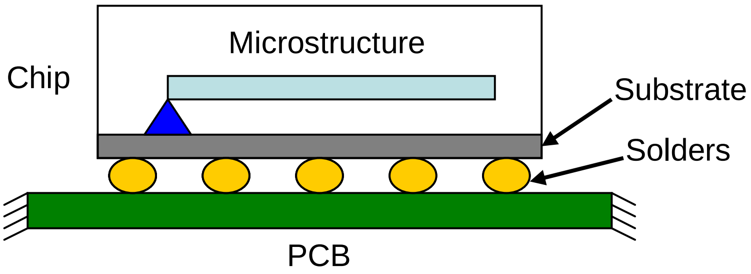

Figure 4.1: Schematic of a typical microstructure mounted on a printed circuit board.

4.1 Problem Formulation

We use a 2-DOF model, Figure 4.2, to study the PCB effect on the response of a MEMS device under shock load (Alsaleem, 2007). The first DOF accounts for the PCB motion and the second DOF represents the motion of the microstructure, such as a beam or a plate, which is mounted over the PCB. Shown in Figure 4.2 are k_m: microstructure stiffness, k_{PC} : PCB stiffness, c_m: microstructure damping, c_{PC} : PCB damping, m_m:

microstructure mass and m_{PC}: PCB mass. In this model, we assume the MEMS device to be placed on the center of the PCB, which represents a worst-case scenario. The governing equations of motion of the system are given by

$$m_m \ddot{x}_m + k_m (x_m - x_{PC}) + c_m (\dot{x}_m - \dot{x}_{PC}) = 0 \tag{4.1}$$

$$\begin{aligned} m_p \ddot{x}_2 - k_m (x_m - x_{PC}) - c_m (\dot{x}_m - \dot{x}_{PC}) \\ + k_{PC} x_{PC} + c_{PC} \dot{x}_{PC} = k_{PC} y + c_{PC} \dot{y} \end{aligned} \tag{4.2}$$

where y and $\dot{y}$ are the displacement and velocity of the assembly base, respectively, x_m represents the motion of the microstructure and x_{PC} represents the motion of the PCB. The base acceleration $\ddot{y}$ is assumed to be a half sine pulse of amplitude A_o, as defined in Chapter 2. Equations (4.1) and (4.2) are integrated numerically with time to obtain the dynamic response.

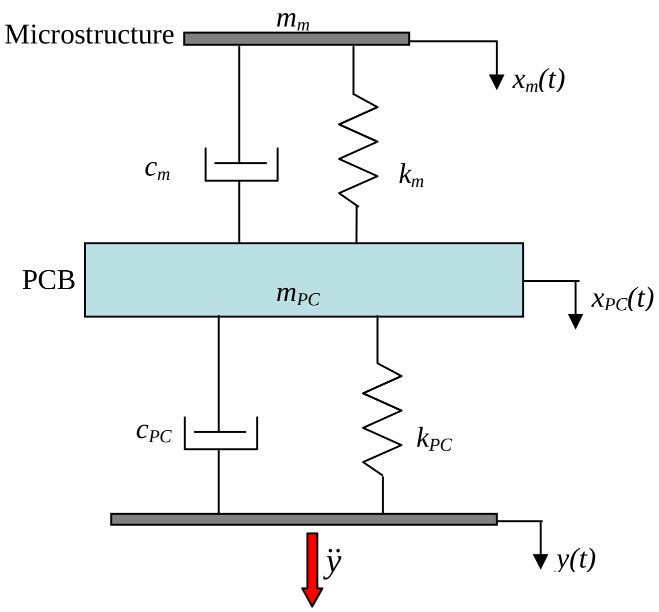

Figure 4.2: MEMS-PCB assembly subjected to a base acceleration.

4.2 Simulation and Experimental Results

Two PCBs shown in Figure 4.3 were used to investigate the effect of the PCB motion on the motion of sample *a* of the capacitive accelerometer. This work has been conducted in collaboration with Mr. Alsaleem from our group (Alsaleem et al., 2009). The first investigation was using PCB1 shown in Figure 4.3a, which has a natural frequency of *6 kHz*, that is far from the accelerometer's natural frequency with a ratio of $\omega_P / \omega_{MEMs} = 6\ kHz/\ 187\ Hz = 32$. The accelerometer was mounted over PCB1, and the PCB was fixed using four screws to the head of the shaker. Figure 4.4 compares simulation and experimental results for the shock spectrum of the accelerometer with and without being mounted on the PCB. This figure shows a good agreement between simulation and experimental results. Figures 4.4a and 4.4b show that with the high ratio between the PCB and accelerometer's natural frequency, the PCB has no effect on the accelerometer motion, i.e., it transfers the shock load to the MEMS device without any alteration (Alsaleem et al., 2009).

(a) PCB1 ($\omega_P = 6\ kHz$) **(b) PCB2 ($\omega_P = 230\ Hz$)**

Figure 4.3: A picture for the two PCBs used for testing. Figure 4.3b shows PCB2 placed over the shaker head.

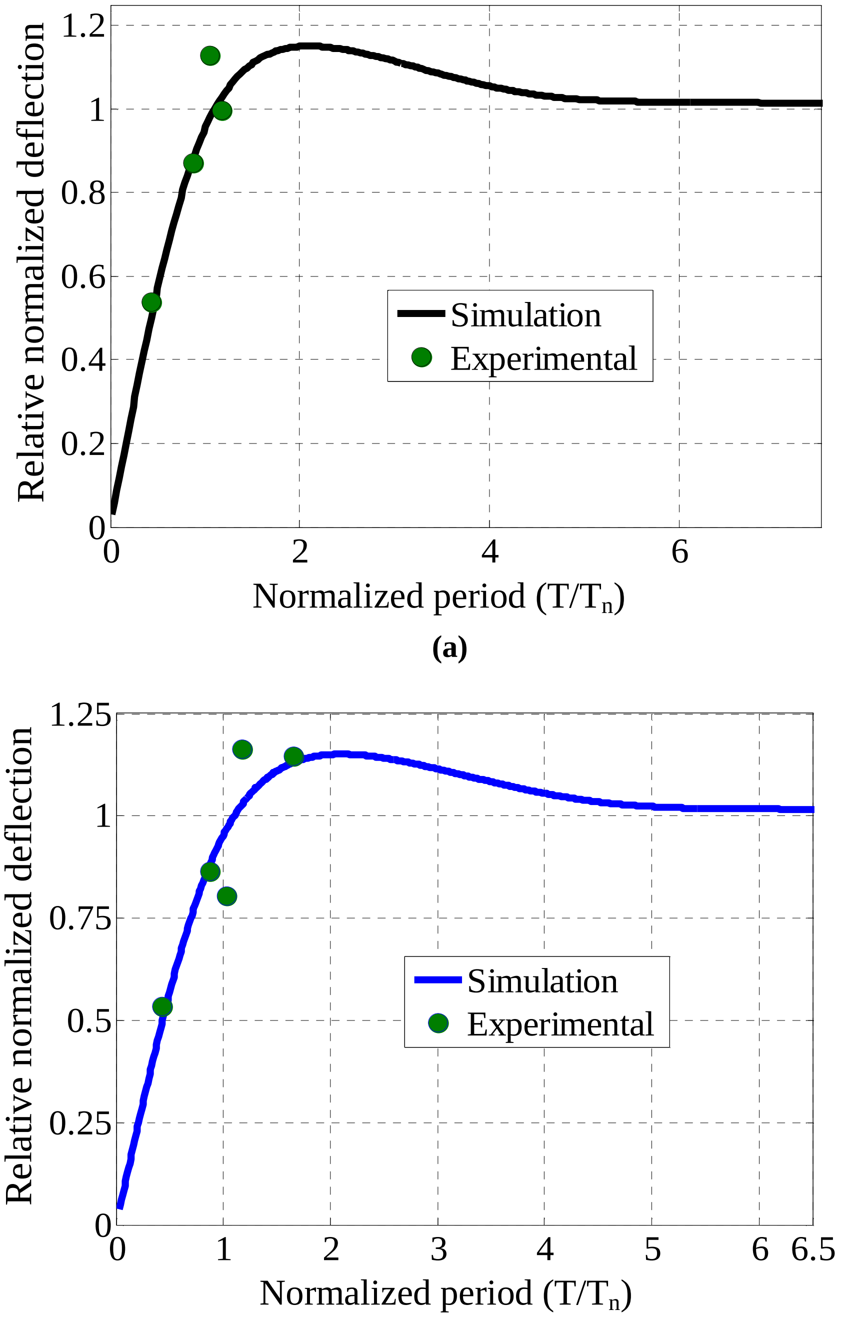

(a)

(b)

Figure 4.4: Shock spectrum of sample *a* obtained theoretically and experimentally. (a) Including the PCB effect. (b) Without including the PCB effect.

Next, the accelerometer was mounted over PCB2 shown in Figure 4.3b. The ratio of the natural frequency of PCB2 to the accelerometer's natural frequency is *1.23*. Figure 4.5 compares simulation and experimental results for the shock spectrum of the accelerometer when mounted on PCB2. This figure shows a good agreement between simulation and experimental results. In a comparison between Figures 4.4b and 4.5 we find that at this specific ratio between the PCB and MEMS device, the response of the microstructure is amplified. This is because the natural frequency of the PCB is near that of the microstructure.

Figure 4.6 shows a sample of the transient response of the device with PCB2 (dynamic response amplification) and without PCB2 (static response with no amplification), due to shock loads of $T = 5.0\ ms$. This figure shows a significant amplification for the response of the device due to the dynamic effect of the poor-designed PCB. Note that without a PCB, the device responds quasi-statically to shock loads. Hence, the PCB here has adverse effect on the performance of the device. The figure shows a drift in the measurement where the microstructure reaches a transient response of about $-20\ \mu m$, while it should reach zero. This is due to the laser vibrometer not restarting from zero with every measurement. We can also observe from the figure a nonlinear behavior in the microstructure response with a PCB. This behavior is characterized by the fact that the microstructure is able to deflect freely away from the substrate reaching a relative deflection of $-100\ \mu m$ while it is suppressed going towards the substrate and that is due to the presence of SQFD.

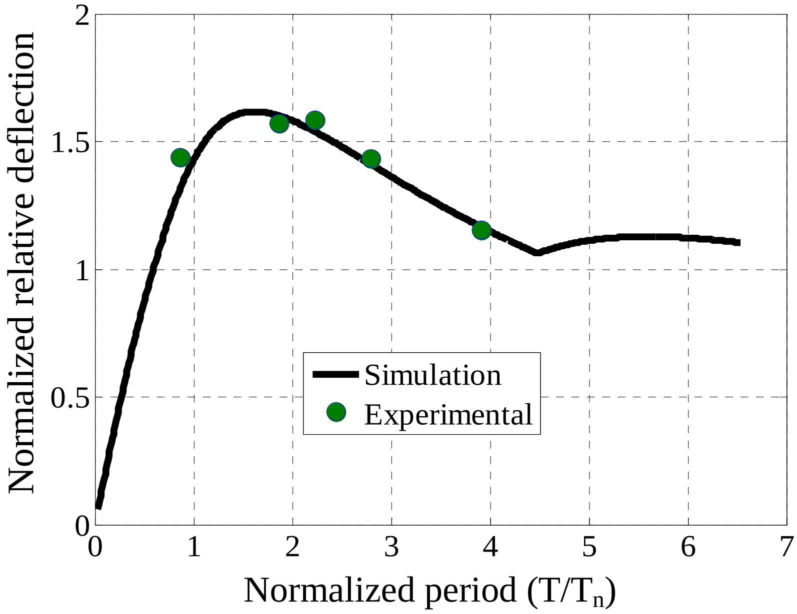

Figure 4.5: Simulation Vs experimental results for the shock spectrum of sample *a* including the effect of PCB2.

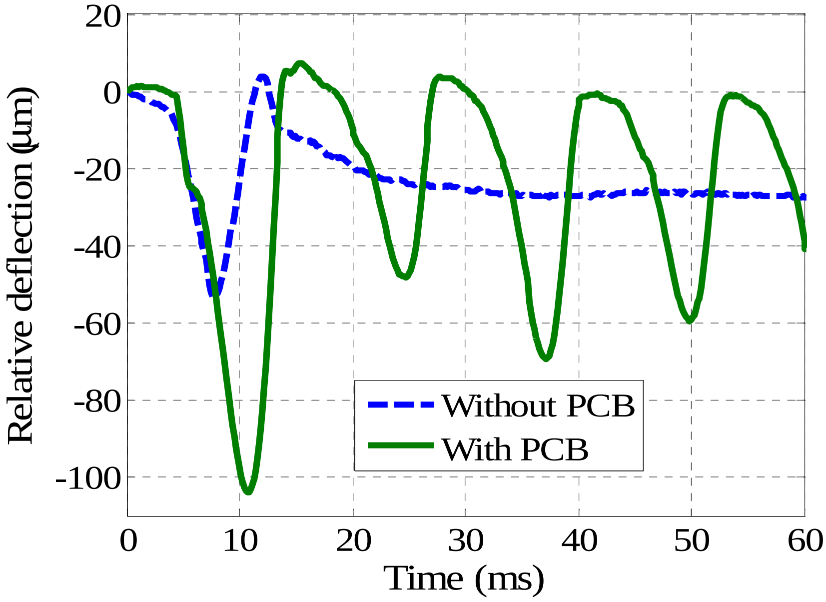

Figure 4.6: Transient response of the microstructure with and without PCB2, when subjected to a mechanical shock as monitored through a Laser Doppler Vibrometer (*T = 5.0 ms*).

Chapter 5. Enhancing the Sensitivity of a Resonant Accelerometer and its Use as a Switch

In this chapter we investigate the sensitivity enhancement of a resonant accelerometer by operating it in the nonlinear regime. The accelerometer is excited by a DC load superimposed to an AC harmonic load. The operation of the accelerometer at both primary and sub-harmonic resonance is investigated. The concept of the nonlinear excitation is demonstrated by simulation on a commercial capacitive accelerometer. This chapter also focuses on the use of the nonlinearities arising from the electrostatic forces to realize a switch triggered by acceleration.

5.1 Problem Formulation

We begin by considering the SDOF model shown in Figure 5.1, utilized to represent a structure of linear stiffness, which can be a microstructure of a MEMS device. This model is similar to the model adopted by Sung and Lee (2000).

The governing equation of motion of the microstructure can be written as

$$m\ddot{x} + c\dot{x} + kx = \frac{\varepsilon A(V_{DC} + V_{AC}\cos\Omega t)^2}{2(d-x)^2} + ma \tag{5.1}$$

where x is the deflection of the proof mass, the superscript dot denotes time derivative, m is the mass, c is the viscous damper coefficient, k is the stiffness of the microstructure, ε is the dielectric constant of the gap medium, A is the electrode area of the microstructure, d is the capacitor gap width, V_{DC} is the DC polarization voltage, and a represents the input acceleration. The input acceleration here is considered a constant value, which can be assumed as a mechanical shock with a large shock duration (quasi-static). The parameters V_{AC} and Ω are the AC harmonic load amplitude and frequency, respectively.

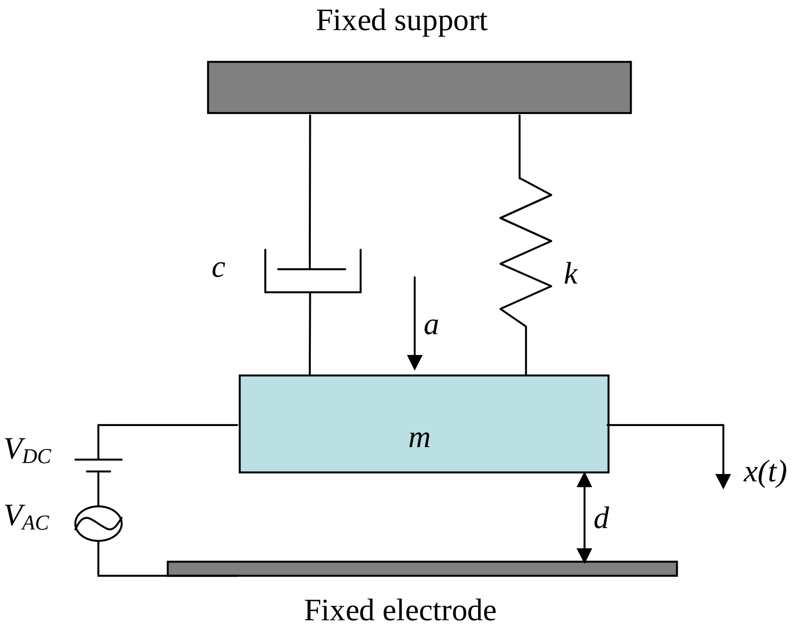

Figure 5.1: A single-degree-of-freedom model (SDOF) of a typical parallel-plate MEMS resonator actuated electrically.

In order to obtain the natural frequency of the microstructure, the response *x(t)* is assumed to be composed of a dynamic term x_d and a static term x_s. Substituting for ($x = x_d + x_s$) in Equation (5.1) we obtain:

$$m\ddot{x}_d + c\dot{x}_d + k(x_d + x_s) = \frac{\varepsilon A(V_{DC} + V_{AC} Cos\Omega t)^2}{2(d - x_d - x_s)^2} + ma \tag{5.2}$$

Next we use Taylor series expansion of the electrostatic force term about $x_d = 0$, which yields:

$$\frac{1}{2(d-x_d-x_s)^2}=\frac{1}{2}\left[\frac{1}{(d-x_s)^2}+\frac{2x_d}{(d-x_s)^3}+....\right] \tag{5.3}$$

where the higher order and nonlinear terms of the electrostatic force have been neglected. Substituting Equation (5.3) into Equation (5.2) yields the static and linearized dynamic equations of motion as follows:

$$\text{Static:}\quad kx_s=\frac{\varepsilon A V_{DC}{}^2}{2(d-x_s)^2}+ma \tag{5.4}$$

$$\text{Dynamic:}\quad m\ddot{x}_d+c\dot{x}_d+kx_d=\frac{\varepsilon A(V_{DC}+V_{AC}Cos\Omega t)^2}{2(d-x_s)^2}x_d \tag{5.5}$$

The static component has three possible solutions, one of which is a non-physical solution, as illustrated in Chapter 2. Figure 5.2 shows the other physical solutions. As seen in the figure, one of the solutions is stable and the other one is unstable. The stable solution will be used for the calculation of the natural frequency as shown below.

We note from Equation (5.5) that the effective stiffness of the resonator is given by

$$k_{eff}=k-\frac{\varepsilon A V_{DC}{}^2}{(d-x_s)^3} \tag{5.6}$$

The effective stiffness expression is next used to approximate the natural frequency of the microstructure as follows

$$\omega_n=\sqrt{\frac{k}{m}-\frac{\varepsilon A V_{DC}^2}{m(d-x_s)^3}} \tag{5.7}$$

As seen from Equation (5.7), the natural frequency of the microstructure decreases as we raise the DC voltage, which is known as a softening behavior (Younis et al., 2003). The working principle of the resonant accelerometer is as follows; an externally applied acceleration will change the equilibrium position of the resonator, as indicated by

Equation (5.4), particularly it will increase the value of x_s. This in turn will cause a decrease in the linear natural frequency of the resonator, as indicated by Equation (5.7). This shift in frequency can be related to the applied acceleration.

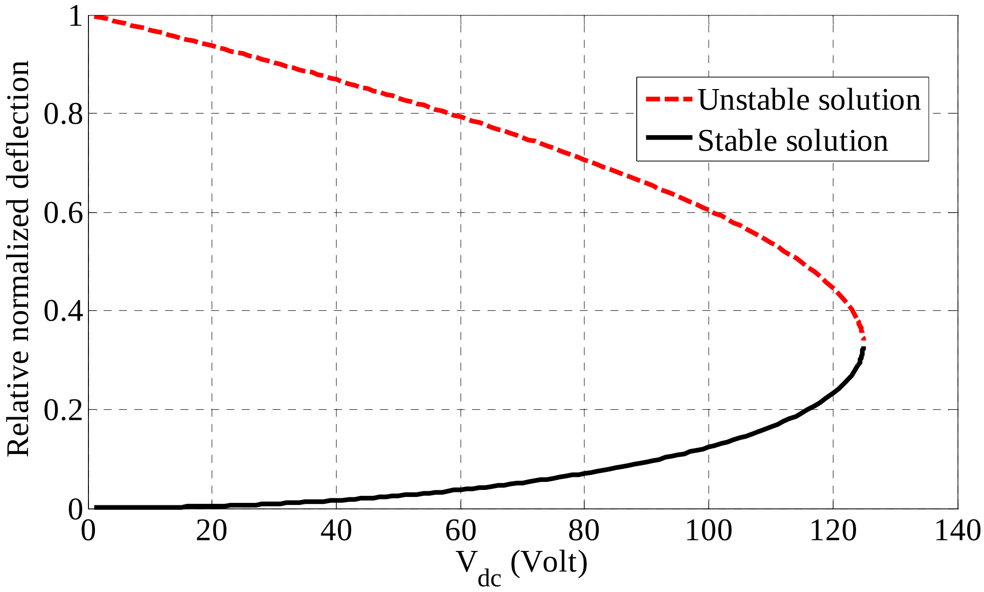

Figure 5.2: Variation of the normalized static deflection of the capacitive accelerometer with the DC voltage.

5.2 Simulation Results

In order to obtain a highly sensitive resonant accelerometer, investigations are conducted to monitor the effects of DC voltage, AC voltage, and acceleration on the frequency response curve of the microstructure. Analysis is first conducted using the linearized model of Equations (5.4) and (5.7), which assumes small values of AC voltages, to explore the effect of the DC voltage on the natural frequency. This mode of operation with small values of AC load represents the traditional method for operating resonant sensors (Burns and Horning, 1995).

Then, large values of AC voltages are assumed. In this case, the linearized model does not apply and therefore, we perform direct time integration based on the 4th order Runge-Kutta technique for the equation of motion, Equation (5.1), to calculate the frequency response curve of the resonator before and after the external acceleration and determine the difference in the resonance frequency.

As a case study, we use the mechanical parameters of sample *b* of the commercial capacitive accelerometer discussed in Chapter 3. A damping ratio of *0.05* is also assumed.

5.2.1 The effect of the DC voltage and acceleration on the resonant frequency

In this section we investigate the effects of the DC voltage on the resonant frequency of the microstructure under an applied acceleration based on Equations (5.4) and (5.7).

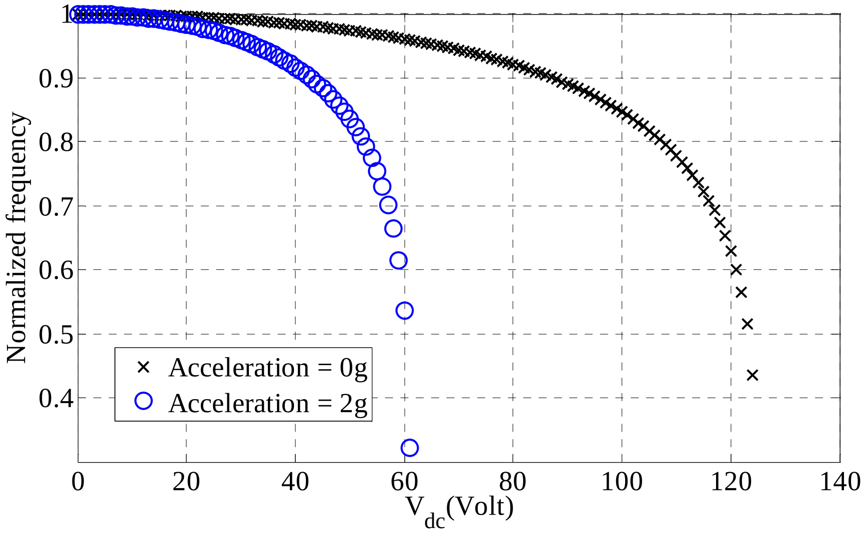

Figure 5.3: Variation of the normalized frequency with the DC voltage for various values of acceleration.

Figure 5.3 shows the resonant frequency of the microstructure normalized by the natural frequency of *187 Hz* versus the applied DC voltage, for various accelerations. We can observe that under zero acceleration, the change in the resonant frequency increases as the voltage increases and the resonant frequency approaches zero at the pull-in voltage (Younis et al., 2007). For an applied acceleration of *2 g*, we observe the same behavior, however, the change in resonant frequency is more sensitive to the applied voltage and pull-in is reduced to about *60 Volt*.

Next, we further investigate the effect of acceleration on the resonant frequency of the microstructure under an applied DC voltage. Figure 5.4 shows the normalized frequency versus the applied acceleration for various DC voltages. We observe through the figure that increasing the applied acceleration has the same effect as applying DC voltage. The applied acceleration softens the microstructure and causes a change in its resonant frequency.

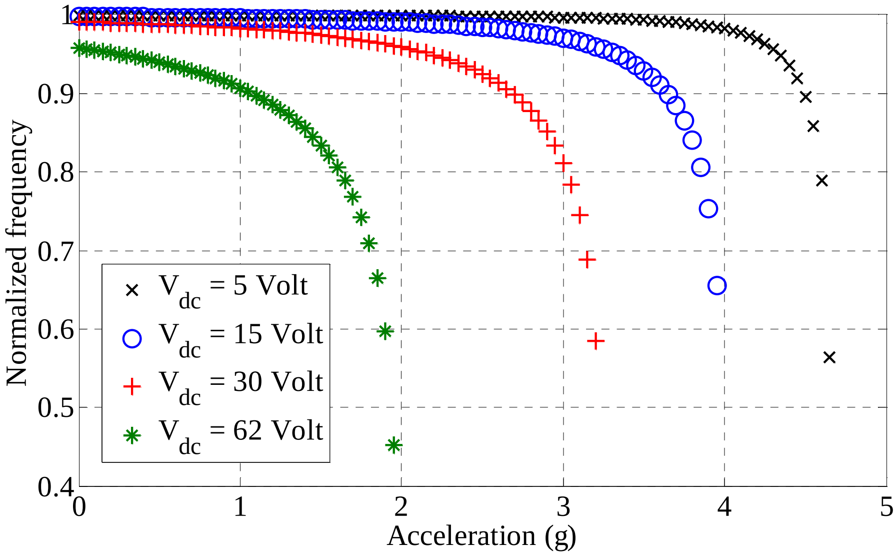

Figure 5.4: Variation of the normalized frequency with acceleration for various DC voltages.

5.2.2 The effect of AC load on the frequency response

Figure 5.5 gives a schematic of the frequency response shift due to acceleration and shows the difference between a linear shift, which can be obtained using long-time integration, and the nonlinear shift (bend) in the frequency response curve which can only be obtained using whether shooting or long-time integration. However, it is estimated more accurately using the shooting method of Section 5.3.

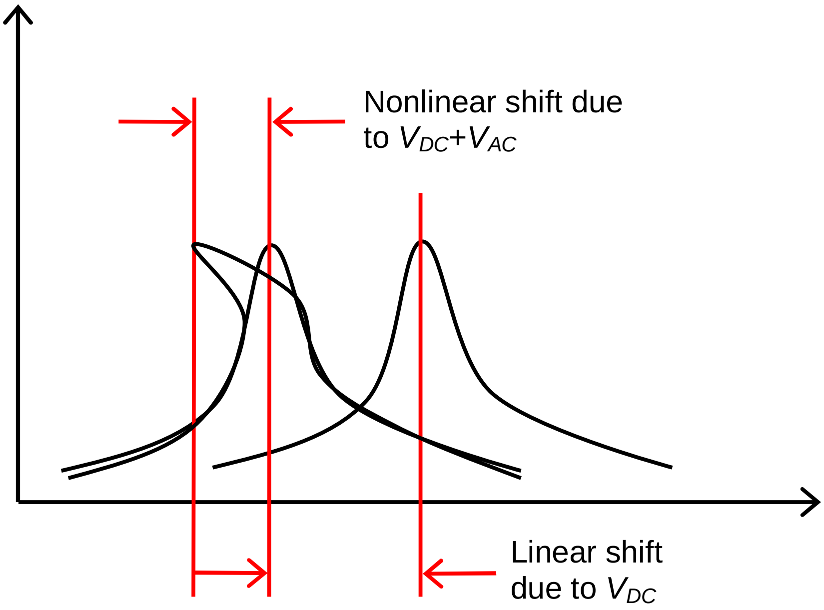

Figure 5.5: A schematic showing the difference between a linear and a nonlinear shift in the frequency response plot.

The linearized model introduced in the previous section is sufficient in showing the effects of DC voltage and acceleration on the resonant frequency of the microstructure; however, it is not capable of capturing the nonlinear effect of the AC harmonic load. Figure 5.6 shows a comparison at a DC voltage of *30 Volt*, between the linearized model and the frequency response model, for two values of AC harmonic loading. It is clear that for a small AC load, the models are in good agreement. However, as the AC load is raised to higher values, there is significant deviation between the two models.

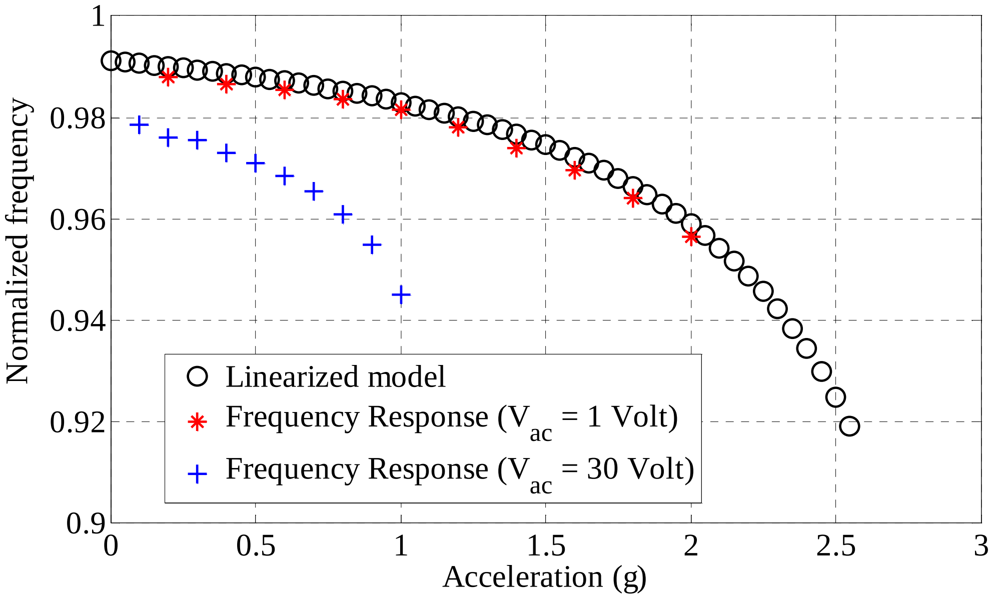

Figure 5.6: A comparison of the resonant frequency predicted using a linearized model to that using the forced-response model.

In the following section, the effects of DC voltage, AC harmonic load and acceleration are investigated. For each DC voltage a number of AC harmonic loads are applied and the sensitivity of the microstructure under acceleration is studied. Equation (5.1) was integrated numerically for a long time using Runge-Kutta scheme to obtain a steady-state solution.

5.2.2.1 DC voltage of 30 Volt

At an applied DC voltage of *30 Volt*, two AC harmonic loads of *20 Volt* and *40 Volt* were applied and the sensitivity of the device to acceleration under these loading conditions is shown in Figure 5.7. It is important to mention that for each given AC harmonic load, the last data point in Figure 5.7 is the limit of acceleration which the accelerometer can withstand, beyond which it experiences pull-in. In other words, taking the case of *40 Volt* in Figure 5.7 as an example, an applied acceleration of *0.6 g* is the limit of stable operation of the accelerometer, beyond which the accelerometer undergoes pull-in. This behavior can be used to our advantage, if we intend to realize a trigger or a switch.

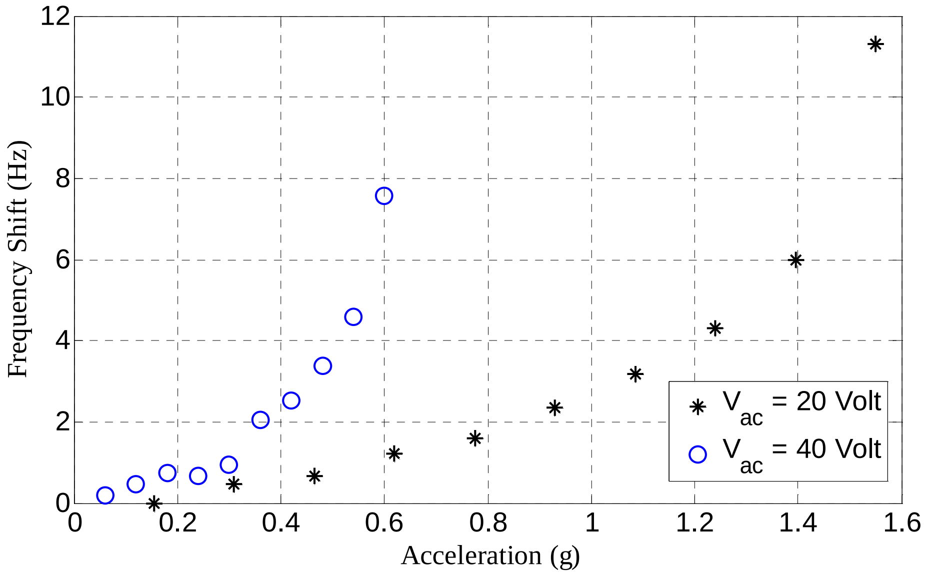

Figure 5.7: Device sensitivity to acceleration at a V_{DC} of *30 Volt* and for various AC harmonic loads.

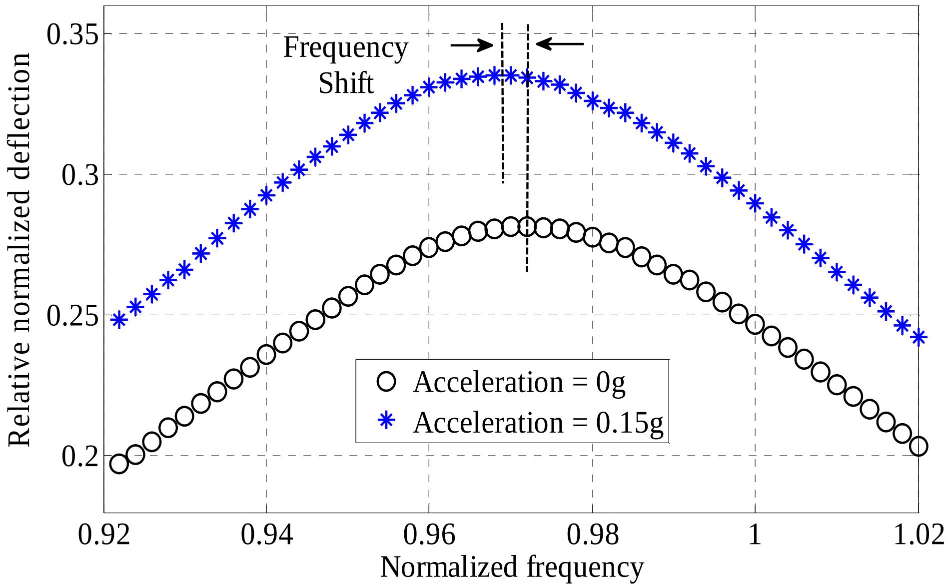

Figure 5.8: Frequency response curves showing the resonant frequency shift between *0 g* and *0.15 g*, for an applied V_{DC} of *30 Volt* and V_{AC} of *40 Volt*.

The frequency shifts shown in Figures 5.8 and 5.9 each represents one point in Figure 5.7. By comparing the two figures, we can note that increasing the applied acceleration raises the frequency shift, which was demonstrated through the linearized model. If we look at Figure 5.6 at an applied acceleration of *0.6 g*, we find that the frequency shift at an AC voltage of *40 Volt* is about *7.8 Hz*, while at a voltage of *20 Volt*, it is only *1 Hz*. The frequency shift is significantly increased by raising the AC loading. This clearly shows that increasing the AC harmonic load raises the sensitivity of the device.

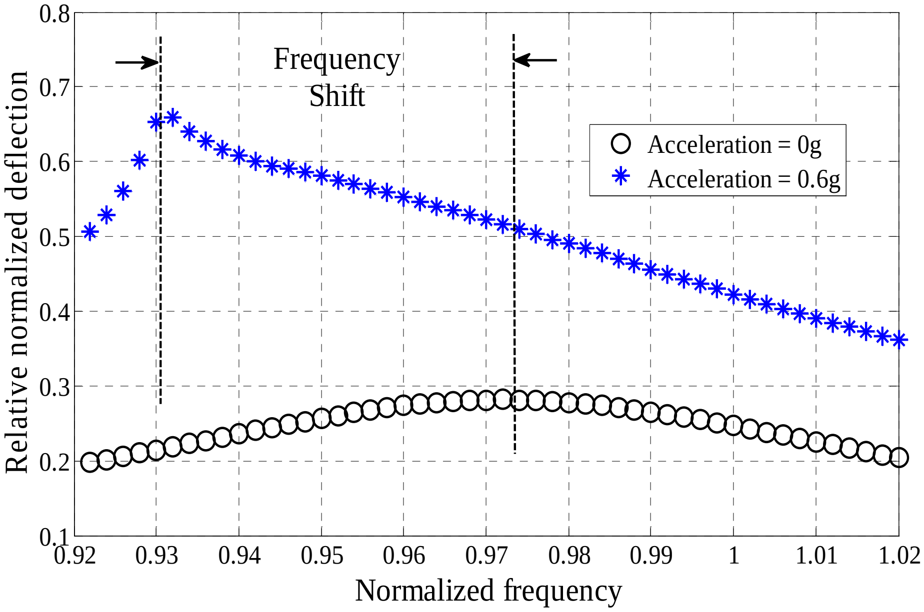

Figure 5.9: Frequency response curves showing the resonant frequency shift between *0 g* and *0.6 g*, at an applied V_{DC} of *30 Volt* and V_{AC} of *40 Volt*.

The nonlinearities introduced by the electrostatic force and the AC harmonic loading are now more apparent in the frequency response model. Figure 5.9 shows a typical softening behavior at an applied acceleration of *0.6 g*. It is important to note that hysteresis was not reached in any of the obtained frequency response curves, i.e. the simulation results were the same while sweeping the frequency forward and backward.

5.2.2.2 DC voltage of 40 Volt

For an applied DC voltage of *40 Volt*, AC harmonic loads of *20 Volt*, *30 Volt*, and *40 Volt* were used and the sensitivity of the device to acceleration under these loading conditions is shown in Figure 5.10. We observe the same behavior when raising the AC harmonic load. It is clear however that also raising the DC voltage enhances the sensitivity of the device. Figure 5.11 shows a closer look for the case of an applied acceleration of *0.16 g*. As seen in the figure, the frequency shift is about *5.4 Hz*, while in Figure 5.7, at the same applied harmonic load and acceleration, the frequency shift is less than *0.6 Hz*. This is also illustrated visually by comparing Figures 5.8 and 5.12, where for the same applied harmonic load and acceleration, the frequency shift is larger for the higher DC voltage of *40 Volt*, compared to *30 Volt*. We can also observe the same behavior in Figure 5.10, as in Figure 5.7. For each given AC harmonic load, raising the acceleration brings the accelerometer closer to its limit of stable operation, unless once again we intend to use it as a trigger or a switch.

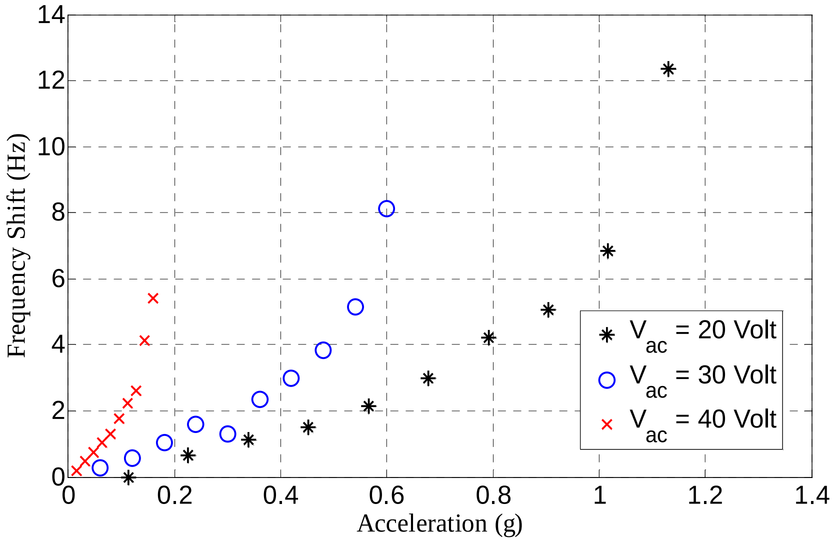

Figure 5.10: Device sensitivity to acceleration at a V_{DC} of *40 Volt* and for various AC harmonic loads.

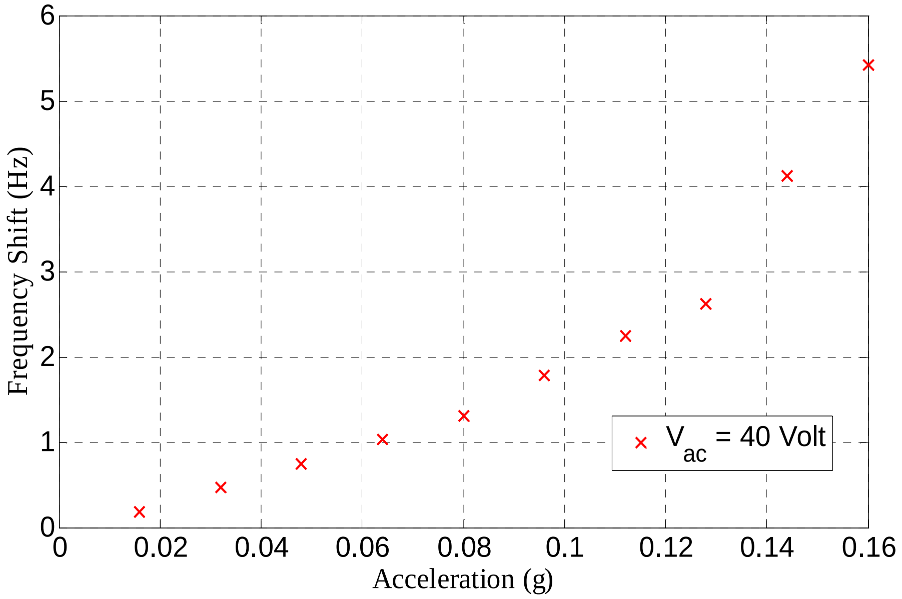

Figure 5.11: A closer view of Figure 5.10 for a V_{AC} of *40 Volt*.

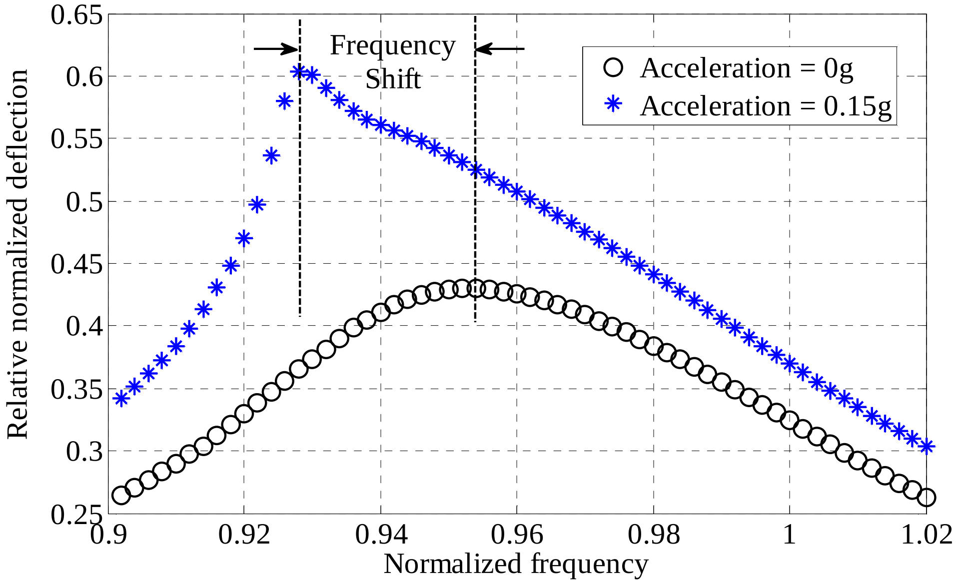

Figure 5.12: Frequency response curves showing the resonant frequency shift between *0 g* and *0.15 g*, at an applied V_{DC} of *40 Volt* and V_{AC} of *40 Volt*.

5.2.2.3 *DC voltage of 50 Volt*

Finally, the last DC voltage investigated was *50 Volt*, with AC harmonic loads of *20 Volt*, *25 Volt*, *30 Volt*, and *34 Volt*. The sensitivity of the device to acceleration under these loading conditions is shown in Figure 5.13. The same conclusions are drawn on the effects of the AC harmonic loading, DC voltage and acceleration. The major addition of this analysis is that it shows the highest sensitivity reached which is illustrated in Figure 5.14. It shows that the device at a DC voltage of *50 Volt* and an AC harmonic load of *34 Volt* is sensitive to applied accelerations as small as *0.02 g*, giving a frequency shift at that value of about *1.75 Hz*. Once again we find the same behavior as observed earlier, raising the acceleration brings the accelerometer closer to its limit of stable operation, beyond which it experiences pull-in.

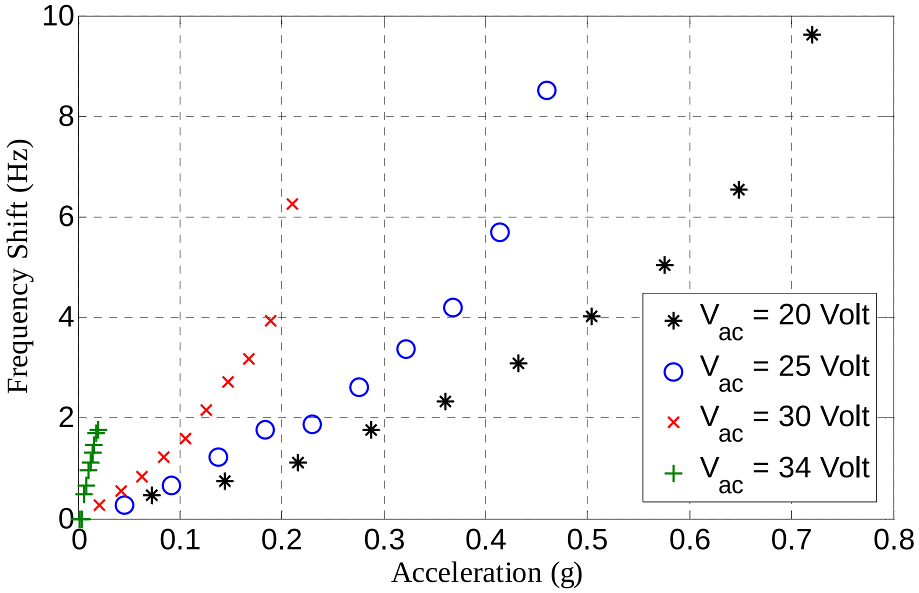

Figure 5.13: Device sensitivity to acceleration at a V_{DC} of *30 Volt* and for various AC harmonic loads.

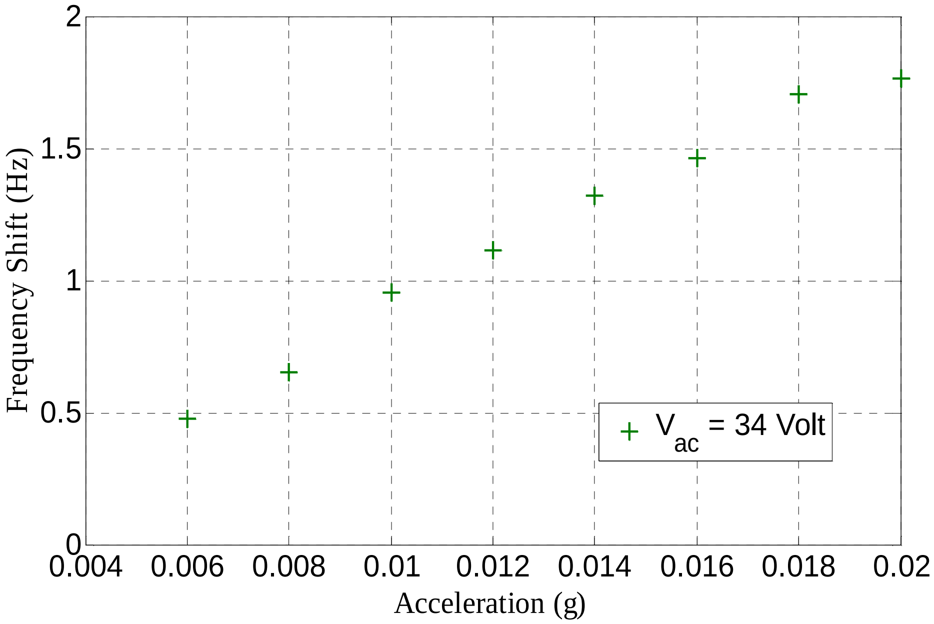

Figure 5.14: A closer view of Figure 5.12 for a V_{AC} of *34 Volt*.

5.3 Shooting Technique

In the previous section, long-time intergation was used to investigate the sensitivity of the accelerometer to acceleration as we raise the electrostatic forces. The one disadvantage in using long-time intergation is that it does not allow accurate investigation of the nonlinear region of the frequency response curve. For the purpose of investigating accurately the nonlinear region in the frequency response curve we introduce the shooting technique (Nayfeh and Balachandran, 1995). The shooting technique captures a periodic solution (orbit) of period $T = 2\pi/\Omega$, where Ω is the excitation frequency. It is called shooting because it is based on searching (shooting) for an appropriate set of initial conditions that can result in a periodic motion for the system. In this technique, initial guesses for the initial conditions are first supplied to the scheme and then they are corrected using a Newton-Raphson method. Convergence is achieved when the difference between the newly corrected set of initial guesses and the previous ones diminishes to very small values. Once a periodic motion is captured, its stability is determined using the Floquet theory. Next, we discuss the procedure as it is applied to the equation of motion of the resonator studied in this chapter.

We utilize a nonlinear single-degree-of-freedom model to simulate the resonator response due to V_{DC} plus V_{AC} electric loading. The equation of motion governing the behavior of the resonator can be written as

$$m\ddot{x} + c\dot{x} + kx = \frac{\varepsilon A[V_{DC} + V_{AC}\cos(\Omega t)]^2}{2(d - x)^2} \tag{5.8}$$

For convenience, we normalize the equation of motion by introducing nondimensional variables (denoted by superscript ^) as below

$$\hat{x} = \frac{x}{d}\ ,\ \hat{t} = \frac{t}{T} \tag{5.9}$$

where $T = 2\pi / \omega_n$ and $\omega_n = \sqrt{k/m}$. Substituting Equation (5.9) in (5.8) yields the nondimensional equation of motion:

$$\ddot{\hat{x}} + \hat{c}\dot{\hat{x}} + \hat{x} = \alpha \frac{[V_{DC} + V_{AC}\cos(\Omega\hat{t})]^2}{(1 - \hat{x})^2} \tag{5.10}$$

where $\hat{c} = 2\zeta = \frac{c}{\sqrt{km}}$; $\alpha = \frac{\varepsilon A}{2m\omega_n^2 d^3}$

Next, we write Equation (5.10) in state-space representation; hence we let $X_1 = \hat{x}$, and $X_2 = \dot{\hat{x}}$ to yeild :

$$\dot{X}_1 = X_2 \tag{5.11}$$

$$\dot{X}_2 = -X_1 - \hat{c}X_2 + \alpha \frac{[V_{DC} + V_{AC}\cos(\Omega\hat{t})]^2}{(1-\hat{x})^2} \tag{5.12}$$

For this second order system, we need to search for an appropriate set of intial conditions (η_1, η_2) that yeilds periodic solution for Equations (5.11) and (5.12). To proceed with the shooting technique, we define the follwing variables

$$X_3 = \frac{\partial \hat{x}}{\partial \eta_1},\ X_4 = \frac{\partial \hat{x}}{\partial \eta_2}\ ,\ X_5 = \frac{\partial \dot{\hat{x}}}{\partial \eta_1},\ X_6 = \frac{\partial \dot{\hat{x}}}{\partial \eta_2}$$

The shooting technique requires solving Equations (5.10) and (5.11) along with the below system of differntial equations, which are

$$\dot{X}_3 = X_5 \tag{5.13}$$

$$\dot{X}_4 = X_6 \tag{5.14}$$

$$\dot{X}_5 = -X_3 - \hat{c}X_5 + 2X_3\alpha \frac{[V_{DC} + V_{AC}\cos(\Omega\hat{t})]^2}{(1-X_1)^3} \tag{5.15}$$

$$\dot{X}_6 = -X_4 - \hat{c}X_6 + 2X_3\alpha \frac{[V_{DC} + V_{AC}\cos(\Omega\hat{t})]^2}{(1-X_1)^3} \tag{5.16}$$

The initial conditions for Equations (5.11 - 5.16) are

$$\begin{aligned} X_1(0) &= \eta_{10} \\ X_2(0) &= \eta_{20} \\ X_3(0) &= 1; \\ X_4(0) &= 0; \\ X_5(0) &= 0; \\ X_6(0) &= 1; \end{aligned} \tag{5.17}$$

where (η_{10}, η_{20}) are the intial guesses for the initial conditions, which lead to periodic motion. Then, we intergrate Equations (5.11 – 5.16) subjected to the intial conditions (5.17) over the duration of one period *T*. Subsequently, we calculate the values of $X_3 - X_6$ at time *T*, substitute them in the below algebric system of equations, and solve for the error in the intial conditions $(\partial\eta_1, \partial\eta_2)$.

$$\left\{\begin{pmatrix} X_3 & X_4 \\ X_5 & X_6 \end{pmatrix} - [I]\right\}\begin{Bmatrix} \partial\eta_1 \\ \partial\eta_2 \end{Bmatrix} = \begin{Bmatrix} \eta_{10} - x(T, \eta_{10}, \eta_{20}) \\ \eta_{20} - \dot{x}(T, \eta_{10}, \eta_{20}) \end{Bmatrix} \tag{5.18}$$

The procedue is repeated until the errors are minimized and a convergernce is achieved. The next step after obtaining the periodic motion is to analyze its stability. This can be done by solving for the eigenvalue of the manadromy matrix $\begin{pmatrix} X_3 & X_4 \\ X_5 & X_6 \end{pmatrix}$, which yeilds the two Floquete multiplieres. If the absoulte values of both Floquete multiplieres are less than unity then the perioidc motion is stable, otherwise it is considered unstable.

Figure 5.15 shows a verification of the shooting technique when compared with the time integration solution.

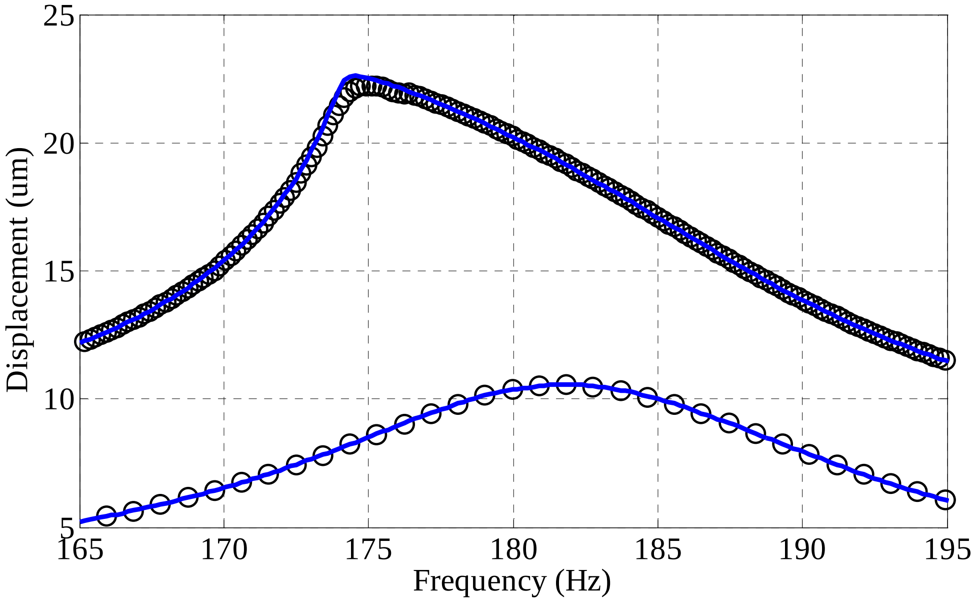

Figure 5.15: Frequency response for V_{DC} = *30 Volt*, V_{AC} = *40 Volt* and *0.58 g*. (solid blue - shooting technique, black circles - time integration)

5.3.1 Results

In Section 5.2, we concentrated on using the nonlinearities from the electrostatic forces to raise the sensitivity of the accelerometer. As we raise the electrostatic forces to very large values, we start to obtain a gap in the frequency response curve (Figure 5.16) at which the microstructure is expected to pull-in. This band of frequencies (gap) is also known as the inevitable escape band. Despite the disadvantages arising from the accelerometer undergoing pull-in, such as stiction and short-circuit problems, it comes to an advantage if the accelerometer is intended to be used as a switch triggered by acceleration, rather than a sensor. The shooting technique allowed us to further investigate the idea of obtaining a switch triggered by small acceleration.

5.3.1.1 Sensitive switch triggered by acceleration at primary resonance

We observed from Figures 5.7-5.14, obtained using the long-time integration method, how the accelerometer can be used also as a switch triggered by acceleration, however, with limited sensitivity. In this section we use a more accurate method, shooting method, to further investigate the capability of using the accelerometer as a sensitive switch triggered by acceleration by operating it at primary resonance ($\Omega \approx \omega_n$). Figure 5.16 represents the highest sensitivity obtained for a switch operating at primary resonance, showing sensitivity to accelerations as small as *0.02 g*. The working principle is as follows: if we operate the microstructure at a frequency of about *142 Hz*, the microstructure lies on the frequency response curve, giving a stable solution (Figure 5.17a). Once the microstructure experiences an acceleration of about *0.02 g*, the frequency response curve shifts to the left, and the microstructure suddenly is operating in the escape band and therefore pulls-in (switch on), as seen in Figure 5.17b.

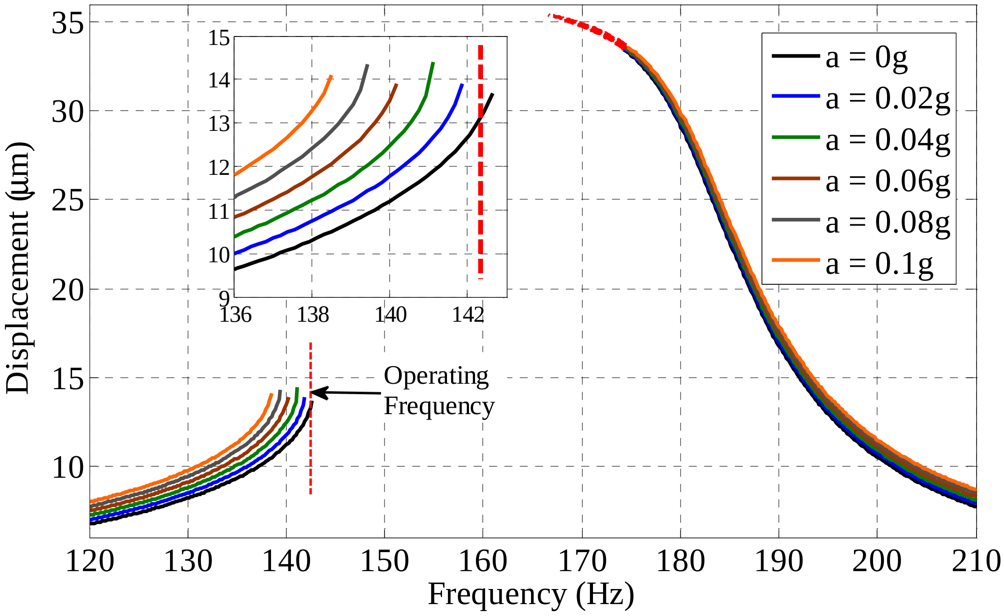

Figure 5.16: Frequency response curves for various accelerations in the case of primary resonance when V_{DC} = *60 Volt* and V_{AC} = *50 Volt*.

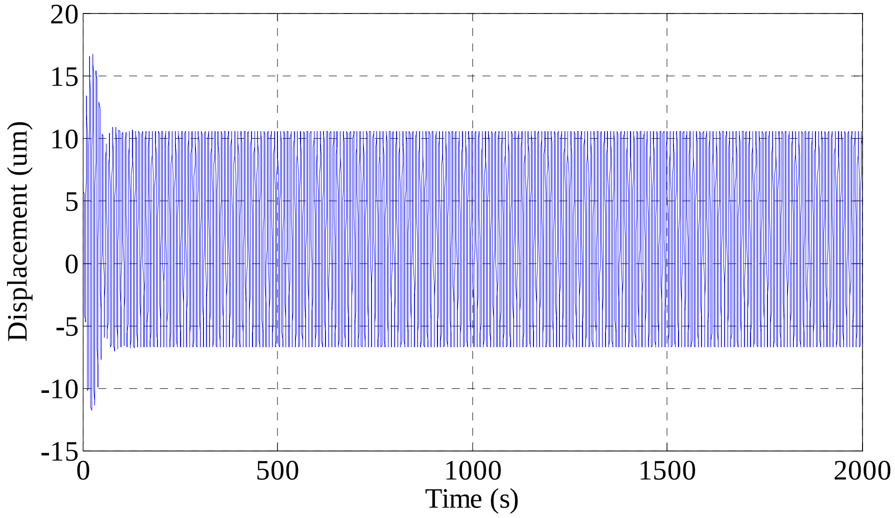

(a) At no applied acceleration.

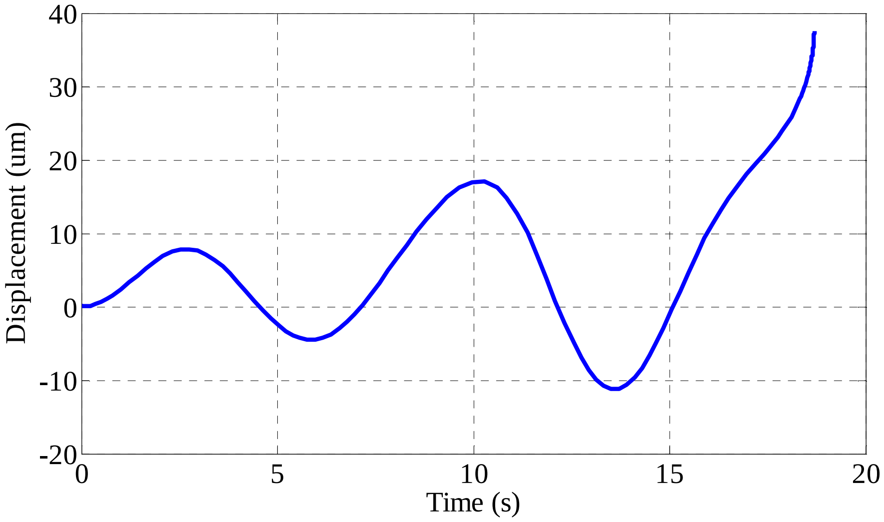

(b) Subjected to an acceleration of *0.02 g*.

Figure 5.17: The time history of the accelerometer response when excited by V_{DC} = *60 Volt*, V_{AC} = *50 Volt* and operating at a frequency Ω = *142 Hz*.

Operating the microstructure at such high voltages raises the important question of stability. It is crucial to understand how stable the microstructure is when operating very close to the escape band. To address this problem we calculate the domain of attraction (basin of attraction) of the periodic solution of the microstructure. The basin of attraction is a grid of initial conditions. For each set of initial conditions, we integrate the equation of motion and look at the stability of the solution. If the solution is stable, the set of initial conditions are represented as a white point on the phase plane. If the solution is unstable, the set of initial conditions are represented as a black point. Looking at Figure 5.18b, we find that no stable solution exits for the microstructure, which is expected as it is operating in the escape band. However, in Figure 5.18a, there is only a very small set of initial conditions at which the microstructure is stable. This raises concerns about the stability of the resonator and how reliable it is before detection of acceleration.

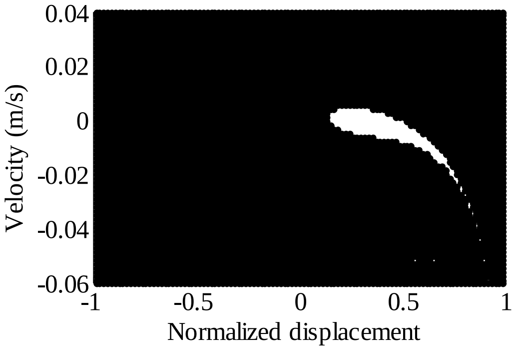

(a) At no applied acceleration

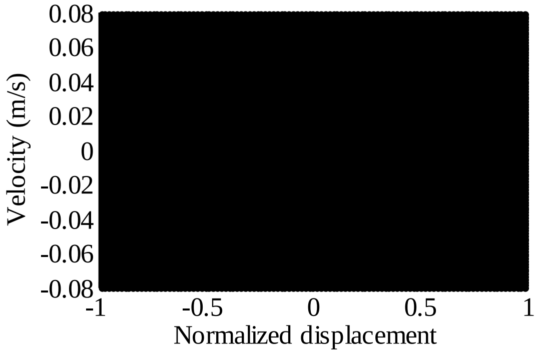

(b) Subjected to an acceleration of *0.02 g*.

Figure 5.18: Basin of attraction of the capacitive accelerometer excited by V_{DC} = *60 Volt*, V_{AC} = *50 Volt* and operating at a frequency Ω = *142 Hz* (safe basin - white, unsafe basin - black).

5.3.1.2 *Sensitive switch triggered by acceleration at sub-harmonic resonance*

Similar to the previous section, we investigate the capability of using the accelerometer as a sensitive switch triggered by acceleration but this time operating at sub-harmonic resonance ($\Omega \approx 2\omega_n$). Figure 5.19 represents the highest sensitivity obtained for a switch operating at sub-harmonic resonance, showing sensitivity to accelerations as small as *0.1 g*. We can note from Figure 5.19 that before applying the acceleration, the sub-harmonic resonance was inactivated. Applying the acceleration caused a sharp jump in the accelerometer response, which is very desirable for switching applications.

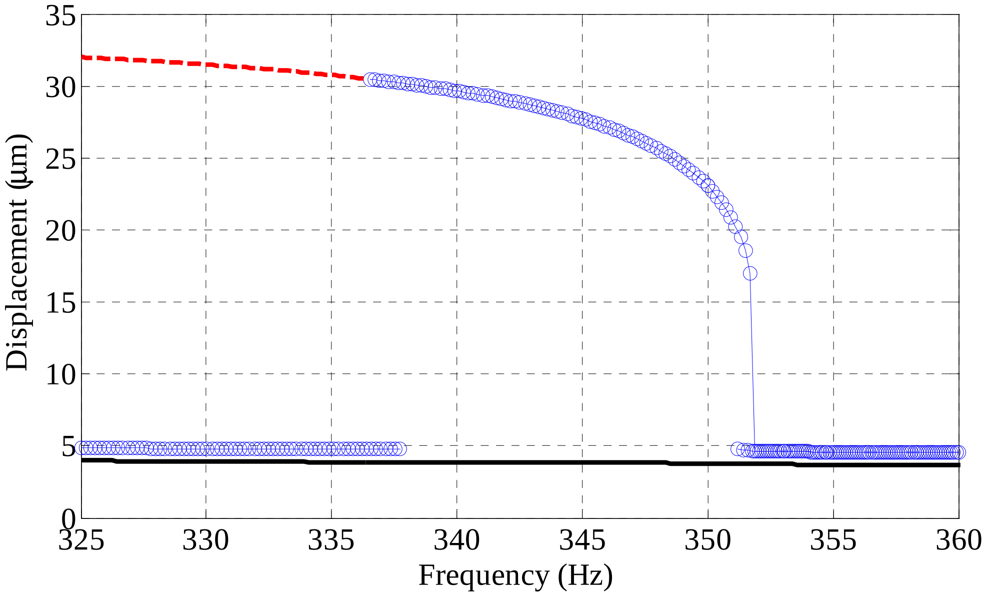

Figure 5.19: Frequency response curve for the case of sub-harmonic resonance when V_{DC} = *50 Volt*, and V_{AC} = *89 Volt.* (Solid black – *0 g*, circles - *0.1 g*, dashed red - unstable solution).

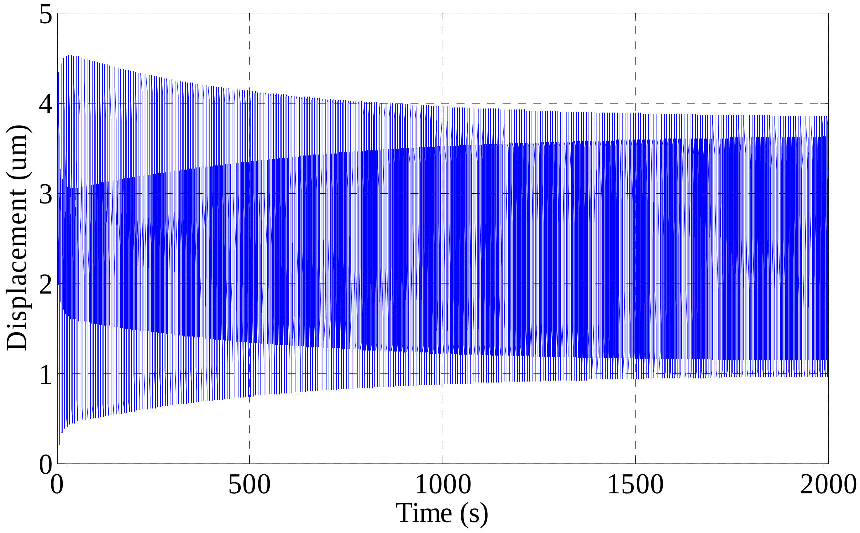

(a) At no applied acceleration.

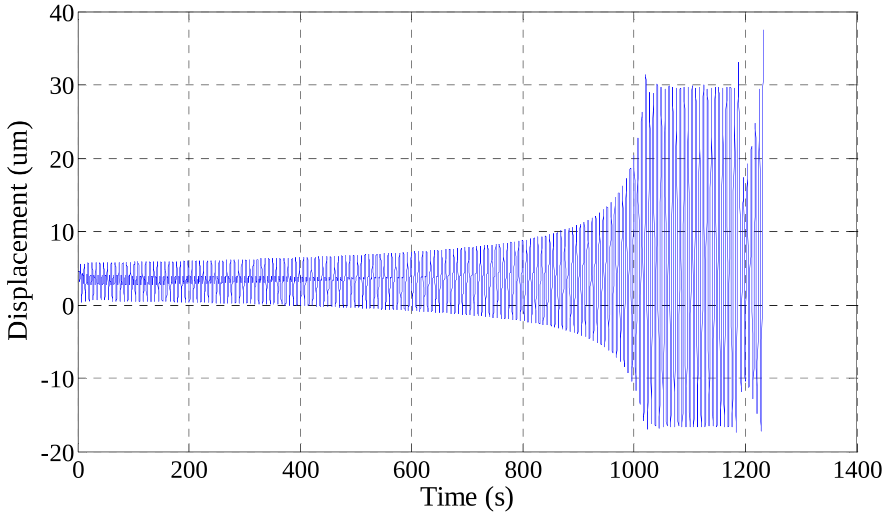

(b) Subjected to an acceleration of *0.1 g*.

Figure 5.20: The time history of the accelerometer response when excited by V_{DC} = *50 Volt*, V_{AC} = *89 Volt* and operating at a frequency Ω = *340 Hz*.

Similar to the previous section, once again, we calculate the basin of attraction of the periodic solution of the microstructure. Looking at Figure 5.21b, we find the same behavior observed for the primary resonance case. For Figure 5.21b, no stable solution exits for the microstructure, which is expected as it is operating in the escape band. In

Figure 5.21a, there is only a very small set of initial conditions at which the microstructure is stable.

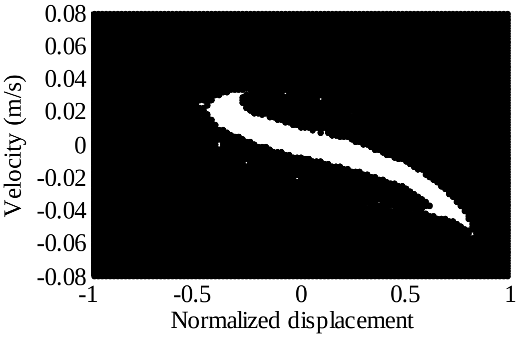

(b) At no applied acceleration.

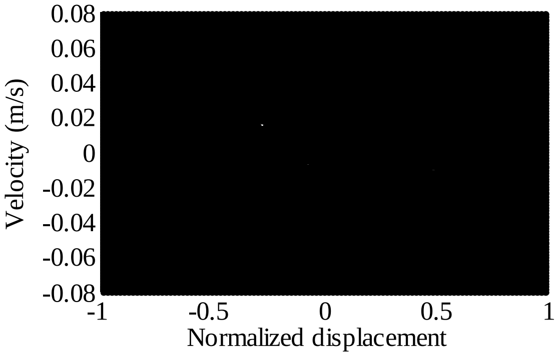

(b) Subjected to an acceleration of $0.1\ g$.

Figure 5.21: Basin of attraction of the capacitive accelerometer excited by $V_{DC} = 50$ Volt, $V_{AC} = 89$ Volt and operating at a frequency $\Omega = 340$ Hz (safe basin - white, unsafe basin - black).

In conclusion, for the given microstructure, using the electrostatic forces to obtain a sensitive switch triggered by acceleration is an attractive concept; however, it requires high power and raises instability issues. One way of enhancing the stability of the microstructure before undergoing acceleration is using control methods; however, it is beyond the scope of this thesis.

Chapter 6. Reliability of Resonant Sensors under Mechanical Shock, Driven by DC and AC Load

In this chapter we investigate the effects of mechanical shock on the response of a resonant sensor. Resonant sensors typically operate at low pressures for enhanced sensitivity, which makes their response to external disturbances such as shock a major issue. The simulation results are demonstrated in a series of shock spectra that help indicate the combined effects of shock and the existing nonlinearities from the electrostatic forces. The effect of the shock duration coinciding with the AC harmonic load frequency is also investigated. It is found that for specific shock and AC excitation conditions, the resonator might experience an early dynamic instability. This may lead to unexpected failure of the resonator. The theoretical and experimental works of this chapter are based on sample *c* of the capacitive device in Chapter 3.

6.1 Problem Formulation

A typical parallel-plate electrostatically driven resonator can be represented by the SDOF model shown in Figure 5.1 in Chapter 5. The equation of motion is given by Equation (6.1). Here, the acceleration term is represented as a base excitation $m\ddot{y}(t)$, where $\ddot{y}(t)$ is the half-sine pulse as defined in Chapter 2.

$$m\ddot{z} + c\dot{z} + kz = \frac{\varepsilon A(V_{dc} + V_{ac} Cos\Omega t)^2}{2(d-z)^2} - m\ddot{y}(t) \qquad (6.1)$$

Next, we use long time integration of Equation (6.1) to obtain the microstructure response.

6.2 Defining Shock Spectrum due to AC Load

Studying the nonlinear effects of the AC harmonic load on the shock spectrum can be challenging, due to the oscillatory motion of the resonator. The proof mass of the resonator oscillates away and towards the substrate, and the time at which the mechanical shock is applied can either attenuate the microstructure response or amplify it. In some cases, amplifying the response of the resonator can lead to pull-in. Figure 6.1 gives an example of the simulated response of the resonator to the combination of electrostatic forces and shock, showing the shock applied at two different times. For Figure 6.1a, the shock amplifies the resonator response up to about *25* μm. For Figure 6.1b, with the shock being applied just *2.3 ms* later, the shock attenuates the response of the resonator to about *4* μm before it goes back to the level of vibrations before shock.

Figure 6.1 indicates how critical it is to account for the time at which the shock is applied to the resonator. In order to account for this effect, for a given value of shock duration T, the shock is applied at various time instances (T_{AP}) during one full steady-state oscillation of the resonator. In other words, if the resonator oscillating period is T_{AC}, the shock is applied at various fractions of T_{AC}. For each time instance of the applied shock, the maximum displacement of the resonator is calculated. To capture the worst case scenario of the response, the maximum displacement is calculated by comparing the results of all time instances. Figure 6.2 shows a plot of the resonator maximum response to an applied shock of *1 g*, applied at different times of two full cycles of oscillations of the resonator. In Figure 6.2, the normalized time scale is the time instance of shock application T_{AP} normalized by the resonator response time T_{AC}.

The final step in obtaining the shock spectrum is to repeat the same procedure and obtain data similar to Figure 6.2 for each shock duration. From this figure, one data point is obtained to be used in the shock spectrum. Figure 6.3 shows an example of a shock spectrum of the resonator due to shock, DC load, and an AC load for the case when the resonator is excited at resonance.

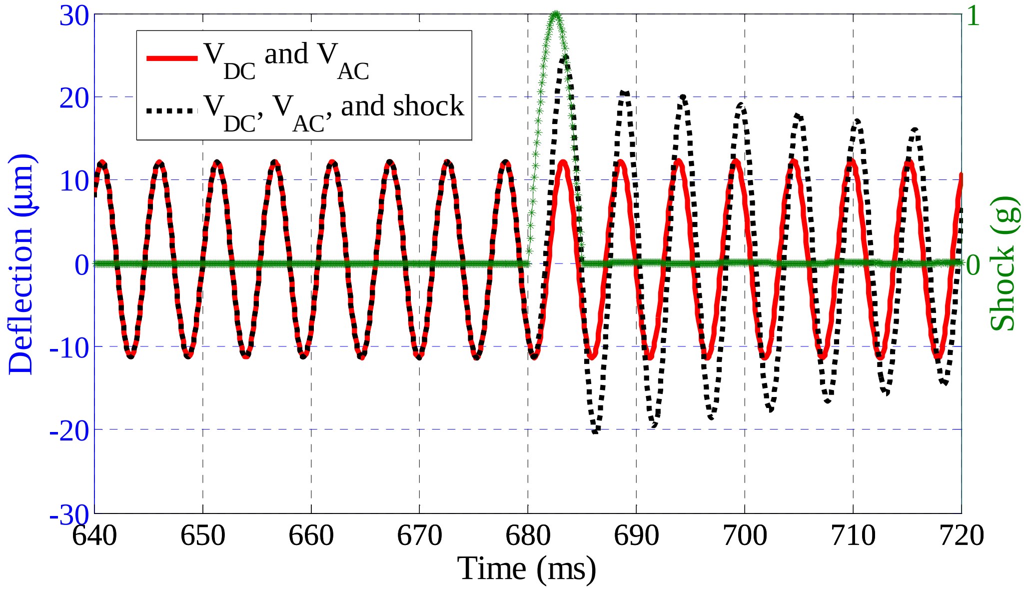

(a) Mechanical shock applied at time equals *680 ms.*

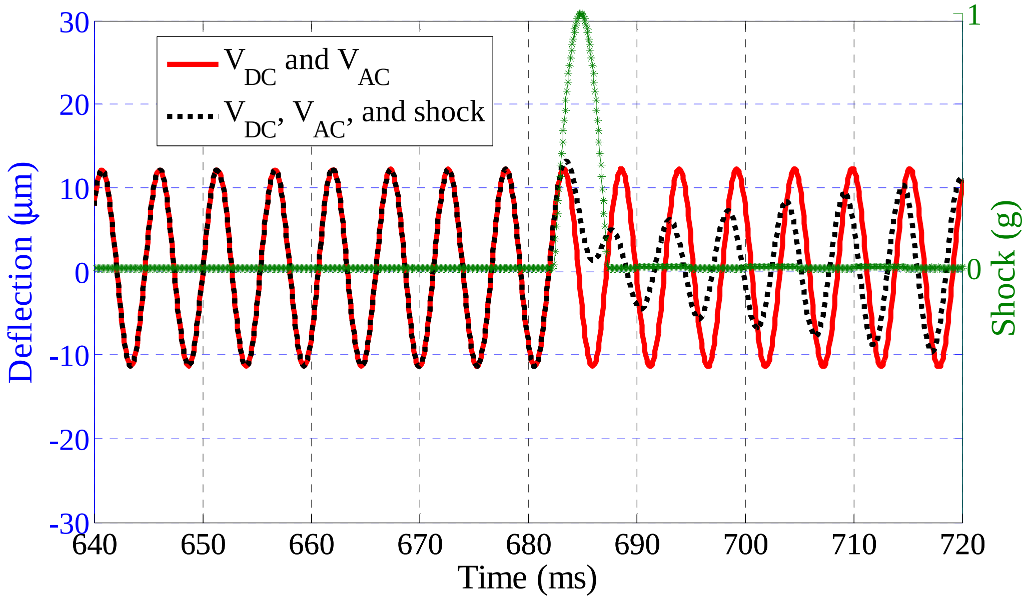

(b) Mechanical shock applied at time equals *682.3 ms*.

Figure 6.1: Time history response of sample *c* of the resonator at $V_{DC} = 30$ Volt, $V_{AC} = 15$ Volt, $T = 5$ ms, a shock of *1 g*, and operating at a frequency $\Omega = \omega_n$. The damping ratio is assumed $\zeta = 0.006$.

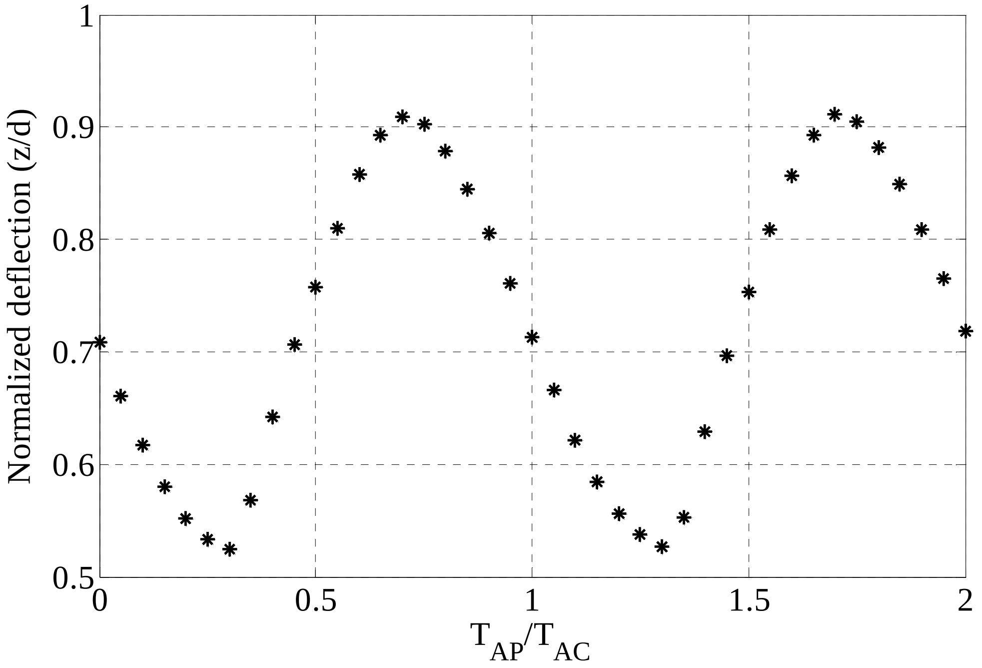

Figure 6.2: Maximum response of sample *c* of the resonator to an applied shock of *1 g* and $T = 5$ ms, applied at various times during two oscillations of the resonator, where $V_{DC} = 30$ Volt, $V_{AC} = 15$ Volt and operating at a frequency $\Omega = \omega_n$. The damping ratio is assumed $\zeta = 0.006$.

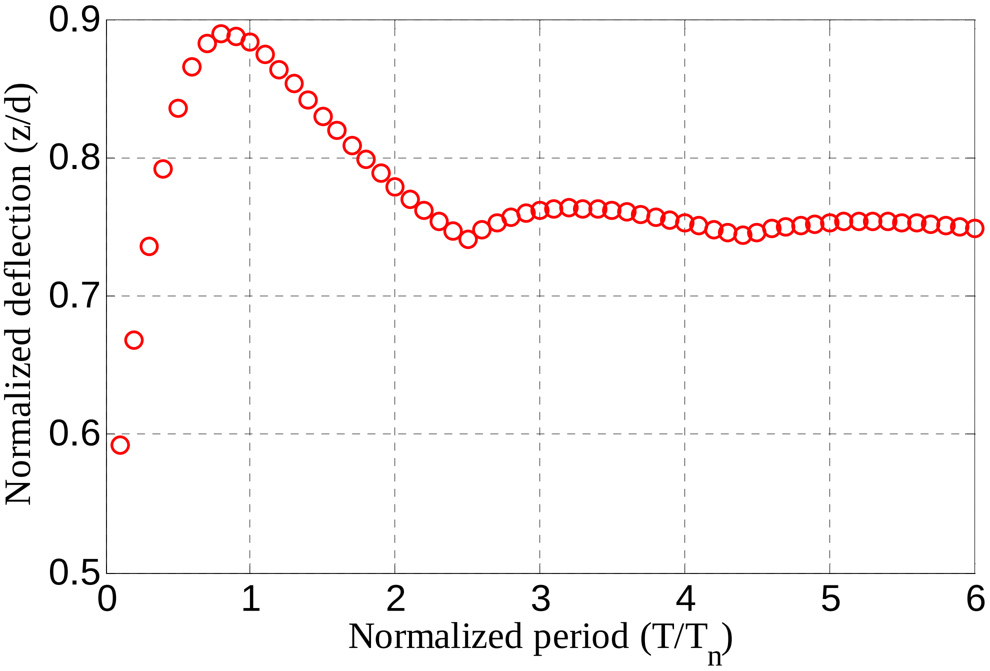

Figure 6.3: Nonlinear shock spectrum of sample *c* of the resonator at an applied shock of *1 g*, where $V_{DC} = 30$ *Volt*, $V_{AC} = 15$ *Volt* and operating at a frequency $\Omega = \omega_n$. The damping ratio is assumed $\zeta = 0.006$.

6.3 Simulation Results

In order to fully understand the behavior of resonators under mechanical shock, various simulations are conducted to study the effect of the different parameters of this problem. The parameters are the shock amplitude A_0, shock duration T, DC voltage amplitude V_{DC}, AC harmonic load amplitude V_{AC}, and harmonic load frequency Ω. The results are represented in a series of shock spectra, where the response of the resonator is normalized by the gap width d. For all the simulations conducted, we use the parameters of the capacitive accelerometer introduced in Chapter 3. We assume the resonator to have a linear damping ratio of $\zeta = \frac{c}{2m\omega_n} = 0.006$. This value of low linear damping ratio is typical for a resonator operating at reduced pressure.

6.3.1 Effect of the AC harmonic load on the shock spectrum

In this section we investigate the effect of the AC harmonic load on the shock spectrum of the resonator. Figures 6.4 and 6.5 depict the nonlinear spectrum of the resonator subjected to a shock load of *1 g*, operating at a frequency $\Omega = \omega_n$, and actuated by a V_{DC} of *20 Volt*, and *30 Volt*; respectively. For the purpose of making a valuable qualitative comparison between the different applied AC harmonic loads, the maximum response of the resonator due to the DC and AC harmonic loads alone is subtracted from the total response. The figures show that the AC harmonic load has a softening effect on the resonator. As we raise V_{AC}, the response of the resonator increases and we begin to obtain pull-in zones in the shock spectrum. As we raise the DC voltage, lower V_{AC} is needed to cause the resonator to pull-in. This clearly shows that accounting for the effects of the AC harmonic load and the DC voltage when testing the reliability of the resonator under mechanical shock is crucial. It is important to note that at no applied shock, the resonator has a response due to the AC harmonic load. Figure 6.6 shows shock spectrums of the resonator for a shock load of *1 g* and a combined DC and AC voltage of *40 Volt*. Different combinations of the DC and AC loads are used to better demonstrate the effect of the AC harmonic load. For this particular figure, the spectrums show the total response of the resonator, without subtracting the effect of the AC harmonic load alone. The figure shows that the combination of the DC and AC loads has a more severe softening effect on the resonator, making it more sensitive to the applied shock. In the case of actuating the resonator by either the DC load alone, or the AC harmonic load alone, the response of the resonator to shock is less sensitive.

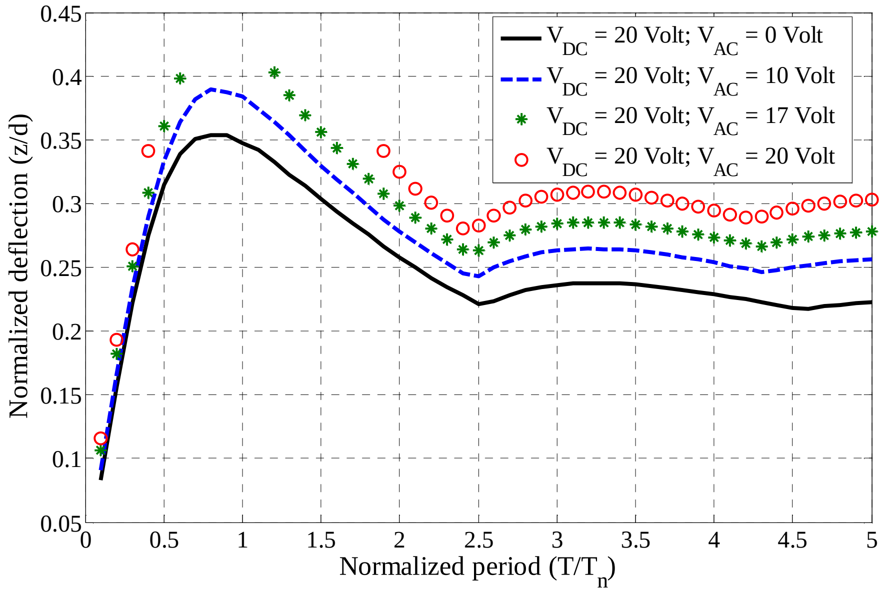

Figure 6.4: Nonlinear shock spectrum of the resonator for various V_{AC} at an applied shock of $1\ g$, where $V_{DC} = 20$ and operating at a frequency $\Omega = \omega_n$. The damping ratio is assumed $\zeta = 0.006$.

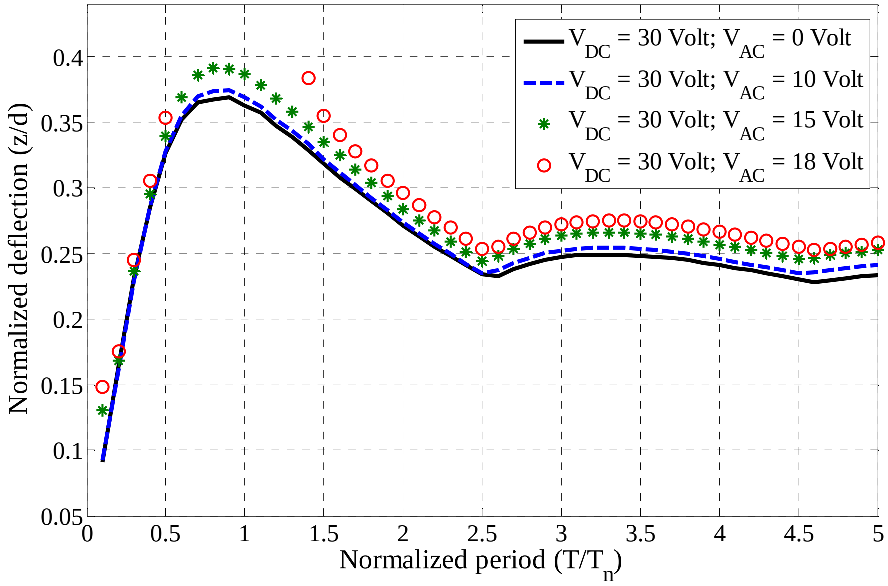

Figure 6.5: Nonlinear shock spectrum of the resonator for various V_{AC} at an applied shock of $1\ g$, where $V_{DC} = 20$ Volt and operating at a frequency $\Omega = \omega_n$. The damping ratio is assumed $\zeta = 0.006$.

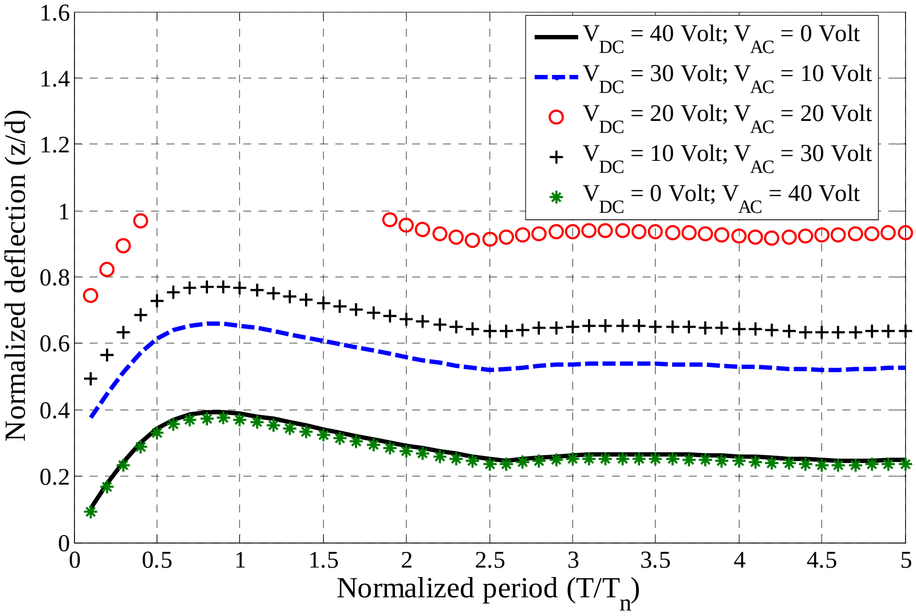

Figure 6.6: Nonlinear shock spectrum of the resonator for a combined V_{AC} and V_{DC} of *40 Volt* at an applied shock of *1 g*, operating at a frequency $\Omega = \omega_n$. The damping ratio is assumed $\zeta = 0.006$.

6.3.2 Effect of the AC operating frequency on the shock spectrum

In this section we investigate the effect of the AC operating frequency Ω on the shock spectrum of the resonator. Figure 6.7 depicts the nonlinear spectrum of the resonator subjected to a shock load of *1 g*, actuated by a V_{DC} of *20 Volt* and V_{AC} of *15 Volt*. If the resonator is operated at a frequency near its natural frequency ω_n, the response of the resonator is amplified and for a range of shock durations may experience pull-in. For an operating frequency below ($0.2\ \omega_n$) or beyond ($1.5\ \omega_n$) the natural frequency of the resonator, the response of the resonator to shock is almost the same as the linear case, where no electrostatic forces are present.

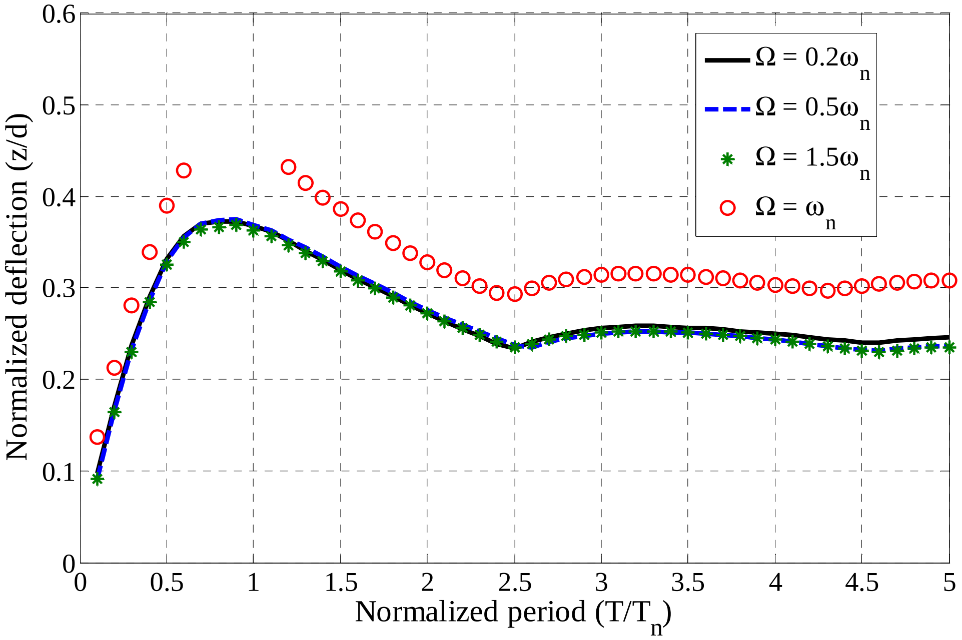

Figure 6.7: Nonlinear shock spectrum of the resonator for various AC frequencies (Ω) at an applied shock of $1\ g$, where $V_{DC} = 20$ Volt and $V_{AC} = 15$ Volt. The damping ratio is assumed $\zeta = 0.006$.

6.4 Experimental Results and Comparison with Simulations

The previous section showed the importance of accounting for the combined effects of mechanical shock, DC load, and the AC harmonic load on a resonator. The simulations showed that for certain conditions, the mechanical shock could either amplify or attenuate the response of the resonator. In some cases, the amplification of the resonator response causes it to reach an early dynamic instability (pull-in). An experimental investigation is conducted to further investigate and validate the theoretical predictions. The same experimental setup of Figure 3.9 of Chapter 3 is used for the experimental investigation of mechanical shock applied to a resonator. The device was mounted on a shaker head, and connected to a V_{DC} and V_{AC} supply in a small electrical circuit. Current limiting resistors were used in the circuit to avoid failure of the device in the case of pull-in. An analog function generator was used to generate the AC harmonic load. A reference accelerometer was also mounted on the shaker head to monitor the value of shock applied to the device. A laser vibrometer was used to monitor the response of the device proof mass. The shaker (Figure 3.10b) was placed inside the vacuum chamber.

It is important to mention that it is extremely difficult to compare simulation and experimental results as was done in the previous chapters using the shock spectrum. This is because there is no way to explicitly control the instant of shock application during the experiment. It is also hard to hit the resonant frequency of the resonator using the analog function generator. In the presence of such difficulties, the most efficient way of comparison is by imitating the experimental conditions and comparing qualitatively the response of the resonator. Parameters such as the operating pressure, the AC frequency Ω, and most importantly the instant of shock application T_{AP} were applied to the simulation model. The experimental input shock pulse shape was imported directly from the experiment and applied to the simulation model. The parameter T_{AP} was approximated by carefully looking at the time history of the resonator response and the input shock. Three different cases were compared both theoretically and experimentally, where the resonator response was amplified, attenuated, or reached pull-in.

6.4.1 Amplification of the resonator response

In this case, the resonator was actuated with a $V_{DC} = 24.3$ *Volt*, $V_{AC} = 18.92$ *Volt*, and $\Omega = 189$ *Hz*. The resonator was operated at reduced pressure of *180 mtorr*. Figure 6.8b shows the theoretical results and Figure 6.8c shows the experimental results for the studied case.

The results show that at a given shock of *1 g*, the resonator response was amplified. The simulation and experimental results are in good agreement as observed from the figures.

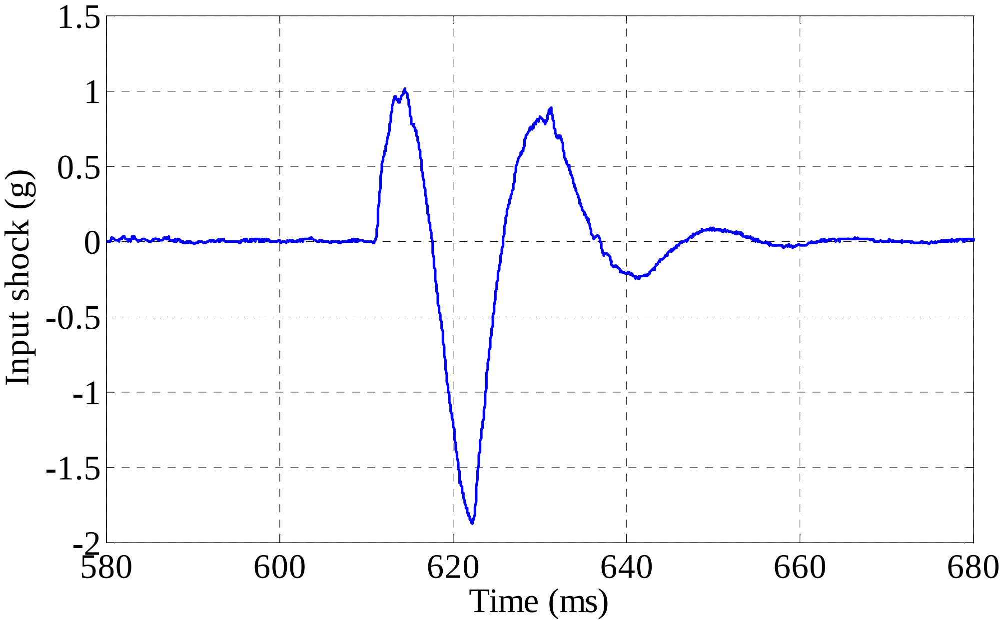

(a) Experimental input shock of *1 g* at a total shock duration of *T = 20 ms*.

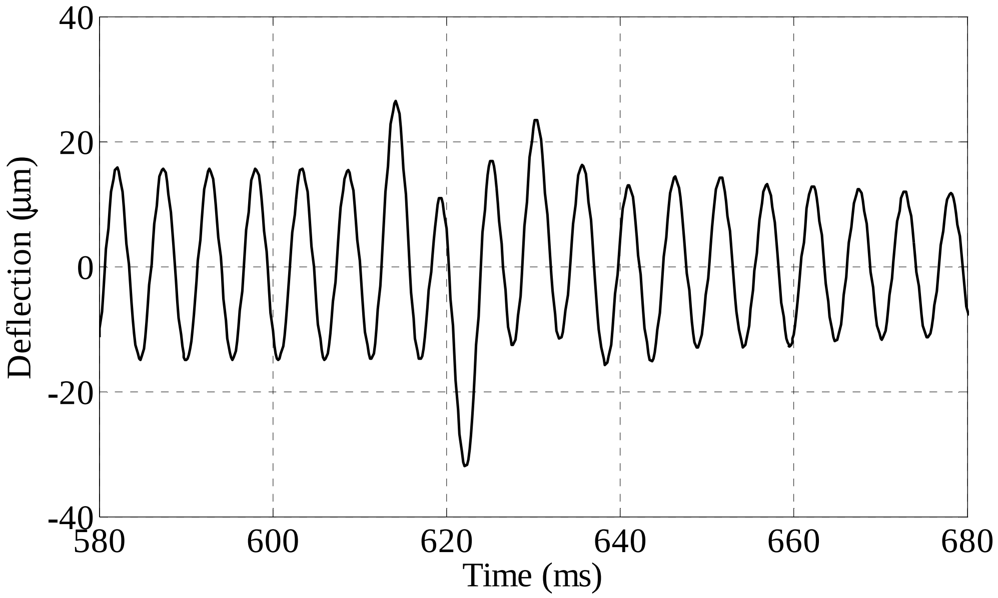

(b) Simulated time history response of the resonator.

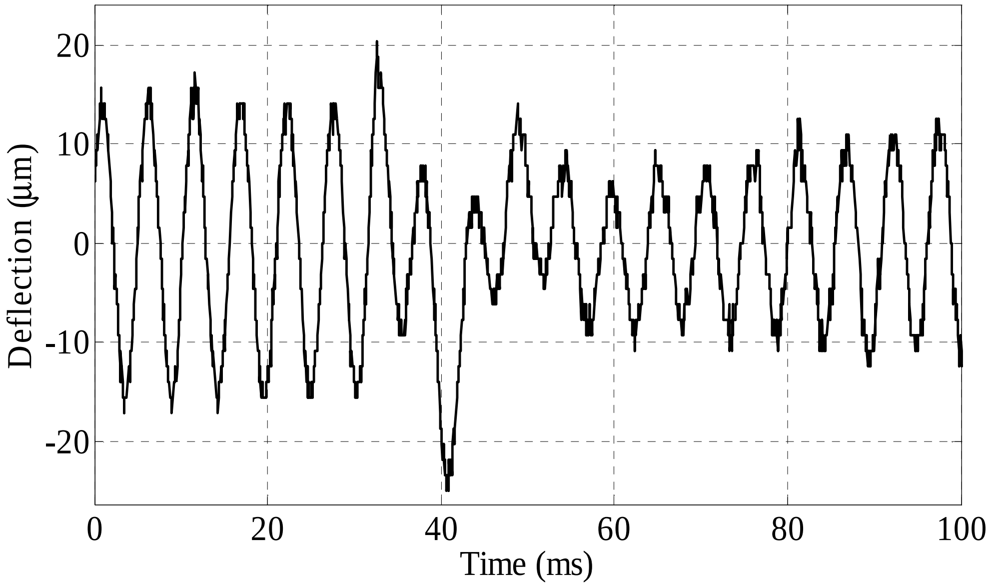

(c) Experimental time history response of the resonator.

Figure 6.8: Theoretical and experimental results of the resonator when actuated with V_{DC} = *24.3 Volt*, V_{AC} = *18.92 Volt*, and *Ω = 189 Hz*. The operating pressure is equal *180 mtorr*.

6.4.2 Attenuation of the resonator response

In this case, the resonator was actuated with a V_{DC} = *25 Volt*, V_{AC} = *17.96 Volt*, and *Ω = 188 Hz*. The resonator was operated at reduced pressure of *200 mtorr*. Figure 6.9b shows the theoretical results and Figure 6.9c shows the experimental results for the studied case. The results show that at a given shock of *1 g*, the resonator response was attenuated. The simulation and experimental results are in good agreement as observed from the figures.

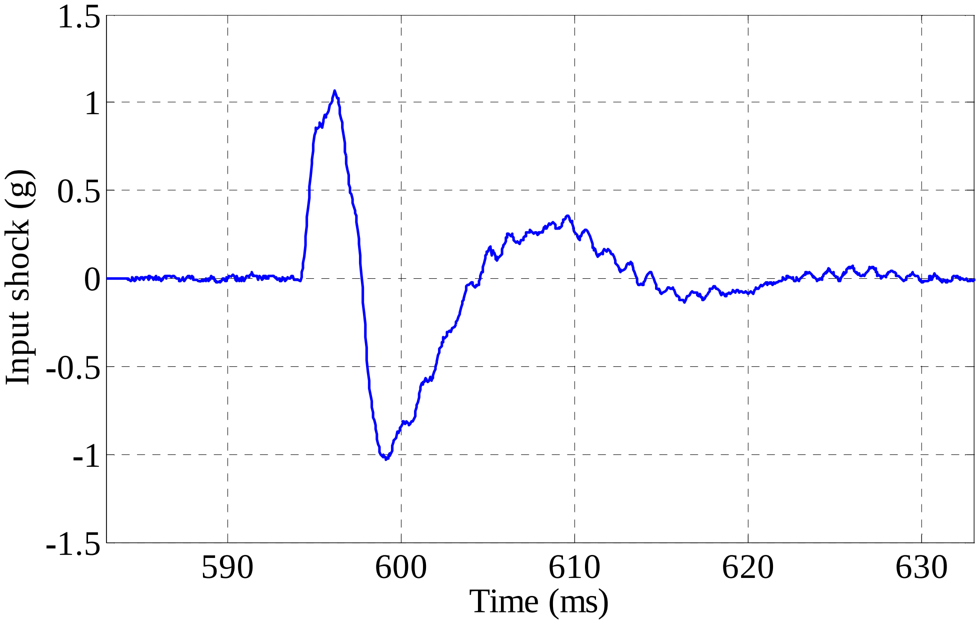

(a) Experimental input shock of *1 g* at a total shock duration *T = 10 ms*.

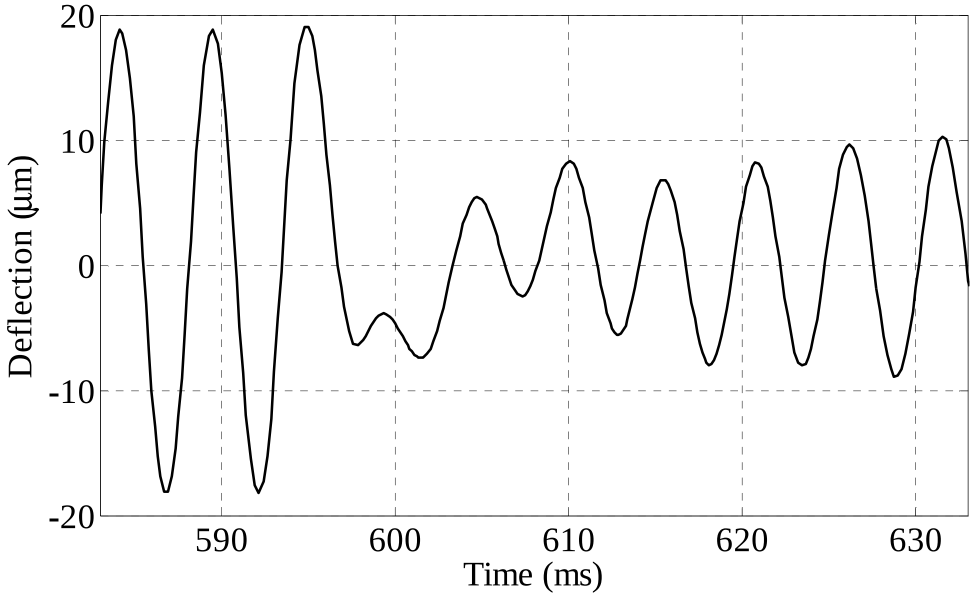

(b) Simulated time history response of the resonator.

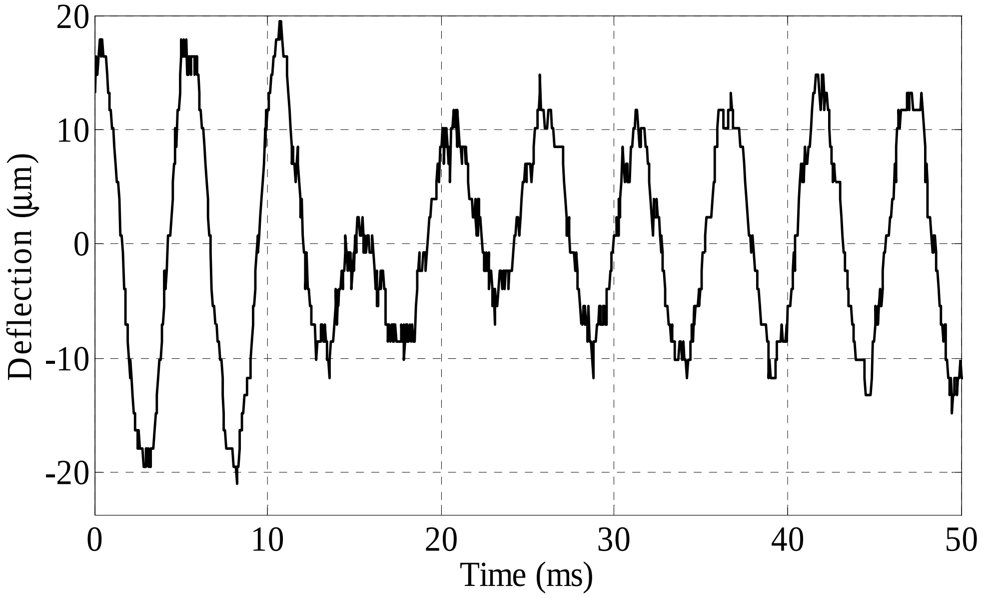

(c) Experimental time history response of the resonator.

Figure 6.9: Theoretical and experimental results of the resonator when actuated with V_{DC} = *25 Volt*, V_{AC} = *17.96 Volt*, and Ω = *188 Hz*. The operating pressure is equal *200 mtorr*.

6.4.3 Resonator pull-in

In this case, the resonator was actuated with a V_{DC} = *19.2 Volt*, V_{AC} = *17.96 Volt*, and Ω = *187 Hz*. Figure 6.10b shows the theoretical results and Figure 6.10c shows the experimental results for the studied case. The results show that at a given shock of *1 g*, the resonator reached an early dynamic instability and pulled-in. The simulation and experimental results are in good agreement as observed from the figures.

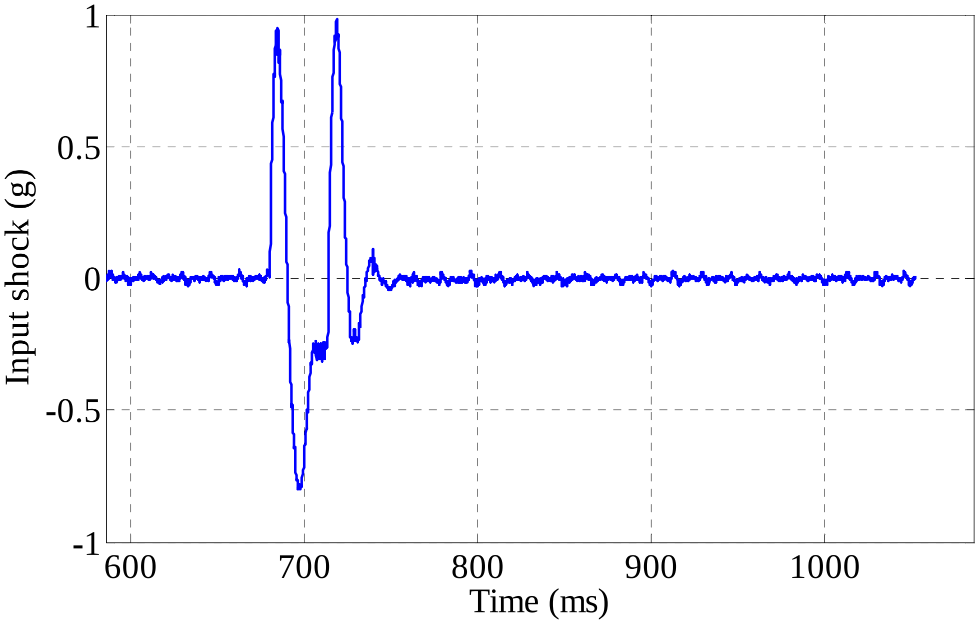

(a) Experimental input shock of *1 g* at a total shock duration *T = 45 ms*.

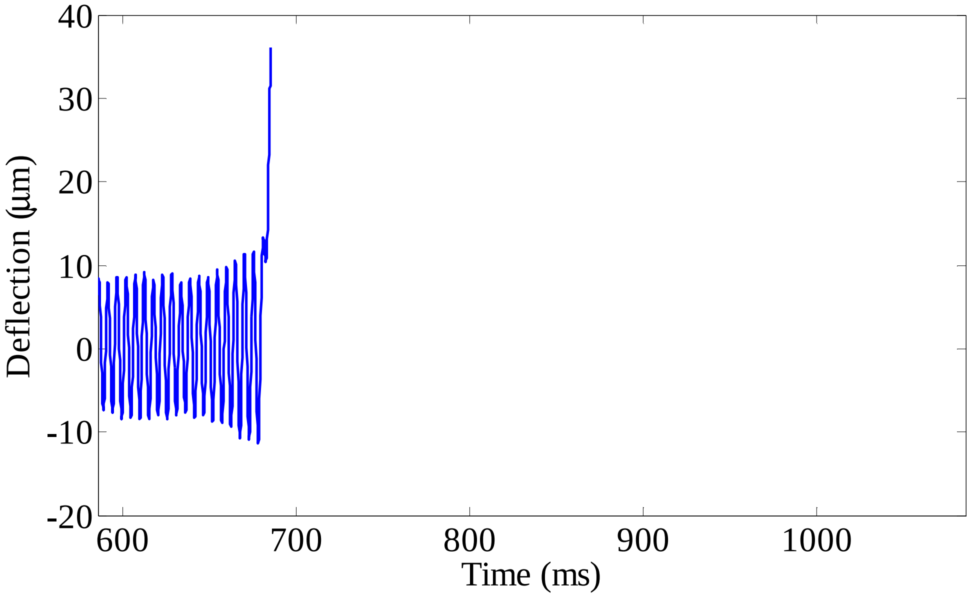

(b) Simulated time history response of the resonator.

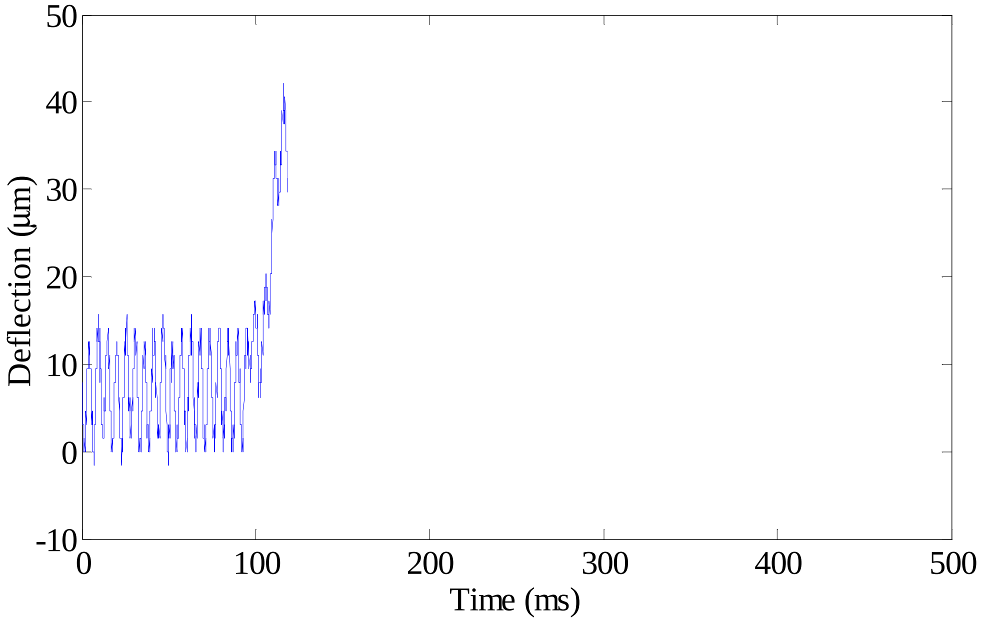

(c) Experimental time history response of the resonator.

Figure 6.10: Theoretical and experimental results of the resonator when actuated with $V_{DC} = 19.2$ *Volt*, $V_{AC} = 21.2$ *Volt*, and $\Omega = 187$ *Hz*. The operating pressure is equal *200 mtorr*.

Chapter 7. Summary, Conclusions, and Future Works

7.1 Summary and Conclusions

We presented an investigation of the response of a MEMS device under mechanical shock and electrostatic force. We observed interesting behaviors for the case of negligible squeeze film damping effect, where an apparent gap in the spectrum, referred to as the pull-in zone, was obtained. Raising the electrostatic force caused softening of the microstructure and created wider pull-in zones. When squeeze film effects were present, a great suppression of the proof mass deflection in the dynamic region of the spectrum was noted, causing pull-in to occur at the quasi-static region, where SQFD has minimal effect. This is crucial for MEMS designers that design devices acting in the quasi-static range to avoid any amplification in the motion of the microstructure.

The effect of the PCB motion on the response of a MEMS device to shock was also investigated. It was found that in the case where the natural frequency of the PCB is close to that of the MEMS device, the PCB amplifies the response of the MEMS device due to shock. However, in the case where the natural frequency of the PCB was far from that of the MEMS device, the PCB motion had no effect on the response of the MEMS device to shock and acted almost as a rigid body.

Also presented was the effect of mechanical shock on an electrostatically driven resonator. It was found that the time at which the mechanical shock is applied to the resonator is of great importance. In some cases, the response of the resonator was attenuated due to the applied shock. In other cases, the response of the resonator was amplified, sometimes reaching pull-in which could lead to its failure.

The use of nonlinearities arising from the electrostatic forces was used to an advantage, in an attempt to enhance the sensitivity of a resonant accelerometer. It was found that at high values of electrostatic actuation, the accelerometer becomes softer and is more sensitive to low accelerations. One draw back to this concept is the stability of the accelerometer at such high electrostatic forces. The basin of attraction was used to illustrate the stability of the accelerometer, and it was found that for high electrostatic forces, the accelerometer was almost unstable. This fact was used to an advantage in realizing a switch triggered by low accelerations.

The experimental investigation presented in this work was first used to obtain tested device parameters. Experimental investigations were conducted to validate the simulations. The experimental data obtained on the device response to shock under different actuation voltages was in good agreement with the simulations, with and without the presence of squeeze film damping. The experimental data on the response of the resonator to mechanical shock was also in good agreement with the simulation results.

It is realized through the work conducted in this thesis, that accounting for the electrostatic forces, squeeze film damping, and PCB motion when investigating the response of a MEMS device under shock is vital. It is found in many cases, that the response of a MEMS device is liable to amplifications that may lead to early dynamic instabilities, and hence could lead to its failure.

7.2 Future Works

The following is a list of recommendations and notes for future work.

- The use of control methods to stabilize the resonant accelerometer when operated in the nonlinear regime.
- The design of a microstructure for the purpose of acting as a switch triggered by acceleration, using the same concept adopted in this thesis. The design should include optimization of the mechanical parameters such as the stiffness, damping, and the natural frequency, along with the geometric properties of the device such as the electrode surface area and gap size.
- Further study the fractal behavior of pull-in when the microstructure is electrostatically actuated and subjected to mechanical shock.
- Improve the experimental setup used to investigate the effect of mechanical shock on resonators by better controlling the input parameters and the instant of shock application for a more accurate comparison with simulations.

- Avoid current magnetic problems existing from the shaker used in vacuum by the use of a magnetic insulating material between the driving shaft of the shaker and the microstructure placed on it.
- The use of a new shaker when conducting the experimental work in vacuum that does not have magnetic effects on the microstructure for more accurate results.
- Modify the resonant accelerometer problem from measuring only static acceleration to measuring accelerations from random vibration signals.
- Perform experimental work to verify the concepts used in enhancing the sensitivity of a resonant accelerometer.
- Investigate the effect of the position of the microstructure on the PCB, when the assembly is subjected to mechanical shock.
- Investigate the effect of mechanical shock on resonant sensors when placed on a PCB.
- Conduct similar theoretical and experimental investigations on a real MEMS device with geometry in the micro-range, rather than the capacitive sensor used in this thesis.

References

1. Abdel-Rahman, E. M., Younis, M. I., and Nayfeh, A. H., [2002], *“Characterization of the mechanical behavior of an electrically actuated microbeam,”* Journal of Micromechanics and Microengineering. **12**(6), pp. 759-766.
2. Abdel-Rahman, E. M., and Nayfeh, A. H., [2003], *“Secondary resonances of electrically actuated resonant microsensors,”* Journal of Micromechanics and Microengineering, **13**(3), pp. 491-501.
3. Agrawal, M., Chandorkar, S. A., Candler, R. N., Kim, B., Hopcroft, M. A., Melamud, R., Jha, C. M., Kenny, T. W., and Murmann, B., [2006], *“Optimal drive condition for nonlinearity reduction in electrostatic microresonators,”* Journal of Applied Physics Letters, **89**.
4. Agrawal, M., Mehta, H., Candler, R. N., Chandorkar, S. A., Kim, B., Hopcroft, M. A., Melamud, R., Bahl, G., Kenny, T. W., and Murmann, B., [2007], *“Scaling of amplitude-frequency-dependency nonlinearities in electrostatically transduced microresonators,”* Journal of Applied Physics, **102**.
5. Aikele, M., and Bauer, K., [2001], *“Resonant accelerometer with self-test,”* Sensors and Actuators A, **92**, pp.161-167.
6. Alsaleem, F. M., [2007], *“An Investigation into the Effect of PCB Motion on the Dynamic Response of MEMS Devices Under Mechanical Shock,”* Master’s Thesis, State University of New York at Binghamton, Mechanical Engineering Department.
7. Alsaleem, F. M., Younis, M. I., and Miles, R., [2008], *“An investigation into the effect of the PCB motion on the dynamic response of MEMS devices under mechanical shock,”* Journal of Electronic Packaging, **130**.

8. Alsaleem, F. M., Younis, M.I., and Ibrahim, M. I., [2009], *"An Investigation into the effect of the PCB motion on the dynamic response of MEMS devices under mechanical shock loads,"* J. Microelectromech. Syst., Accepted.
9. Andrews, M., Harris, I., and Turner, G., [1993], *"A comparison of squeeze-film theory with measurements on a microstructure,"* Sensors and Actuators A, **36**, pp. 79-87.
10. Ayela, F., and Fournier, T., [1998], *"An experimental study of anharmonic micromachined silicon resonators,"* Measurement Science and Technology, **9**(11), pp. 1821-1830.
11. Bart S., Zhang, S., Rabinovich V., Cunningham S., [1999], "*Coupled Package-Device Modeling for MEMS,"* Proc. MSM **99**, San Juan, Puerto Rico, USA.
12. Blech, J. J., [1983], *"On isothermal squeeze films,"* Journal of Lubricants Technology, **105**, pp. 615-620.
13. Brown, T. G., Davis, B., Hepner, D., Faust. J., Myers. C.., Muller. P., Harkins, T., Hollis, M., Miller C., and Placzankis B., [2001], *"Strap-down microelectromechanical (MEMS) sensors for high-g munition applications,"* IEEE Trans. Magnetics **37**, pp. 336-342.
14. Brown T. [2003], *"Harsh military environments and microelectromechanical (MEMS) devices,"* Proc. of IEEE Sensors **2**, pp. 753-760.
15. Burns, D. W., and Horning, R. D., [1995], *"Resonant microbeam accelerometers,"* Proceedings of the International Solid-State Sensors and Actuators Conference - TRANSDUCERS '95, **2**, pp. 659-662.
16. Burrer, C., and Esteve, J., [1994], *"A novel resonant silicon accelerometer in bulk-micromachining technology,"* Sensors and Actuators A, pp. 185-189.
17. Chu, P. B., Nelson, P. R., Tachiki, M. L., and Pister, K. S. J., [1996], *"Dynamics of polysilicon parallel-plate electrostatic actuators,"* Sensors and Actuators A, **52**, pp. 216-220.

18. Darling, R. B., Hivick, C., and Xu, J., [1998], *"Compact analytical modeling of squeeze film damping with arbitrary venting conditions using a Green's function approach,"* Sensors and Actuators A, **70**, pp. 32-41.

19. De Coster J., Tilmans H., Van Beek J., Rijks G., and Puers R., [2004], "*The Influence of Mechanical Shock on the Operation of Electrostatically Driven RF-MEMS Switches,"* J. Micromech. Microeng, **14** (9) ,pp- S49-S54.

20. De, S. K., and Aluru, N. R., [2006], *"Complex nonlinear oscillations in electrostatically actuated microstructures,"* Journal of Microelectromechanical Systems, **15**(2), pp. 355-369.

21. Fan M. S., and Shaw H. C., [2001], "*Dynamic Response Assessment for the MEMS Accelerometer Under Severe Shock Loads,*" National Aeronautics and Space Administration NASA, Washington, DC TP—2001–209978, Washington, DC.

22. Gui, C., Legtenberg, R., Tilmans, H. A. C., Fluitman, J. H. J., and Elwenspoek, M., [1998], *"Nonlinearity and hysteresis of resonant strain gauges,"* Journal of Microelectromechanical systems, **7**(1), pp. 122-127.

23. Hartzell, A. and Woodilla D., [1999], *"Reliability methodology for prediction of micromachined accelerometer stiction,"* Proc. IEEE Int. Reliability Physics Symp., pp. 202-205

24. Helsel, M., and Gassner, G., [1994], "*Navigation grade micro-machined silicon accelerometer,"* Proceedings of the 1994 IEEE Position Location and Navigation Symposium, pp. 51-58.

25. Henrion, W., DiSanza, L., Ip, M., Terry, S., and Jerman, H., [1990], *"Wide-dynamic range direct digital accelerometer,"* in Tech. Dig. Solid-State Sensors Actuators Workshop, pp. 153–156.

26. Hernried A. G., and Sackman J. L., [1968], *"The Two –Degree-Of- Freedom Equipment Structure System,"* Journal of engineering mechanics **112**(6), pp .621 - 628.

27. Hsu, T., [2002], *"MEMS and MICROSYSTEMS Design and Manufacture,"* McGraw Hill, 1st.

28. Jiang Y., Du, M., Huang W., Xu W., and Luo L., [2003], "*Simulation on the Encapsulation Effect of the High-g Shock MEMS Accelerometer*," Proc. 5th International Conference on Electronic Packaging Technology, **28**(30), pp. 52 – 55.

29. Jordy, D., and Younis, M. I., [2008], *"Characterization of the Dynamical Response of a Micromachined G-sensor to Mechanical Shock Loading,"* J. Dyn. Sys., Meas., Control, **13**.

30. Lalanne, C., [2002] *"Mechanical Shock,"* Hermes Penton, 1st.

31. Legtenberg, R., and Tilmans, H. A. C., [1994], *"Electrostatically driven vacuum-encapsulated polysilicon resonators, part I: Design and fabrication,"* Sensors and Actuators A: Physical, **45**(1), pp. 57-66.

32. Legtenberg, R., and Tilmans, H. A. C., [1994], *"Electrostatically driven vacuum-encapsulated polysilicon resonators, part II: Theory and performance,"* Sensors and Actuators A: Physical, **45**(1), pp. 67-84.

33. Letuthold, H., and Rudolf, F., [1990], *"An ASIC for high-resolution capacitive microaccelerometers,"* Sensors Actuators A, pp. 278–281.

34. Li G., and Shemansky Jr., [2000], *"Drop Test Analysis on Micro-machined Structures,"* Sensors and Actuators A, **85**, pp.280-286.

35. Lim, C., Teo, Y. M., and Shim, V. P. W., [2002], *"Numerical Simulation of the Drop impact Response of a Portable Electronic Product,"* IEEE Transactions on Components and Packaging Technologies, **25**(3), pp. 478-485.

36. Liu, C., Brazilai, A. M., Reynolds, J. K., Partridge, A., Kenny, T. W., Grade, J. D., and Rockstad, K., [1998], *"Characterization of a high-sensitivity micromachined tunneling accelerometer with micro-g resolution,"* J. Microelectromech. Syst., **2**, pp. 235–244.

37. Liu, S., Davidson, A., and Lin, Q., [2004], *"Simulation studies on nonlinear dynamics and chaos in a MEMS cantilever control system,"* Journal of Micromechanics and Microengineering, **14**(7), pp. 1064-1073.

38. Luan, J., Tee, T. Y., Pek, E., Lim, C. T., and Zhong, Z., [2003], “*Modal Analysis and Dynamic Responses of Board Level Drop Test,”* Proceedings of the IEEE 2003 Electronics Packaging Technology Conference, pp. 233-243.

39. Nayfeh, A. H., and Balachandran, B., [1995], *“Applied nonlinear dynamics,”* Wiley, New York.

40. Nayfeh, A. H., and Younis, M. I., [2004], *“A new approach to the modeling and simulation of flexible microstructures under the effect of squeeze-film damping,”* Journal of Micromechanics and Microengineering, **14**, pp. 170-181.

41. Nayfeh, A. H., and Younis, M. I., [2005], *Dynamics of MEMS resonators under subharmonic excitations,”* Journal of Micromechanics and Microengineering. **15**(10), pp. 1840-1847.

42. Nayfeh, A. H., Younis, M. I., and Abdel-Rahman, E. M., [2007], “*Dynamic pull-in phenomenon in MEMS resonators,”* Journal of Nonlinear Dynamics, **48**, pp. 153-163.

43. Ong, Y. C., Shim, V. P. W., Chai, T. C., and Lim, C. T., [2003], “*Comparison of Mechanical Response of PCBs Subjected to Product-Level and Board-Level Drop impact Tests,”* Proceedings of the IEEE 2003 Electronics Packaging Technology Conference, pp. 223-227.

44. Pan, F., Kubby, J., Peeters, E., Tran, A. T., and Mukherjee, S., [1998], “*Squeeze film damping effect on the dynamic response of a MEMS torsion mirror,”* Journal of Micromechanics and Microengineering, **8**, pp. 200-208.

45. Pitarresi, J. M., and Primavera, A. A., [1992], *“Comparison of Modeling Techniques for the Vibration Analysis of Printed Circuit Cards,”* Journal of Electronics Packaging, **114**, pp. 378-383.

46. Rebeiz, G. M., [2003], *“RE MEMS Theory, Design, and Technology,”* Wiley-Interscience, 1st.

47. Roszhart, T. V., Jerman, h., Drake, J., and de Cotiis, C., [1995], “*An inertial-grade micromachined vibrating beam accelerometer,”* in Tech. Dig. Eighth Int. Conf. Solid-State Sensors Actuators, pp. 656–658.

48. Rudolf, F., Jornod, A., Berqvist, J., and Leuthold, H., [1990], "*Precision accelerometers with* μg *resolution,*" Sensors Actuators A, pp. 297–302.

49. Sensata Technologies; Available www.sensata.com

50. Shao, L. C., Palaniapan, M., and Tan, W. W., [2008], "*The nonlinearity cancellation phenomenon in micromechanical resonators,*" Journal of Micromechanics and Microengineering, **18**.

51. Shao, L. C., Palanipan, M., Tan, W. W., and Khine, L., [2008], "*Nonlinearity in micromechanical free-free beam resonators: Modeling and experimental verification,*" Journal of Micromechanics and Microengineering, **18**(2).

52. Srikar V., and Senturia S., [2002], "*The Reliability of Microelectromechanical Systems (MEMS) in Shock Environments,*" Journal of Microelectromechanical Systems, **11** (3), pp. 206-214.

53. Starr, J. B., [1990], "*Squeeze film damping in solid state accelerometer,*" Proceedings of the IEEE Solid State Sensor and Actuator Workshop, pp. 44-47.

54. Steinberg D. S., [2000] "*Vibration Analysis for Electronic Equipment,*" Wiley Interscience, 3^{ed} edition.

55. Suhir, E., [2000], "*Predicted Fundamental Vibration Frequency of a Heavy Electronic Component Mounted on a Printed Circuit Board,*" Journal of Electronic Packaging, **122**, pp. 3-5.

56. Sung, S., and Lee, J. G., [2000], "*Development of a tunable resonant accelerometer with self-sustained oscillation loop,*" Proceedings of the IEEE 2000 National Aerospace and Electronics Conference, pp. 354-361.

57. Tanner D.M., Walraven J.A., Helgesen K., Irwin L.W., Smith N.F., and Masters N., [2000], "*MEMS reliability in shock environments,*" Proc. IEEE Intl. Reliability Physics Symposium, San Jose, CA, pp. 129-138.

58. Tas N., Sonnenberg T., Jansen H., Legtenberg R, and Elwenspoek M., [1996], "*Stiction in surface micromachining,*" J. Micromech. Microeng. **6**, pp.385–397.

59. The Math Work, Available http://www.mathworks.com/.

60. Thomson, W. T., [1960], *"Shock spectra of a nonlinear system,"* Journal of Applied Mechanics, pp. 528-534.

61. Thomson, W. T., and Dahleh, M. D., [1998], *"Theory of Vibration with Applications,"* Prentice Hall, 5th.

62. Tilmans, H. A., Legtenberg, R., [1994] *"Electrostatically driven vacuum encapsulated polysilicon resonators. Part II. Theory and performance,"* Sensors and Actuators A, **45,** pp.67–84.

63. Veijola, T., Kuisma, H., Lahdenpera, J., and Ryhanen, T., [1995], *"Equivalent-circuit model of the squeezed gas film in silicon accelerometer,"* Sensors and Actuators A, **48**, pp. 239-248.

64. Veijola, T., Mattila, T., Jaakkola, O., Kiihamaki, J., Lamminaki, T., Oja, A., Ruokonen, K., Seppa, H. Seppala, P., and Tittonen, I., [2000], *"Large-displacement modeling and simulation of micromechanical electrostatically driven resonators using the harmonic balance method,"* Proceedings of the IEEE 2000 Intelligent and Manufacturing Systems Conference, pp. 99-102.

65. Wagner U., Franz J., Schweiker M., Bernhard W., Muller-Fiedler R., Michel B., and Paul O., [2001], *"Mechanical reliability of MEMS-structures under shock load,"* Microelectronic Reliability **41**, pp.1657-1662.

66. Wong E. H., Mai Y. W., Seah S.K., [2005], *"Board level drop impact: Fundamental and parametric analysis,"* Journal of Electronic Packaging, Transactions of the ASME, **127**(4) , pp. 496-502.

67. Wong, E. H., [2005], *"Dynamics of Board-Level Drop Impact,"* Journal of Electronic Packaging. Transactions of the ASME, **127**(3), pp. 200-207.

68. Yazdi, N., and Najafi, K, [2000], *"All-silicon single-wafer micro-g accelerometer with a combined surface and bulk micromachining process,"* J. Microelectromech. Syst., **9**, pp. 544–550.

69. Young, D., Barton, M. V., and Fung, Y. C., [1963], *"Shock spectra for nonlinear spring mass systems and their applications to design,"* AIAA Journal, **1**(7), pp.1597-1602.

70. Younis, M. I., Abdel-Rahman, E. M., and Nayfeh, A. H., [2003], *"A reduced-order model for electrically actuated microbeam-based MEMS,"* J. Microelectromech. Syst., **12**, pp. 672-680.

71. Younis, M. I., and Nayfeh, A. H., [2003], *"A study of the nonlinear response of a resonant microbeam to an electric actuation,"* Nonlinear Dynamics, **31**(1), pp. 91-117.

72. Younis M. I., Miles R. and Jordy D., [2006], *" Investigation of the Response of Microstructures under the Combined Effect of Mechanical Shock and Electrostatic Forces,"* J. Micromech. Microeng., **16**, pp. 2463-2474.

73. Younis, M. I., Alsaleem, F. M., and Jordy, D. [2007], *"The response of clamped-clamped microbeams under mechanical shock,"* International Journal of Non-Linear Mechanics, doi:10.1016/j.ijnonlinmec.2007.01.017

74. Younis, M. I., Alsaleem, F. M., Miles R., and Su Q., [2007], *"Characterization of the performance of capacitive switches activated by mechanical shock,"* Micromech. Microeng., **17**, pp. 1360-1370.

75. Younis, M. I., and Nayfeh, A. H., [2007], *"Simulation of squeeze-film damping of microplates actuated by large electrostatic load,"* Transactions of ASME Journal of Computational and Nonlinear Dynamics, **2**, pp. 232-241.

76. Younis, M. I., Jordy, D., and Pitarresi J., [2007], *"Computationally efficient approaches to characterize the dynamic response of microstructures under mechanical shock"* J. Microelectromech. Syst., **16**, pp. 628-638.

77. Younis, M. I., and Alsaleem, F. M., [2008], *"Nonlinear Dynamics of Electrostatically Actuated Resonators Part II: Mass Sensing Applications,"* J. Microelectromech. Syst.,

78. Zhang, C., Xu, G., and Juang, Q., [2004], *"Characterization of the squeeze film damping effect on the quality factor of a microbeam resonator,"* Journal of Micromechanics and Microengineering, **14**, pp. 1302-1306.